COSMOLOGY THROUGH GRAVITATIONAL LENSES

by

Rodrigo Gil-Merino Rubio

A THESIS SUBMITTED TO THE UNIVERSITY OF POTSDAM
FOR THE DEGREE OF DOCTOR RERUM NATURALIUM
IN THE DISCIPLINE OF ASTROPHYSICS.
MATHEMATISCH-NATURWISSENSCHAFTLICHEN FAKULTÄT
SEPTEMBER 2003

Cover design: My idea of a Miro
interpretation of this work.

Produced in LaTeX 2ε.

Are we mark this day with a white or a black stone?

Don Quijote (Part II, Chap. XVI)

A mi padre,
que no cabrá en sí,
y a mi madre,
que hacía hueco para todos.

Y a Ana,
cuya ilusión es infinita.

Abstract

In this thesis the gravitational lensing effect is used to explore a number of cosmological topics. We determine the time delay in the gravitationally lensed quasar system HE 1104−1805 using different techniques. We obtain a time delay $\Delta t_{A-B} = (-310 \pm 20)$ days (2σ errors) between the two components. We also study the double quasar Q0957+561 during a three years monitoring campaign. The fluctuations we find in the difference light curves are completely consistent with noise and no microlensing is needed to explain these fluctuations. Microlensing is also studied in the quadruple quasar Q2237+0305 during the GLITP collaboration (Oct.1999-Feb.2000). We use the absence of a strong microlensing signal to obtain an upper limit of $v_{\rm bulk} = 600$ km/s for the effective transverse velocity of the lens galaxy (considering microlenses with $M_{\rm lens} = 0.1\ M_{\odot}$).

The distribution of dark matter in galaxy clusters is also studied in the second part of the thesis. In the cluster of galaxies Cl 0024+1654 we obtain a mass-to-light ratio of $M/L \simeq 200\ M_{\odot}/L_{\odot}$ (within a radius of 3 arcminutes). In the galaxy cluster RBS380 we find a relatively low X-ray luminosity for a massive cluster of $L_{X,bol} = 2 \cdot 10^{44}$ erg/s, but a rich distribution of galaxies in the optical band.

Abstract

In dieser Dissertation nutze ich den Gravitationslinseneffekt, um eine Reihe von kosmologischen Fragen zu untersuchen. Den Laufzeitunterschied des Gravitationslinsensystems HE 1104−1805 wurde mit unterschiedlichen Methoden bestimmt. Zwischen den beiden Komponenten erhalte ich einen Unterschied von $\Delta t_{A-B} = (-310 \pm 20)$ Tagen (2σ -Konfidenzintervall).

Auerdem nutze ich eine dreijährige Beobachtungskampagne, um den Doppelquasar Q0957+561 zu untersuchen. Die beobachteten Fluktuationen in den Differenzlichtkurven lassen sich durch Rauschen erklären, ein Mikrogravitationslinseneffekt wird zur Erklärung nicht benötigt. Am Vierfachquasar Q2237+0305 untersuchte ich den Mikrogravitationslinseneffekt anhand der Daten der GLITP-Kollaboration (Okt. 1999-Feb. 2000). Durch die Abwesenheit eines starken Mikrogravitationslinsensignals konnte ich eine obere Grenze von $v_{\rm bulk} = 600$ km/s fr die effektive Transversalgeschwindigkeit der Linsengalaxie bestimmen (unter der Annahme von Mikrolinsen der Masse $M_{\rm lens} = 0.1\ M_\odot$).

Im zweiten Teil der Arbeit untersuchte ich die Verteilung der Dunklen Materie in Galaxienhaufen. Fr den Galaxienhaufen Cl 0024+1654 erhalte ich ein Masse-Leuchtkraft-Verhältnis von $M/L \simeq 200\ M_\odot/L_\odot$ (innerhalb eines Radius von 3 Bogenminuten). Im Galaxienhaufen RBS380 finde ich eine relativ geringe Röntgenleuchtkraft von $L_{X,bol} = 2 \cdot 10^{44}$ erg/s, obwohl im optischen eine groe Anzahl von Galaxien gefunden wurde.

Preface

After the discovery of the first gravitationally lensed quasar almost 25 years ago, gravitational lensing – the bending of light by a mass distribution– has become a powerful and versatile tool. It is used in the search for planets outside the Solar System and for dark matter in galaxies' halos and in clusters of galaxies. It is playing a key role in the study of the nature and structure of quasars, and also it helps in understanding stellar atmospheres. The phenomenon itself was a test for General Relativity, but nowadays it has already opened its own link with singularity theory, giving mathematicians a laboratory for their concepts. And, moreover, gravitational lensing is probably one of the best tools to answer important cosmological questions about the age, size and composition of the Universe. Obviously, it is impossible to cover all these topics in a thesis. Nevertheless, in this work we have tried to address a number of different problems applying gravitational lensing, and we have focused our efforts in its cosmological applications.

Measuring the time delays between multiple images of the same lensed quasar, the Hubble constant – the expansion rate of the Universe– can be estimated. The Chapter 4 is dedicated to explore some of the most common techniques employed in the determination of time delays in lensed quasars and to discuss the problems that might arise. The result is a new time delay estimation in the double quasar HE $1104-1805$. Following with the studies of lensed quasars, Chapter 5 shows a simple but robust way of analysing difference lightcurves through Monte Carlo simulations. No short time-scale microlensing fluctuations –lensing induced by substructure in the lens– were found in the double quasar Q0957+561 in the monitoring campaigns analysed. If microlensing fluctuations cannot be measured in a system in which they were previously detected, interesting implications can be derived. In Chapter 6 the absence of microlensing in the quadruple quasar Q2237+0305 is used to place limits on the transverse velocity of the lensing galaxy.

Clusters of galaxies can act as gravitational lenses, too. In fact, they can produce multiple distorted images of background galaxies (called giant arcs) as well as only induce little elongations in them (called weak lensing). The former effect allows to model the gravitational potential in the inner parts of the galaxy cluster, whereas the latter is able to do it at larger scales. Observing galaxy clusters in X-rays offers a way of cross-checking lensing results. A problem appears when these different approaches give different results for the same physical quantity. In Chapter 7 the galaxy cluster Cl 0024+1654 is studied using the weak lensing theory with a multiband photometry dataset and the results compared to other techniques. Chapter 8 is dedicated to the galaxy cluster RBS380, using both X-rays and optical data.

A brief note on *how to read this thesis*. The content is divided in four parts: an Introduction (Part I), with some historical remarks and the needed theoretical background, Part II devoted to quasar lensing, Part III with the galaxy cluster lensing and X-ray analysis and Part IV with the final remarks. All the chapters in parts II and III have a two-paragraph abstract. The first one is called **Link** and it is used to introduce the chapter in the general context of the thesis. The second one is the **Abstract** itself, and summarizes the particular content of the chapter. At the end of the thesis an **Index** of selected terms is also available.

Contents

List of Figures

List of Tables

Part I

General Introduction

Chapter 1

Historical perspective

In the introduction to one of the lastest lensing conference proceedings, Virginia Trimble pointed out that this topic, as any other in science, can be traced arbitrarily far back in history (Trimble 2001). In our view, this is only partially true: 'arbitrarily' is too much. Discoveries are not just snapshots of ideal lives. They require a context to appear and the context is the evolution of certain initial conditions. One has to go back in time to get a wider perspective and not exclusively scientific. Brilliant minds are needed, but they fight against something else than simple ignorance in a particular epoch, they also fight against the social conditions at that time and the historical heritage that configures that society. For several reasons, we cannot analyse all these aspects here. It would surely be another thesis. Instead, we follow the somehow standard steps in the historical introduction of the subject, keeping in mind that these are merely guidelines of a story not yet written.

To understand how the theory of gravitational lensing arose in a particular moment of history, one must follow the footprints of the theories of gravitation. The historical evolution of the ideas behind the concept of gravitation is very much linked with the description of the movement of bodies, both in the sky and on the ground[1].

In 1684 Edmond Halley visited Newton in Cambridge. Halley asked Newton what trajectory would describe a planet following a force inversely proportional to the square of the distances. Halley, Christopher Wren and Robert Hooke were trying to solve the problem, but they did not find a solution. Newton answered that it was an elipse, but that he had not yet the proof and promised to send it to Halley when found. Newton sent several works in mechanics to Halley. After revising all the material, Halley pressed Newton to publish the results. The serie of books was called "*Principia mathematica philosophiae naturalis*". The *Principia*, with the theory of gravitation included, was a challenge to the accepted view of nature at that time. Newton's ideas were based on the work of Brahe, Copernicus, Galileo, Kepler and others, none of them plainly accepted by then. One of the reasons for this was that discarding the Aristotelian conception of the sky, there was not a satisfactory cosmogony. Around 1630, Descartes wrote "Le Monde, ou Traité de la lumiére" in which he developed a theory of gravitation in terms of his theory of celestial vortices (the book appeared after his death because when he was going to publish it, the Inquisition condemned Galileo and he thought the moment was not the best). In fact, Newton himself was Cartesian before

[1] Several histories of astronomy are available in the market. Abetti (1949), Hoskin (1999) and North (1994) are the three we have used. Further readings can be found there.

completely developing his *Principia*. Again, the Newtonian theories were specially rejected by philosophers, with Leibniz at the head of them. Leibniz did not like the role space and time had in the Newtonian system. This period is one of the most exciting and turbulent episodes in history, where scientific progress was mixed up with philosophy, religion and society. The excellence of the scientific output probably eclipsed this fact. A very interesting discussion, from the philosophical point of view, can be found in Sklar (1992) and a wider treatment in Torretti (1999).

The idea that mass can bend light[2] is well known since the early 19th century, when Soldner (1804) derived the deflection angle of a light ray passing close to the sun using Newton's theory of gravity. In fact, Cavendish calculated it in the same way at the end of the 18th century, motivated by John Michells ideas on the light attraction by the Sun. Although Cavendish did not publish his results, they appeared in one of his manuscripts (see Will 1988). Laplace (1795) also calculated the velocity required to escape from a gravitational field produced by a spherical body. Both Michell and Laplace realised that a body with a high enough density would not allow the light to escape from it, so that it would appear completely black. These were the ideas that inspired Soldner to calculate the deviation of a test particle when passing close to a body and apply it to light.

The phenomenon was reconsidered a century later, when Einstein developed his General Theory of Relativity in 1916, predicting a deflection angle twice the value obtained by Soldner[3]. During the famous solar eclipse in 1919 the apparent angular displacement of background stars when close to the sun's limb was measured (an expedition was planned in 1914 by E.Freundlich, but they could not take scientific data because of the World War I). These measurements were the confirmation of Einstein's prediction and one of the successful first tests to General Relativity. At that time, O.J. Lodge (1919) introduced the term 'lens' in the context of gravitational deflection of light, although he argued that it was imprecise because these lenses have no focal length. The term 'gravitational lensing' was born.

But it was Eddington (1920) first to suggest that multiple images could be observed if two stars were aligned and calculated, although wrongly, a magnification factor for the images. Moreover, Chwolson (1924) mentioned that if the alignment between the stars were perfect, there should not be multiple images, but a ring-like one. We now call these images *Einstein rings*.

Einstein (1936) calculated the cross-section for lensing of stars in our Galaxy and concluded that it was very small and the phenomenon difficult to observe. Nevertheless, Zwicky (1937a, b) computed a higher probability for observing lensing when applied to what was called *extragalactic nebulae* (the name for galaxies at that moment). He noted that the discovery of gravitational mirages would be a test for relativity and the effect would act as a natural telecope since it would enable us to see galaxies at larger distances, due to the magnification of the sources. Zwicky applied the virial theorem – which relates the kinetical and potential energy of a given system with its dynamical state – to estimate the masses of clusters of galaxies and soon he realised that gravitational lensing would provide a direct estimator of cluster and galaxy masses.

After Zwicky there was again a parenthesis of around three decades without significant improvement in lensing studies. Then, close in time, Klimov (1963) studied the galaxy-galaxy lensing

[2]For the historical aspects of gravitational lensing, we follow Schneider et al. (1992), Petters et al. (2001) and Trimble (2001). More references can be found there.

[3]Although this factor of two is sometimes viewed as a little difference between the GR and Newton's one, the fact is that this factor is nothing but a coincidence. Newton's theory cannot be applied to explain the light deflection and it is conceptually wrong to do it.

configuration concluding that both ring-like and multiple images could form depending on the alignment of the galaxies and Liebes (1964) paid attention on the star-star lensing. Liebes suggested that stars in our galaxy might lens stars in nearby galaxies (e.g. Andromeda), an idea on which the actual searching of compact objects (and planets) in the halo of the Milky Way is based (Paczyński 1986b). Refsdal (1964a,b) proposed a method for calculating the Hubble constant using gravitationally lensed quasars based on the different arrival times for each image (15 years before the phenomenon was observed!!). With the papers by Refsdal, a great theoretical effort on gravitational lensing started.

The first gravitationally lensed quasar Q0957+561 was discovered by Walsh, Carswell and Weymann (1979). The discovery, as many others in science, was serendipitous: two quasar images were accidentally observed, with a separation of 6.1 arcseconds and apparently at the same distance (at the same redshift of z =1.41, see Section 2.1.4 for a definition of redshift). Soon after, the lensing galaxy was detected at a redshift of z =0.36 (Stockton 1980). There was no doubt about the nature of the effect: gravitational lensing became an observational fact.

Chapter 2

Basic concepts

The present Chapter is divided in two main sections. In the first one, the basic concepts of general relativity and cosmology are reviewed. The second one contains the highlights of the theory of lravitational lensing. General Relativity gives the framework in which gravitational lensing is developed, although only those results oriented to cosmology are presented. Moreover, in the chapters after this general introduction, some concepts might be used in a slightly different way and then discussed again. In spite of being somewhat repetitive, we consider that in this way the chapters can also be viewed independently and those readers only interested in selected parts and having already some background in the subject can go directly to them.

2.1 General Relativity and Cosmology

The bending of light by matter can only be properly described by using the theory of General Relativity (GR). In this Section, we briefly introduce some of the main concepts of GR on which gravitational lensing is based[1].

2.1.1 Einstein field equations

The fundamental equation of GR are the field equations, that describes the space-time curvature in the presence of a distribution of matter and/or energy. These equations state:

$$G_{ik} - \Lambda g_{ik} = \frac{8\pi G}{c^4} T_{ik} \tag{2.1}$$

where G_{ik} is the curvature tensor that describes the space-time geometry, Λ is the cosmological constant, g_{ik} is the metric tensor, G is the Newtonian gravity constant, c is the speed of light and T_{ik} is the energy-momentum tensor that describes the mass and energy distribution.

[1] A detailed description of GR is obviously out of the scope of this short introduction. Textbooks where this can be found are, e.g., Weinberg (1972), Misner et al. (1973), Schutz B.F. (1985), Peebles (1993) or Peacock (1999) among many others. A brief but excellent essay is Schrödinger (1950). A monograph with special attention to the philosophycal implications of GR can be found, e.g., in Friedman (1983).

2.1.2 The Roberson-Walker metric

Finding exact solutions to Eq. 2.1 is not easy and implies the knowledge of the distribution of matter and energy in space-time. A way of simplifying this is by assuming the Universe has two properties:

a) that the average matter on large scales is distributed homogeneously and isotropically (in general, isotropy from any point implies homogeneity, but the reverse is not true, see Fig. 2.1 to illustrate these ideas);

b) that the matter and energy that fills the Universe can be treated as a perfect fluid.

Condition a) is usually referred to as the *cosmological principle*, whereas condition b) is called the *Weyl condition*. These two conditions can be expressed mathematically as:

$$\textit{cosmological principle} \quad \rightarrow \quad ds^2 = c^2dt^2 - a^2(t)\left[\frac{dr^2}{1-kr^2} + r^2(d\theta^2 + \sin^2\theta d\phi^2)\right] \tag{2.2}$$

$$\textit{Weyl condition} \quad \rightarrow \quad T_{ij} = (\rho + p)u_i u_j - p g_{ij} \tag{2.3}$$

The expression 2.2 means that the assumption of the *cosmological principle* allows us to define the metric (the 'line element' ds) in terms of a dimensionless time-varying scale factor $a(t)$ and a parameter $k = 1$, 0, -1, which is the value that determines the total curvature of the Universe; t is the time coordinate and r, θ and ϕ are the spatial coordinates. A metric defined in this way is called *Robertson-Walker metric*. The *Weyl condition* implies that the energy-momentum can be described as in expression 2.3, so that the evolution of the density ρ and the pressure p in time depends on the metric tensor g_{ij} and the 4-velocity components u_i. A cosmology based on these two conditions is called a *Friedmann cosmology* and the solutions obtained from Eq. 2.1 with these constraints are called *Friedmann models*.

FIGURE 2.1: To illustrate the concepts of homogeneity and isotropy. In the *left* box, the material distribution is homogeneous and isotropic. The *middle* box shows a homogeneous – at large scales – but anisotropic distribution. Finally, matter in the *right* box is anisotropically and inhomogeneously distributed.

2.1.3 Friedmann models and cosmological parameters

The *Friedmann solutions* comprise two independent equations:

$$\left(\frac{\dot{a}}{a}\right)^2 = \frac{8\pi G}{3}\rho - \frac{kc^2}{a^2} + \frac{1}{3}\Lambda c^2 \tag{2.4}$$

$$\frac{\ddot{a}}{a} = \frac{1}{3}\Lambda - \frac{4\pi G}{3}\left(\rho + \frac{3p}{c^2}\right) \tag{2.5}$$

With these two equations we relate the pressure p and density ρ to the scale factor $a(t)$. In fact, the quantity $(\dot{a}/a)$ is the rate at which this scale factor increases or, in other words, the rate at which the Universe is expanding. This quantity is called the *Hubble parameter*: $(\dot{a}/a) \equiv H$ and its value for the present epoch t_0 is the *Hubble constant*: $\dot{a}(t_0)/a(t_0) \equiv H_0$. Setting $\Lambda = 0$ and $k = 0$ in Eq. 2.4 we get a special value for the density called *critical* or *closure density*

$$\rho_{cr} = \frac{3H_0^2}{8\pi G}. \tag{2.6}$$

This is the density limit for which the Universe is: a) geometrically closed if $\rho < \rho_{cr}$; b) geometrically open if $\rho > \rho_{cr}$. Condition a) is satisfied for $k < 0$ and means that expansion of the Universe will 'turn around' – stops expansion and starts contraction –. Condition b) is satisfied for $k > 0$ and gives hyperbolic models, which means expansion forever. Cosmologies with $k = 0$ are called *flat cosmologies* and expansion goes asymptotically to zero.

A *Friedmann model* can then be uniquely determined by four parameters:

$$H_0 = \frac{\dot{a}_0}{a_0}; \qquad \Omega_M = \frac{8\pi G}{3H_0^2}\rho_0; \qquad \Omega_\Lambda = \frac{\Lambda c^2}{3H_0^2}; \qquad \Omega_k = -\frac{kc^2}{a_0^2 H_0^2}, \tag{2.7}$$

where subindex 0 denotes again present time t_0. The *Friedmann solutions*, Eqs. 2.4 and 2.5, can be rewritten in terms of these parameters – *the cosmological parameters* – as

$$\Omega_M + \Omega_\Lambda + \Omega_k = 1. \tag{2.8}$$

If we consider $k = 0$, i.e., a *flat* Universe, Eq. 2.8 is reduced to $\Omega_M + \Omega_\Lambda = 1$. In this case, since the curvature of space-time is considered to be zero, we recover formally Euclidean space.

2.1.4 Redshift and cosmic distances

Without knowing the value of the *the cosmological parameters* parameters, it is not possible to know the absolute distances to far away objects in the Universe. We refer to the distance of a given object by its *redshift* z: light suffers the expansion of the Universe and when a photon is emitted at a time t_e from a distant object with a wavelength λ_e, it is redshifted by the expansion to a wavelength λ_0 at the present time t_0, when it is observed. The relation between the *redshift*, the scale factors $a(t)$ and the wavelengths is

$$1 + z = \frac{\lambda_0}{\lambda_e} = \frac{a(t_0)}{a(t_e)}. \tag{2.9}$$

Thus, in a cosmological context, it is common practise to use the *redshift* of a source as a measure of its distance to us. For this we need a definition of distance as a function of redshift.

In *flat cosmologies* (see Eq. 2.8 with $k = 0$) a useful definition of the distance of a source at a *redshift* z is

$$D = \frac{2c}{H_0}\frac{1}{(1+z)^2}\left[1 + z - \sqrt{1+z}\,\right]. \tag{2.10}$$

A distance defined in this way is called *angular-diameter distance*. The term comes from the fact that two separate sources at a distance d that subtend an angle θ satisfy $separation = \theta \times d$. The *angular-diameter distance*, D_{ang} between two sources with *redshifts* z_1 and z_2 (and $z_1 \leq z_2$) is

$$D_{ang} = \frac{2c}{H_0} \frac{1}{1+z_2} \left[(1+z_1)^{-1/2} - (1+z_2)^{-1/2} \right]. \tag{2.11}$$

There are other possible ways of defining distances, which are also useful in astronomy. We give three more definitions and the relations between them[2]: the *proper distance*, the *comoving distance* and the *luminosity distance*.

The *proper distance*, D_{prop}, between z_1 and z_2 is the distance measured by the travel time of a photon propagating from z_1 to z_2 and can be written as

$$D_{prop} = \frac{2c}{3H_0} \left[(1+z_1)^{-3/2} - (1+z_2)^{-3/2} \right]. \tag{2.12}$$

The *comoving distance* D_{com} between z_1 and z_2 is the distance which remains constant with epoch if the two sources are moving with the Hubble flow (i.e., the expansion). The *luminosity distance* D_L is defined, like in an Euclidean space, as the relation between the luminosity of a source at z_2 and the flux received at z_1. The latter two distance definitions can be easily expressed in terms of the *angular-diameter distance* D_{ang} as (notice that they are all defined between redshifts z_1 and z_2)

$$\begin{aligned} D_{com} &= (1+z_2)\, D_{ang} \\ D_L &= \left(\frac{1+z_2}{1+z_1} \right)^2 D_{ang}. \end{aligned} \tag{2.13}$$

Observational cosmology tries to give an answer to probably one of the main questions in Astrophysics: which are the values of the *cosmological parameters* in Eq. 2.7?. To answer this question means to know the age, size and evolution of the Universe, to fix the distance ladder and also to know what the Universe is made of. Currently, gravitational lensing has revealed itself as one of the most powerful tools to explore possible answers to this question. Thus, as it will be described in the next Section, searching the values of the *Hubble constant* H_0 and the density parameters Ω_M and Ω_Λ is what extragalactic gravitational lensing deals with, among other problems.

2.2 Gravitational Lensing

The gravitational lensing theory has been developed in two excellent books. One is Schneider et al. (1992), with theory, observations and applications; unfortunately its second edition (1999) was not an update. A more mathematical treatment appeared recently in Petters et al. (2001), with special attention on singularity theory. Although the main goal of the book is to develop a mathematical theory of gravitational lensing (in the thin-screen, weak-field approximations), the part in which the astrophysical aspects are explained is a very good introduction from a physical point of view. This Section gives an overview following these two books and most of the material presented here can be found there in much more detail.

[2]There is a concise discussion on distances in, e.g., Bartelmann and Schneider (2001)

2.2.1 Deflection angle, lens equation and the gravitational potential

The deflection angle $\widehat{\alpha}$ of a light ray when passing close to a spherical mass distribution M within a distance or impact parameter r is

$$\widehat{\alpha} = \frac{4GM(\leq r)}{c^2} \tag{2.14}$$

where G is the gravity constant and c the speed of light.

This expression can be extended to a surface mass distribution. In that case, the mass can be expressed as $M = \Sigma(\vec{r'})\ d^2r'$, where $\Sigma(\vec{r'})$ is the surface mass density in an area d^2r'. The deflection angle becomes

$$\widehat{\alpha}(\vec{r}) = \frac{4G}{c^2 r} \int_{\Re^2} \Sigma(\vec{r'}) \frac{\vec{r} - \vec{r'}}{|\vec{r} - \vec{r'}|^2} d^2r' \tag{2.15}$$

and is valid for any surface mass density in the limit of velocities $v \ll c$ and small angles. This is the weak field limit.

In most of the astrophysical applications the condition of small deflection angles is verified and the weak-field limit is a good aproximation. By using just geometrical considerations (see Fig. 2.2), we can derive a relation between the positions in the source and lens planes: the lens equation

$$\vec{s} = \frac{D_s}{D_d}\vec{r} - D_{ds}\widehat{\alpha}(\vec{r}), \tag{2.16}$$

where D_s, D_d and D_{ds} are the angular distances between observer-source, observer-lens (deflector) and lens-source respectively; $\vec{s}$ define positions in the source plane and $\vec{r}$ in the lens one.

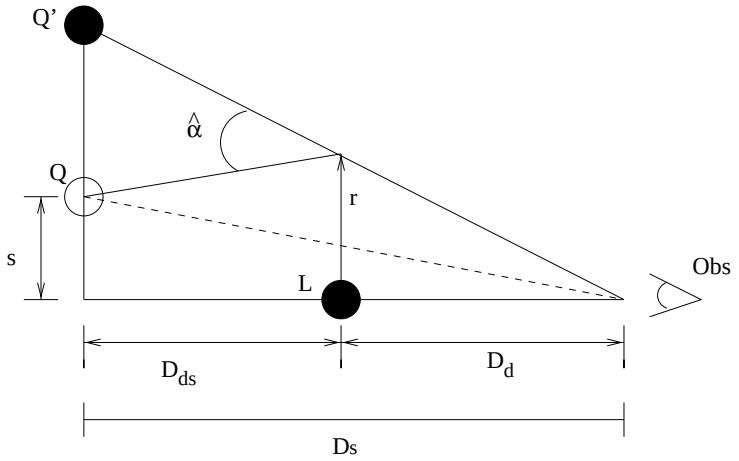

FIGURE 2.2: Configuration of a gravitational lens. The deflection angle $\widehat{\alpha}$ relates the position in the lens plane $\vec{r}$ with that in the souce plane $\vec{s}$, using Equation 2.16. Q is the source, Q' is where the observer (Obs) sees the image of Q and L is the lens.

The lens equation can be rewritten in a dimensionless way , with a simple change of variables $\vec{x} = \vec{r}/r_0$ and $\vec{y} = \vec{s}/s_0$, where $s_0 = r_0\ D_s/D_d$ and r_0 is an arbitrary scale length. The surface mass density can be normalized and written as

$$\kappa(\vec{x}) = \Sigma(\vec{x})/\Sigma_{crit}, \qquad \text{where} \qquad \Sigma_{\rm crit} = \frac{\rm c^2 D_s}{4\pi \rm G D_d D_{ds}}. \tag{2.17}$$

Then, the dimensionless lens equation is:

$$\vec{y} = \vec{x} - \vec{\alpha}(\vec{x}) \tag{2.18}$$

and also the dimensionless deflection angle results in:

$$\vec{\alpha}(\vec{x}) = \frac{1}{\pi} \int_{\Re^2} \kappa(\vec{x}) \frac{\vec{x} - \vec{x'}}{|\vec{x} - \vec{x'}|^2} d^2x' \tag{2.19}$$

The critical surface mass density Σ_{crit} in Equation 2.17 is a useful quantity. A sufficient condition for producing multiple images of a background source is that the surface mass density is greater than the critical one. Moreover, if a source lies exactly behind the lens then the image of the source is a ring, due to the symmetry. The angular radius of this ring is called *Einstein radius* and defines the angular scale of the lensing scenario (see Fig. 2.3). It is defined as

$$\theta_E = \sqrt{\frac{4GM}{c^2} \frac{D_{ds}}{D_d D_s}} = \sqrt{\frac{M}{\pi D_d^2 \Sigma_{crit}}}. \tag{2.20}$$

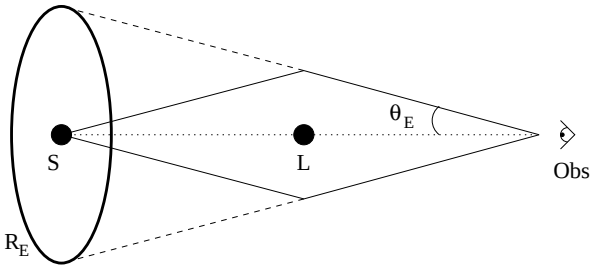

FIGURE 2.3: An Einstein ring is produced if the lens is perfectly aligned with the source and the observer. S is the source, L is the lens and Obs is the observer. θ_E is define in Equation 2.20 and $R_E = D_{OS} \cdot \theta_E$, where D_{OS} is the angular distance between the observer and the source.

It is also useful to define the deflection angle and the lens equation through the gravitational potential. In this way, the deflection angle is the gradient of a gravitational potential $\psi(\vec{x})$ (Schneider 1985)

$$\vec{\alpha}(\vec{x}) = \nabla \psi(\vec{x}). \tag{2.21}$$

The gravitational potential can then be expressed as

$$\psi(\vec{x}) = \frac{1}{\pi} \int_{\Re^2} \kappa(\vec{x}) \ln |\vec{x} - \vec{x'}| d^2x'. \tag{2.22}$$

Using then Eq. 2.21, the lens equation can be written in terms of the gravitational potential

$$\vec{y} = \nabla [\frac{1}{2}\vec{x}^2 - \psi(\vec{x})]. \tag{2.23}$$

Introducing the new two-dimensional potential

$$\phi(\vec{x}, \vec{y}) = \frac{1}{2}(\vec{x} - \vec{y})^2 - \psi(\vec{x}), \tag{2.24}$$

equation the lens equation can be expressed in the elegant and simple way

$$\nabla \phi(\vec{x}, \vec{y}) = 0. \tag{2.25}$$

2.2.2 Magnification matrix, convergence, shear and critical lines

The solutions to the lens equation (Eq. 2.16 or 2.18) mark the positions of a source mapped into the image plane. The ratio between the solid angles subtended by the image and the source is called *magnification*. It can be written as the Jacobian matrix of the transformation described by the lens equation (Eq. 2.16) or it can be derived from the gravitational potential in Eq. 2.22:

$$\mathcal{A}_{ij} = \frac{\partial \vec{r}}{\partial \vec{s}} = \left(\delta_{ij} - \frac{\partial^2 \psi(\vec{x})}{\partial x_i \, \partial x_j} \right). \tag{2.26}$$

The Equation 2.22 that relates the gravitational potential $\psi(\vec{x})$ with the surface mass density $\kappa(\vec{x})$ can be inverted to show that

$$\Delta\psi = 2\kappa. \tag{2.27}$$

This allows us to write the *magnification* matrix as

$$\mathcal{A} = \begin{pmatrix} 1-\kappa-\gamma_1 & -\gamma_2 \\ -\gamma_2 & 1-\kappa+\gamma_1 \end{pmatrix} \tag{2.28}$$

where the trace of the matrix is

$$tr\mathcal{A} = 2(1-\kappa) \tag{2.29}$$

and

$$\gamma_1 = \frac{1}{2}\left(\frac{\partial^2 \psi(\vec{x})}{\partial x_1^2} - \frac{\partial^2 \psi(\vec{x})}{\partial x_2^2} \right) \qquad \gamma_2 = \left(\frac{\partial^2 \psi(\vec{x})}{\partial x_1 \, \partial x_2} \right). \tag{2.30}$$

From the determinant of the *magnification* matrix $\mathcal{A}$, we can write the *magnification factor*, μ, as

$$\mu = \frac{1}{det\mathcal{A}} = \frac{1}{(1-\kappa)^2 - \gamma^2} \tag{2.31}$$

where $\gamma = \sqrt{\gamma_1^2 + \gamma_2^2}$. Its physical interpretation is explained below.

The contribution to the *magnification* can be separated in two terms. One is the *surface mass density* κ which is also called *convergence* or *Ricci focusing*. It depends only on the distribution of mass inside the light beam. On the other hand, the contribution due to the mass distribution outside the light beam can also be significant (obviously, if the matter distribution is symmetric, the net contribution is zero). This is called *shear* and is described by the term γ in the previous equations.

Formally, $det\mathcal{A}$ can vanish for certain values of $\vec{r}$ in the lens equation: then the *magnification factor* diverges for those values. The sets of points in the lens plane for which this happens are called *critical lines* and the corresponding lines in the source plane are called *caustics*. However, although mathematically the *magnification factor* becomes infinite, in 'real' cases the sources are extended (not point-like), so that the *magnification* is derived from averaging over the source profile, resulting in a finite value.

Solving the lens equation, the position of the caustics for a given configuration can be calculated. For a low number of lenses (n$\leq$2), this can be done analytically. When the number of lenses is high (n$\gg$2), the distribution of caustics is easier obtained with inverse ray-shooting techniques, in which rays are traced backwards from the observer to the source through the distribution of lenses in the lens plane (Kayser et al. 1986, Schneider & Weiss 1987 and Wambsganss 1990). In this way the two-dimensional magnification distribution in the source plane is obtained. These distributions are called *magnification patterns* (see Chapter 6 for more details).

2.2.3 Time delays and the Hubble constant

If a source is lensed and several images are produced, the light coming from the different images travels paths of different length – or time – , in general. There are two reasons for this: one is that the geometrical distance is not the same; the other one is that the gravitational potential well of the lens, that retards the light ray compared to the unlensed path, affects the images differently (same effect as the *Shapiro effect* in the Sun vicinity). This means that two light beams departing at the same time but corresponding to two different images will reach the observer at different times. The difference between the arrival times is called *time delay*. We can consider a *time delay function* that can be written, from the lens equation in terms of the gravitational potential (Eq. 2.23), as

$$\mathcal{T}(\vec{x}) = \frac{(1+z_d)}{c}\frac{D_d D_s}{D_{ds}}\left[\frac{1}{2}(\vec{y}-\vec{x})^2 - \psi(\vec{x})\right] \tag{2.32}$$

where the notation is the usual. The geometrical part of the *time delay function* is then proportional to the difference $\vec{y}-\vec{x}$, whereas the gravitational time delay is represented by $\psi(\vec{x})$. The *time delay function* is not an observable, but the quantity $\mathcal{T}(\vec{x_i}) - \mathcal{T}(\vec{x_j})$, that is the *time delay* between the images i and j, can be measured and related to the expansion rate of the Universe.

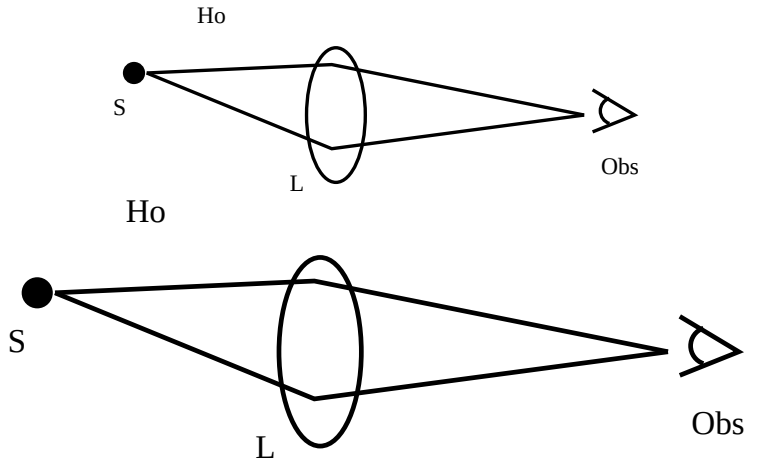

FIGURE 2.4: The time delay in a gravitational lens scales inversely proportional to the Hubble constant H_0. In the Figure, angular image positions, image separations and magnifications as seen from the observer are the same. Only the time delay can physically scale the proper scenario. A larger time delay (bottom sketch) results in a smaller H_0.

Refsdal (1964a,b) showed that the actual expansion rate of the Universe – the *Hubble constant* – is inversely proportional to the *time delay* between two images in a gravitational lens system and directly proportional to the angular separation between the images and the lens centre. Thus the relation holds

$$H_0 \propto \frac{\Delta\theta}{\Delta\mathcal{T}} \tag{2.33}$$

where the constant needed to make the expression an equality depends on the exact description of the lens mass distribution – a lens model –.

2.2.4 Simple lens models and lensing scenarios

To give a model of a gravitational lens system means to mathematically describe the gravitational potential of the deflector. It is usual to classify lens models in two main groups: *point-like* or *extended mass distributions*. Although obviously there are no 'real' point-like mass distributions, sometimes it is not only useful, but can be quantitatively justified. The justification comes from the ratio between the physical angular size of a lens and its Einstein radius. This ratio can be quite different depending on the lensing scenario considered, as shown below.

The first lensing scenario considered in this thesis is that where the source is a distant quasar and we analyse the lensing induced by star-like objects in the halo of the deflector galaxy. These objects, called MACHOs (for MAssive Compact Halo Objects), can produce multiple images of the source, but their angular separation is of the order of only micro-arcseconds and cannot be resolved. The phenomenon is called *microlensing* and the way we have to detect it is to compare the intrinsic fluctuations of the lensed quasar from two images after time-delay correction. Subtracting the lightcurves of these two images one should obtain a flat curve, if no microlensing signal is present. Although in principle any departure from zero in the difference lightcurve can be assigned to *microlensing*, 'noise' can introduce additional features. In Chapter 5 we discuss these problems in the case of the double quasar Q0957+561. In this scenario, the Einstein radii of the micro-lenses is much bigger (two orders of magnitude) than their physical sizes, so the point source approximation for the gravitational potential is valid. The same approximation is also valid in the case of MACHO searches in the Milky Way. The microlensing in our Galaxy is called *galactic microlensing* and it is not considered in this thesis.

In spite of the success of the point-like mass distributions for the situations described in the previous paragraph, this approximation fails in other cases. For example, if we model a lensing galaxy. The angular Einstein radius is of the order of one arcsecond, in many cases smaller than the physical angular size. In the case of the inner parts of galaxy clusters, the typical physical sizes and their Einstein radii are of the order of half an arcminute. In these two cases, the point lens approximation is not a good description, extended mass distributions must be considered. And also in both cases the deflector can be modeled as *elliptical mass distributions*, a particular and simple family of extended distributions.

The second scenario we consider in this thesis is the lensing caused by clusters of galaxies. If not only the inner parts of the cluster are modeled, but also the outer regions are included, then more complicated models are needed and it is not enough the use of elliptical mass distributions. The lensing induced by such structures does not produce multiple images of background objects, but little distortions on them. The phenomenon is then called *weak lensing*, in contrast to the *strong lensing*, where multiple images of background sources appear (even if they are not resolved, as in the case of *microlensing*). In Chapter 7 we analyse the weak lensing produced by the galaxy cluster Cl 0024+1654 and present in more detail some of the theoretical aspects needed in the weak lensing regime.

Chapter 3

Recent progress in gravitational lensing: a context for this thesis

In this Chapter we briefly review some of the recent progress made in aspects of gravitational lensing related to this thesis. It intends to be a complement to the individual introductions of each chapter, but it is not a full description of all the methods and ideas in gravitational lensing. Details on a particular issue can be found in the references.

Thus, we focus on the time delay measurements of lensed quasars and on the different problems that appear in their determinations (Part II). In Chapter 2 we learned that the Hubble constant can be estimated knowing the time delay, via a model for the lens. Unfortunately, depending on the lens modelling, the Hubble constant gets different values. A great improvement has been done in the way we understand different lensing potentials and their connection with the Hubble constant and we illustrate this fact using recent literature. Microlensing can be a tool for revealing substructure in lens galaxies or seen as a problem regarding time delay estimates. Moreover, various mechanisms can induce fluctuations in the quasar lightcurves that mimic microlensing. Several cases where this happens will be reviewed as well.

The application of gravitational lensing to clusters of galaxies is also an important part of this thesis (Part III). Both strong (giant arcs) and weak (little distortions) lensing regimes are of interest in galaxy cluster lensing (see Section 2.2.4 for a discussion of these different regimes). These two approaches are complementary: the strong lensing describes the potential inside (or near) the Einstein ring of the cluster, whereas the weak lensing extends to the outer parts of it. Thus, we can have independent estimates of cluster masses. These estimates are then compared to those obtained with X-ray measurements. We present here some comparisons between lensing and X-ray estimates and methods.

There are other aspects of microlensing and weak lensing which are not treated in parts II and III of the thesis. As an overview we offer in the last section of this Chapter a brief description of these other lensing scenarios.

3.1 Lensed quasars, time delays, the Hubble constant and microlensing

In this Section we briefly review the recent improvements made in time delay measurements and Hubble constant estimates from lensed quasars and describe the problems associated with them and some of the solutions proposed.

After Refsdal (1964a, b) found that time delays in multiple quasars are related to the Hubble constant H_0, a new door was opened to have an independent and non-local estimate of this important constant. Nevertheless, in spite of the apparent simple connection that Refsdal showed (see Section 2.2.3), we have not yet firmly established the value of the Hubble constant – up to an error of a few percent –, nor with gravitational lensing theory, nor with any other approach.

Nowadays, there are around 80 gravitationally lensed quasars known[1]. From those, we 'only' know the time delay in 10 of them (see Table 3.1; we do not include the system HE 1104−1805 in this list, but its time delay is discussed in Chapter 4). The reason why the number of known time delays is so low is not strictly scientific: semi-dedicated telescopes are required to monitor the systems during periods that can be of the order of years and modern projects in astronomy demand quick results in relatively short-time scales. A longer term ($\sim$10 years) international project on time delays would produce a giant scientific output, but the organizing strategy is a challenge.

Apart from these 'organizational' difficulties, some mathematical and physical problems might also arise when estimating time delays. The time delay determination in a system is done by comparing the intrinsic variability of of the lensed quasar in two different images. The method consists in checking which features are identical in the lightcurves of these two images. Usual problems when treating with discrete signals might arise. These problems can be divided in two main groups: sampling and additional noise to the signal. The sampling of the signal can be affected by bad weather conditions, seasonal gaps and observational/technical problems (in Chapter 4 we discuss problems of sampling in more detail). Regarding the time delay, microlensing can be considered as 'noise' (Burud et al. 2001; B1600+434: Burud et al. 2000; RX J0911.4+0551: Hjorth et al. 2002; HE 1104−1805: Schechter et al. 2003; HE 0435−1223: Wisotzki et al. 2003), differential extintion (HE 0512−3329: Wucknitz et al. 2003) or random/instrumental artifacts (e.g., Q0957+561: Chapter 5 in this thesis and Colley et al. 2003a). Moreover, a few authors (Goicoechea 2002; Ovaldsen et al. 2003) claimed the possibility of multiple time delays in the double quasar Q0954+561 (with a difference of 15 days, not significant for H_0 estimates). This could be solved using the idea by Yonehara (1999) that different violent events can take place in different regions of the source, inducing different measurements of a time delay.

So, in principle, one could argue that problems with time delays estimates can be easily solved in most of the cases and that the determination of the Hubble constant should be a straightforward task. Nevertheless, this is not so. And the reason is that the gravitational potential to describe the lens is not, in general, well constrained (see, e.g., Keeton et al. 2000).

Various authors found that many individual lenses are consistent with isothermal models – which explain the observed flat rotation curves in galaxies – (Maoz & Rix 1993; Kochanek 1995, 1996; Grogin & Narayan 1996). Moreover, Witt, Mao & Keeton (2000) showed that all these isothermal models can be included in a more general family of potentials, finding an expression

[1] A up-to-date database with gravitationally lensed quasars can be found in http://cfa-www.harvard.edu/castles/

for the time delay as

$$\Delta\mathcal{T}_{ij} = \frac{D_d D_s}{2cD_{ds}}(1+z_d)(r_j^2 - r_i^2) \tag{3.1}$$

where $r_i = (x_i^2 + y_j^2)^{1/2}$ is the distance of the image i to the centre of the lens galaxy (compare this expression with Equation 2.32). Thus, the time delay in expression 3.1 can be calculated only with observables and does not need any fitting procedure, and includes both singular isothermal elliptical potentials and singular isothermal elliptical density distributions. They also explained how the presence of shear introduces uncertainties in the time delays (and in H_0) and that if non-isothermal models are required then numerical modeling is needed.

In spite of this effort, many of the lenses with measured time delays still have large degeneracies between the Hubble constant and the distribution of the lens potential. Kochanek, Keeton & McLeod (2001) broke these degeneracies by using the infrared Einstein ring observed in the systems PG1115+080 (Impey et al. 1998), B1608+656 (Fassnacht et al. 1996) and B1938+666 (King et al. 1997) and assuming elliptical symmetry for the sources. In this way, if Einstein rings are detected (Q2237+0305: Mediavilla et al. 1998; 1RXSJ113155.4−123155: Sluse et al. 2003; MG 1549+305: Treu & Koopmans 2003), then the lens potential can be much better constrained. In addition, Saha & Williams (2003) demonstrated that some characteristics (the time-ordering of the images, the orientation of the lens potential, the morphology of the possible ring) in multiply imaged quasars are model independent.

Kochanek (2002) showed that the inferred value of the Hubble constant strongly depends on whether the lenses have isothermal mass distributions (corresponding to flat rotation curves) or constant mass-to-light (M/L) ratios. In the former case, the value of the Hubble constant is relatively low $H_0 = (48 \pm 3)$ km s^{-1} Mpc^{-1} and in the latter $H_0 = (71 \pm 3)$ km s^{-1} Mpc^{-1} (see Kochanek & Schechter 2003), a value that agrees with that obtained by the HST Key Project (Freedman et al. 2001).

Microlensing signals have been observed in several lensed quasars and used to extract information on the systems in different ways. In the first discovered lensed quasar, the double Q0957+561 (Walsh et al. 1979), microlensing is somehow controversial. Several authors have claimed long term microlensing variability (of the order of years) is present (Falco et al. 1991, Pelt et al. 1998; see also another interpretation in Gil-Merino et al. 1998). Microlensing on short-time scales (from days to weeks) in this system has been claimed by Schild & Thomson (1995), Schild (1996), Colley & Schild (2000), Colley et al. (2003b) and Ovaldsen et al. (2003). On the other hand, Schmidt & Wambsganss (1998) did not find any short term microlensing signal. These authors used the amplitude of the difference lightcurves to put limits on the mass of the microlenses (MACHOs). In Chapter 5, we report an analysis of the system where no short-time scale microlensing fluctuations were found and, moreover, we found the existing fluctuations were due to noise processes (Gil-Merino et al. 2001).

In the system Q2237+0305 there is a general agreement that microlensing fluctuations are real (Irwin et al. 1989, Corrigan 1991, Witt & Mao 1994, Schmidt et al. 2002). Observational microlensing in this system has been used to put limits on the source size, the transverse velocity of the lens and the velocity dispersion and mass function of the microlenses (Wambsganss et al. 1990, Webster et al. 1991, Foltz et al. 1992, Yonehara et al. 1999, 2001, Wyithe et al. 1999, 2000a, 2000b). Also some authors have analysed the spectral variability induced by microlensing (Schneider & Wambsganss 1990, Lewis et al. 1996, Abajas et al. 2002, Popović et al. 2003).

Name	N_{images}	$\Delta\mathcal{T}$ (days)	Band	Ref.
B0218+357	2	10.5±0.2	radio	[1]
Q0957+561	2	425±4	optical	[2]
SBS1520+530	2	130±3	optical	[3]
B1600+434	2	51±2	optical/radio	[4]
PKS1830−211	2	26±4	radio	[5]
HE2149−2745	2	103±12	optical	[6]
RXJ0911+0551	4	146±4	optical	[7]
PG1115+080	4	25±2	optical	[8]
B1422+231	4	8±3	radio	[9]
B1608+656	4	77±2	radio	[10]

Table 3.1: A total number of 10 time delays are known in different lensed quasars. N_{images} is the number of images and $\Delta\mathcal{T}$ is the longest time delay when more than two images are seen. The errors are 1σ. Band indicates the spectral range in which the time delay was obtained. The references (Ref.) are: [1] Biggs et al. (1999); [2] Serra-Ricart et al. (1999), see also Pelt et al. (1994, 1996), Oscoz et al. (1996, 1997), Kundic et al. (1997), Pijpers (1997), Schild & Thomson (1997), Haarsma et al. (1997, 1999); [3] Burud et al. (2002b); [4] Burud et al. (2000), Koopmans et al. (2000); [5] Lovell et al. (1998); [6] Burud et al. (2002a); [7] Hjorth et al. (2002); [8] Barkana (1997); [9] Patnaik & Narasimha (2001); [10] Fassnacht et al. (2002)

In Chapter 6, we analyse the system Q2237+0305 (Gil-Merino et. al 2002a). Two images did not show strong microlensing signals during the monitoring. We use this fact to put limits on the effective transverse velocity of the lens galaxy.

The double quasar HE 1104−1805 is a more complicated system. It was discovered by Wisotzki et al. (1993) and the first time delay estimate ($\Delta\mathcal{T} = 0.75$ yrs, without error estimates) reported by Wisotzki et al. (1998). In these works clear indications of microlensing were found (see also Courbin et al. 2000). Gil-Merino et al. (2002b) presented a new time delay determination ($\Delta\mathcal{T} = 310 \pm 20$ days, 2σ errors; see Chapter 4) based on poorly sampled light curves and applying a number of techniques. Pelt et al. (2002) argued that the error bars of the time delay reported by Gil-Merino et al. could be underestimated. Schechter et al. (2003) published a three years observation of HE 1104−1805 but, due to the strong microlensing signal, were unable to establish a time delay for the system. Instead, they analysed a wide range of different phenomena that might originate such a microlensing signal: dark matter dilution, hot spots in the quasar accretion disk, microlensing with planetary masses and cold spots. They concluded that a model with multiple hot spots should not be excluded, while the rest of the processes were unlikely. Finally, in a very recent paper Ofek & Maoz (2003), adding two years of observations to the Schechter et al. dataset, obtained a new time delay of $\Delta\mathcal{T} = 161 \pm 7$ days (1σ errors).

Microlensing has been also detected in some other systems. Koopmanns & de Bruyn (2000) found short-time scale fluctuations due to microlensing in the double radio system B1600+434 and ruled out other sources of variability, like scattering by the ionized component of the Galactic interstellar medium (scintillation). Wucknitz et al. (2003) analysed the double quasar HE 0512−3329, finding a flux ratio of the components strongly dependent on wavelength. They found that both

microlensing and differential extinction (differential reddening caused by different extinction effects) were present. Recently, Wisotzki et al. (2003) presented an integral-field spectrophotometry of the quadruple quasar HE 03435−1223, finding evidence for microlensing.

Section summary: this Section is a context to the Part II of this thesis. There we present results concerning three lensed quasar systems: HE 1104−1805, Q0957+561 and Q2237+0305. In the first system, the time delay is estimated, discussed and compared with other very recent estimates and the Hubble constant is also inferred from this time delay. Microlensing studies of a system are done analysing the difference light curves between the components. Such an analysis helps to understand various physical properties of the system, like the mass distribution in the lens galaxy and the size of the source. But sometimes a spurious signal is attributed to microlensing and wrong conclusions might be obtained. We use the system Q0957+561 to show some problems when analysing difference light curves that were not previously pointed out. The system Q2237+0305 has been showing an unambiguous microlensing signal during several monitoring campaigns. Such a signal has been used to put limits on the masses of the microlenses, on the source size and on the transverse velocity of the lens. We use a novel approach to put limits to the transverse velocity of the source, making use of the low amplitude microlensing signal during four months of monitoring.

3.2 Galaxy clusters lensing and X-rays observations

The study of clusters of galaxies provides deep inside in cosmology: the large-scale structure formation, the content of baryon and dark matter in the Universe or how galaxies form and evolve are some of the topics related. In this section we review some of the ways in which gravitational lensing can extract information from clusters of galaxies and their X-ray properties. Two excellent reviews on galaxy cluster lensing by large structures are Mellier (1999) and Bartelmann & Schneider (2001).

If a distant galaxy sits near a caustic (lines of infinite magnification, see Section 2.2.2) due to a foreground lens, then a large gravitationally lensed arc is seen. The first giant arcs produced by galaxy clusters were detected by Lynds & Petrosian (1987, 1989) in the clusters A370 and Cl 2244−02 and by Soucail et al. (1987, 1988) in A370. The suggestion that these could in fact be gravitational mirages was made by Paczyński (1987) and analysed by computer simulations by Grossman & Narayan (1988), concluding that the lensing hypothesis was very likely. How to use these arclets and multiple images produced by galaxy clusters to get the mass distribution in these objects is discussed in detail in Fort & Mellier (1994). These authors showed that the arc-like lensed images were produced by the core of the clusters or by compact clumps of galaxies and that the mass distributions in these regions could be reconstructed modeling the lens potential. They found typical mass-to-light ratio M/L_B =300 h_{100} within the radius of the arcs[2] (i.e. inside the Einstein radius of the cluster). In order to reproduce the multiple images with models, some substructure in form of dark matter is required surrounding the brightest galaxies or in clumps with ellipticities following the isophotes of these galaxies (Hammer & Rigaud 1989: A370 and Cl 2244−02; Mellier et al. 1993: MS 2137−23; Kneib et al. 1993: A370; Kneib et al. 1995: A2218). All these authors found that the core radius of the dark matter distribution is small, $< 50h_{100}^{-1}$ kpc (see also Mellier 1999). These conclusions were independently confirmed by later

[2]The value of h is defined in terms of the Hubble constant $H_0 = 100h_{100}$ km s^{-1} Mpc^{-1}

observations using the Hubble Space Telescope (HST; e.g., Gioia et al. 1998: MS 0440+0204; Tyson et al. 1998: Cl 0024+1654. More recent mass recontructions using strong lensing are e.g. Broadhurst et al. (2000; on the central mass distribution in Cl 0024+1654 using HST data from Colley et al. 1996), Athreya et al. (2002; ESO-VLT data on MS 1008−1224) and Gavazzi et al. (2003; on MS 2137.3−2353 using ESO-VLT multiband UBVRIJK data). Theoretical improvement has also been done in the interpretation of these data. Bartelmann & Weiss (1994) explored the statistics of arcs with N-body simulations, finding that the efficiency of arcs productions by clusters was higher than what it was previously estimated. Williams et al. (1999) compared the core structure of galaxy clusters also with N-body simulations of cluster formation in cold dark matter-dominated universes and found that cluster core masses exceed those of dark matter halos of similar velocity dispersion. In the same direction, Bartelmann et al. (1998) concluded that only the open CDM cosmological model can reproduce the observed abundance of arcs. Meneghetti et al. (2003) showed that more realistic analytical models (Navarro et al. 1997 profiles instead of isothermal spheres), rather than simulations, increase the arc probability. Nevertheless, Wambsganss et al. (2003) found, using ray-shooting simulations, that the observed arc abundance might also be compatible with a ΛCDM cosmological model.

Weak lensing by galaxy clusters – little distorsions induced by a cluster on the background galaxies – were first detected by Tyson et al. (1990) in the analysis of two clusters: A1689 and Cl 1409+52. Kaiser & Squires (1993) and Kaiser, Squires & Broadhurst (1995, KSB hereafter) developed an inversion method, using the fact that the ellipticity of the background galaxies provides an estimate of the second derivatives of the potential (see Section 2.2.2), to reconstruct the projected surface mass density of galaxy clusters. This method was then widely applied to different observations (Bonnet et al. 1994: Cl 0024+1654; Fahlman et al 1994: MS 1224.7+2001; Smail et al. 1994, 1995: Cl 1455+22, Cl 0016+16, Cl 1603+43; Tyson & Fisher 1995: A1689). Seitz & Schneider (1995) generalized the method proposed by Kaiser & Squires, trying to avoid the degeneracies of critical clusters. Bartelmann et al. (1996) proposed a different method to reconstruct both the cluster morphology and its total mass. The method, called maximum-likelihood reconstruction, is based on a least-χ^2 fit to the 2-dimensional gravitational potential of the cluster (see also Squires & Kaiser 1996 and Bridle et al. 1996). Seitz et al. (1998) improved the maximum-likelihood method using the individual ellipticities of each galaxy, instead of smoothing the data. Hoekstra et al. (1998) slightly modified the method by KSB, improving the way in which image moments are calculated. This method is used in Chapter 7 and explained in more detail there.

The inversion methods reconstruct the projected surface mass density up to an additional constant, because by adding a lens plane of constant mass density, the distortions of galaxies do not change (Gorenstein et al. 1988). In order to break this degeneracy, the so-called *mass-sheet degeneracy*, Broadhurst et al. (1995) proposed to calculate the magnification from the local modification of the galaxy number density (the *magnification bias*). The magnification is not invariant under the addition of a constant mass density plane so, in this way, the degeneracy is broken if the magnification is known. Bartelmann & Narayan (1995) proposed to compare the angular sizes of lensed galaxies with an unlensed sample (the *lens parallax method*) to break the mass-sheet degeneracy. The use of wide-field camaras covering fields larger than the clusters, would introduce boundary conditions to the surface mass density (because it should vanish at the boundaries of the field) and thus breaking the degeneracy as well (Mellier 1999). Recently, Athreya et al. (2002) used photometric redshifts of the background sources from multiband photometry to scale the mass of the

cluster. We use this last method in Chapter 7 and apply it to the galaxy cluster Cl 0024+1654.

The mass of galaxy clusters can also be derived from the distribution of their intracluster X-ray emitting gas, assuming the gas is in hydrostatic equilibrium. In principle, this assumption is reasonable as long as the cluster is stationary and forces other than gas pressure and gravity are not important (Sarazin 1988). Comparison between X-ray and lensing mass estimates has proved to be a difficult task and the results are puzzling. This mass discrepancy problem has been reported by many authors in several clusters. Miralda-Escudé & Babul (1995) found that $M_{\rm lensing} \approx 2\text{-}3 M_X$ in the clusters A2218 and A1698. These authors explored a number of possibilities for this discrepancy, finding as the more likely ones projection effects (clumping), temperature profiles toward the center (i.e. not constant temperatures), multiphase intracluster gas and nonthermal pressure (magnetic fields and/or bulk motions). Schindler et al. (1997) found a similar discrepancy in the cluster RX 1347.4−1145 and concluded that the reason could also be the presence of substructure or/and magnetic fields. Wu & Fang (1997) found the same effect in a statistical sample of 29 clusters and thought that the discrepancy arose from the simplification in the models for the X-ray gas distribution and dynamical evolution. Similar problems were found by Ota et al. (1998) in Cl 0500−24, Cl 2244−02 and A370 and Soucail et al. (2000) in Cl 0024+1654. On the other side, some authors find quite different results. Böhringer et al. (1998) found a very good agreement between $M_{\rm lensing}$ and M_X in the cluster A2390, interpreting this result as a more relaxed status of the cluster than in other cases. Although the mass discrepancy problem is not yet definitively explained, it seems that wrong assumptions on the physical state of the cluster and/or some other physical processes need to be considered (Allen 1998).

Section summary: in this Section we give a context for Part III of this thesis. There we analyse the clusters of galaxies Cl 0024+1654 and RBS380. The former is one of the most studied clusters. We use weak lensing analysis to obtain the mass, luminosity and mass-to-light profiles. The advantage of our data is the multiband photometry on filters BVRIJK, which allows to estimate the photometric redshifts of the background sources and thus break the degeneracy in the mass determination. The cluster RBS380 is the more distant cluster in the ROSAT Bright Source (RBS) catalog. We observe this system trying to find gravitational arcs of background galaxies and we found none. The reason might be that previous estimates of its mass were too high.

3.3 Other lensing scenarios

There are many other scenarios in which gravitational lensing is applied. These are not discussed in this thesis, but they are also active research fields. We mention some of them.

Microlensing in individual quasars: Hawkins (1993) and Hawkins & Taylor (1997) argued that the variability of individual quasars might be due to microlensing. This possibility is hard to be confirmed, because quasars are intrinsically variable. Moreover, the expected microlensing in single quasars is smaller than in multiple ones, since the surface mass density is lower (Wambsganss 2001).

Galactic microlensing: The importance of microlensing at low surface mass densities was first pointed out by Paczyński (1986b), suggesting the monitoring of stars in the Large Magellanic Cloud to catch microlensing events by compact objects in our galaxy. Several collaborations have existed since then searching for halo compact objects, binaries and planets: *MACHO* (Alcock et

al. 1993), *EROS* (Aubourg et al. 1993) and *OGLE* (Udalski et al. 1993). Still active collaborations are *OGLE*, *MOA* (Bond et al. 2003), *PLANET* (Albrow et al. 1998) and *MicroFUN*[3].

Astrometric microlensing: Lewis & Ibata (1998) showed that microlensing of quasars by stars in external galaxies can introduce fluctuations in the centroid of the macroimages. Although this shift is very small (microarcsecond scales), it should be possible to be measured with the Space Interferometry Mission (SIM, planned for 2006) and it will help to reveal the quasar structure and the stellar mass function of the lensing galaxy (see also Boden et al. 1998 and references therein). For more 'exotic' microlensing (like *parallax* and xallarap events), see Evans 2003 and references therein.

Galaxy-galaxy lensing: Galaxies at cosmological distances can be lensed by foreground galaxies (which in principle do not need to be physically related, in groups or clusters). The weak lensing techniques already described are not valid in this case, because individual galaxies are not massive enough to produce measurable distortion of background galaxies. The effect of several foreground galaxies has to be statistically taken into account. In this way the properties of dark matter halos of population of galaxies can be investigated. The first report on galaxy-galaxy lensing was made by Brainerd, Blandford & Smail (1996). Several surveys have been carried out in this direction. Recent works are Smith et al. (2001) and Hoekstra et al. (2003).

Lensing by large-scale structures: Background galaxies can be lensed by large-scale structures in the Universe. The effect is an induced correlation of the ellipticity distribution of the lensed sources. The analysis of this *cosmic shear* reveals information on the geometry of the space-time (giving information on Ω_M and Ω_Λ) and on the power spectrum of the matter density perturbation which induce the distortions. First works in this aspect of lensing are Blandford et al. (1991), Miralda-Escudé (1991) and Kaiser (1992). More recent discussions can be found in Van Waerbeke et al. (2001) and Maoli et al. (2001). Cosmic strings and, in general, topological defects (see Vilenkin & Shellard 1994) have been investigated as gravitational lenses as well (Bernardeau & Uzan 2001, Uzan & Bernardeau 2001).

Lensing and the CMB: In the same way in which large structures induce distortions on background galaxies, the Cosmic Microwave Background (CMB) can suffer lensing effects. The structures of the CMB maps (temperature anisotropies) will be stretched in the direction of the gravitational lenses. The effect is, however, very small and careful analysis is required because of the low signal-to-noise ratios of the lens contributions. A review of this topic can be found in Mellier (1999).

Section summary: in this last section we briefly review aspects of lensing which are not treated in this thesis. Although the analysis is not exhaustive, the references provide further readings for the interested reader. We have briefly reviewed other aspects of microlensing – from individual quasars, in the Milky Way and the one due to shifts in the centroids of the macroimages (astrometric) – and also other weak lensing scenarios – galaxy-galaxy, large-scale structures and effects in the CMB –.

[3] http://www.astronomy.ohio-state.edu/∼microfun/

Part II

Quasar Lensing and Microlensing

Chapter 4

Time delay techniques: a comparative analysis via the case study of the double quasar HE 1104−1805⋆

Link. *Once a multiple image quasar is identified as a gravitationally lensed system, researchers want to study it in more detail. The best way of doing so is carring out a monitoring campaign, in which one will obtain a lightcurve for each quasar image. Prior to the analysis of the differences between those components, one has to apply a time delay correction to them. Although in principle the time delay estimation for a system could appear a very simple task, this is not the case in most of the situations: seasonal gaps, bad weather conditions, light contamination of many types and/or poor sampling can induce wrong estimates of the time delays between the components. In this chapter we analyse an extreme case where the sampling was very poor and check the behaviour of a number of different available techniques.*

Abstract. A new determination of the time delay of the gravitational lens system HE 1104−1805 ('Double Hamburger') is presented. A possible bias of the technique used in the previously published value of $\Delta t_{A-B} = 0.73$ years is discussed. We determine a new value of $\Delta t_{A-B} = (0.85 \pm 0.05)$ years (2σ confidence level), using six different techniques based on non interpolation methods in the time domain. The result demonstrates that even in the case of poorly sampled lightcurves, useful information can be obtained with regard to the time delay. The error estimates were calculated through Monte Carlo simulations. With two already existing models for the lens and using its recently measured redshift, we infer a range of values of the Hubble parameter: $H_0 = (48 \pm 4)\ \mathrm{km\ s^{-1}\ Mpc^{-1}}$ (2σ) for a singular isothermal ellipsoid (SIE) and $H_0 = (62 \pm 4)\ \mathrm{km\ s^{-1}\ Mpc^{-1}}$ (2σ) for a constant mass-to-light ratio plus shear model ($M/L+\gamma$). The possibly much larger errors due to systematic uncertainties in modeling the lens potential are not included in this error estimate.

⋆Chapter based on the refereed publication Gil-Merino, Wisotzki & Wambsganss, 2002, A&A, 381, 428

4.1 Introduction

The double quasar HE 1104−1805 at a redshift of $z_Q = 2.319$ was originally discovered by Wisotzki et al. (1993). The two images with (original) B magnitudes of 16.70 and 18.64 are separated by $3''.195$ (Kochanek et al. 1998). The spectral line ratios and profiles turned out to be almost identical between the two images, but image A has a distinctly harder continuum. Wisotzki et al. (1995) report about a dimming of both components over about 20 months, accompanied by a softening of the continuum slope of both images. The lensing galaxy was discovered by Courbin et al. (1998) in the NIR and by Remy et al. (1998) with HST. The authors tentatively identified the lensing galaxy with a previously detected damped Lyman alpha system at $z = 1.66$ (Wisotzki et al. 1993; Smette et al. 1995; Lopez et al. 1999). This identification, however, was disputed by Wisotzki et al. (1998). Using FORS2 at the VLT, Lidman et al. (2000) finally determined the redshift of the lensing galaxy to $z_G = (0.729 \pm 0.001)$.

A first determination of the time delay in this system was published by Wisotzki et al. (1998, hereafter W98), based on five years of spectrophotometric monitoring of HE 1104−1805, in which the quasar images varied significantly, while the emission line fluxes appear to have remained constant. The W98 value for the time delay was $\Delta t_{A-B} = 0.73$ years (no formal error bars were reported), but they cautioned that a value as small as 0.3 years could not be excluded.

HE 1104−1805 shows strong and clear indications of gravitational microlensing, in particular based on the continuum variability with the line fluxes almost unaffected (Wisotzki et al. 1993, Courbin et al. 2000).

Here we present an analysis of previously unpublished photometric monitoring data of HE 1104-−1805. First the data and light curves are presented (Sect. 4.2), then a number of numerical techniques are described and discussed and, as the scope of this Chapter is a comparison of different techniques in the case of poorly sampled data, we finally applied to this data set, in order to determine the time delay (Sect. 4.3). A discussion of the results and the implications for the value of the Hubble constant based on this new value of the time delay and on previously avalaible lens models are given in Sect. 4.4. In Sect. 4.5 we present our conclusions.

4.2 Data acquisition and reduction

Between 1993 and 1998, a B band lightcurve of HE 1104−1805 at 19 independent epochs was obtained, mostly in the course of a monitoring campaign conducted at the ESO 3.6 m telescope in service mode. The main intention of the programme was to follow the spectral variations by means of relative spectrophotometry, but at each occasion also at least one frame in the B band was taken. A *continuum* lightcurve, derived from the spectrophotometry, and a first estimate of the time delay were presented by W98, where details of the monitoring can also be found. Here we concentrate on the broad band photometric data (see Table 4.1). Images were taken typically once a month during the visibility period. The instrument used was EFOSC1 with a 512×512 pixels Tektronix CCD until June 1997, and EFOSC2 with a 2K×2K Loral/Lesser chip afterwards. The B band frames (which were also used as acquisition images for the spectroscopy) were always exposed for 30 seconds, which ensured that also the main comparison stars were unsaturated at the best recorded seeing of $1''$. Sometimes more than one exposure was made, enabling us to make independent estimates of the photometric uncertainties. A journal of the observations is presented together with the

measured lightcurve in Tab. 4.1. The CCD frames were reduced in a homogeneous way following standard procedures. After debiasing and flatfielding, photometry of all sources in the field was conducted using the DAOPHOT II package (Stetson 1987) as implemented into ESO-MIDAS. The instrumental magnitudes of the QSO components and reference stars 1–5 (following the nomenclature of Wisotzki et al. 1995) were recorded and placed on a homogeneous relative magnitude scale defined by the variance-weighted averages over all comparison stars. In Fig. 4.1 we show the resulting QSO lightcurves, together with the two brightest comparison stars. The variability of both QSO components is highly significant, including strong fluctuations on the barely sampled timescales of months. This behaviour is stronger in component A, while component B leads the variability. The error estimates include shot noise, PSF fitting uncertainties and standard deviations in case of multiple images at a given epoch. Note the similarity of these B band data with the completely independently calibrated continuum lightcurves of W98.

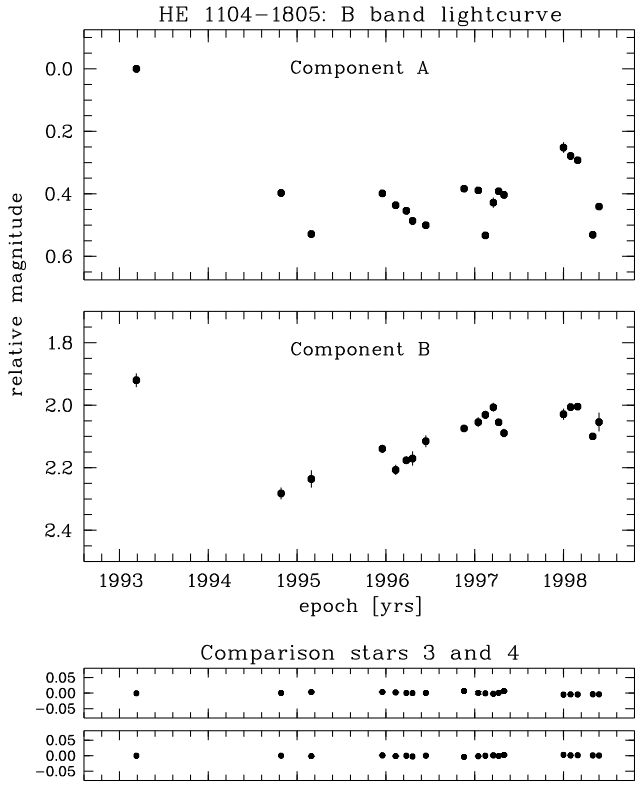

FIGURE 4.1: The new photometric dataset running from 1993 to 1998. The zero point for the relative photometry of HE 1104−1805 is the first data point of component A (see Table 4.1 for error estimates).

4.3 Time Delay Determination

4.3.1 Dispersion spectra method

A first estimation for the time delay in this system resulted in a value of $\Delta t_{B-A} = -0.73$ years (W98), using the dispersion spectra method developed by Pelt et al. (1994, 1996; hereafter P94

Epoch [yrs]	ΔB_A	σ_{B_A}	ΔB_B	σ_{B_B}
1993.19	0.000	0.009	1.920	0.022
1994.82	0.397	0.009	2.282	0.019
1995.16	0.529	0.008	2.236	0.028
1995.96	0.399	0.012	2.140	0.014
1996.11	0.436	0.008	2.207	0.017
1996.23	0.454	0.005	2.176	0.013
1996.30	0.486	0.009	2.171	0.023
1996.45	0.500	0.008	2.115	0.019
1996.88	0.383	0.007	2.074	0.012
1997.04	0.389	0.007	2.054	0.016
1997.12	0.533	0.009	2.031	0.013
1997.21	0.428	0.016	2.007	0.015
1997.27	0.392	0.007	2.055	0.012
1997.33	0.403	0.008	2.089	0.014
1998.00	0.252	0.017	2.029	0.018
1998.08	0.279	0.004	2.006	0.011
1998.16	0.292	0.004	2.004	0.011
1998.33	0.531	0.006	2.100	0.011
1998.40	0.441	0.007	2.054	0.030

Table 4.1: B band lightcurve data for HE 1104−1805. The first measurement of component A has arbitrarily been set to zero. The error estimates include shot noise, PSF fitting uncertainties, and also standard deviations in case of multiple shoots at a given epoch.

and P96, respectively). Note that we will express the time delay as Δt_{B-A} (instead of Δt_{A-B}), since B leads the variability (see Fig. 4.1), and thus there appears a minus sign in the result. We shall demonstrate below that the dispersion spectra method is not bias-free. To facilitate a better understanding of this claim, we first briefly describe the method in the following: The two time series A_i and B_j can be expressed in magnitudes, using the P96 notation, as

$$A_i = q(t_i) + \epsilon_A(t_i), i = 1, ..., N_A \tag{4.1}$$

$$B_j = q(t_j - \tau) + l(t_j) + \epsilon_B(t_j), j = 1, ..., N_B \tag{4.2}$$

$q(t)$ being the intrinsic variability of the quasar, τ the time delay, $l(t)$ the magnitude difference and $\epsilon(t)$ another possible noise component (this could be pure noise or microlensing). Both lightcurves A_i and B_j are combined into a new one, C_k, for each value of the pair $(\tau, l(t))$, 'correcting' the B_j series by $l(t)$ in magnitudes and by τ in time

$$C_k(t_k) = \begin{cases} A_i & \text{if } t_k = t_i \\ B_j - l(t_j) & \text{if } t_k = t_j - \tau \end{cases} , \tag{4.3}$$

with $k = 1, ..., N$ and $N = N_A + N_B$. Then the dispersion spectrum is calculated analytically by the expression

$$D^2_{4,k} = \min_{l(t)} \frac{\sum_{n=1}^{N-1} \sum_{m=n+1}^{N} S^{(k)}_{n,m} W_{n,m} G_{n,m} (C_n - C_m)^2}{\sum_{n=1}^{N-1} \sum_{m=n+1}^{N} S^{(k)}_{n,m} W_{n,m} G_{n,m}}, \tag{4.4}$$

where $W_{n,m}$ are the statistical weights; $G_{n,m} = 1$ if the points C_n and C_m come from different time series, A_i or B_j, and 0 otherwise; and $S^{(k)}_{n,m}$ is a function that weights each difference $(C_n - C_m)$ depending on the distance between the points. In P96 they show three possible definitions for this function, here we have selected

$$S^{(2)}_{n,m} = \begin{cases} 1 - \frac{|t_n - t_m|}{\delta} & \text{if } |t_n - t_m| \leq \delta \\ 0 & \text{if } |t_n - t_m| > \delta \end{cases}, \tag{4.5}$$

which includes those pairs for which the distance between two observations is less than a certain *decorrelation length* δ. More details can be found in P94 and P96. The definition of this function here is slightly different from the one used in W98. We have two reasons to do so: first, we will demonstrate that the selection of one or another definition does not play a crucial role in this case; second, the function $S^{(3)}_{n,m}$ used in W98 is supposed to avoid the problem of having big gaps between the observational points in the lightcurves, but we will try to solve this problem in a different way.

The new dataset used here has the same sampling as the one used for the first estimation of the time delay in W98. As the errorbars for individual points are also very similar, one should expect to obtain a similar time delay. And in fact this is exactly what happens when applying the dispersion spectra method as described above. The original dataset is plotted in Fig. 4.1. There are 19 observational points for each component. We apply the dispersion spectra method (P94, P96): the result is $\Delta t_{B-A} = -0.73$ years, i.e., the same value as the first published estimation.

Since W98 did not provide a formal error estimate, we now investigate the goodness of this value and try to estimate the uncertainty, and we also want to check the self-consistency of the method in this case. For this purpose we do a test based on an iterative procedure: after having applied the dispersion spectra method to the whole data set, we make a selection of the data trying to avoid big gaps between the epochs and considering points in both lightcurves that fall in the same time interval once one has corrected the time shift with the derived time delay. This will avoid the so-called border effects, and a time delay close to the initial one should result when the dispersion spectra are recalculated for the selected data. We do this in the next subsection.

4.3.2 Borders and gaps

We first consider $\Delta t_{B-A} = -0.73$ years as a rough estimate of the time delay, in agreement with W98. It is obvious that using this time delay, the first point of the whole dataset (epoch 1993.19) of component B has no close partner in component A. Eliminating this point means avoiding the big gap of almost two years at the beginning of the lightcurves. Once this is done, the last five points of the lightcurve B and the first two ones of A (after eliminating the epoch 1993.19) are not useful anymore for a time delay determination since they do not cover the same intrinsic time interval.

We also eliminate these points. Now we have a 'clean' dataset with 16 points from component A and 13 points from component B. The situation is illustrated in Fig. 4.2, where only the epochs inside the time interval [1994.5, 1998.0] are plotted. This is the time interval for which the two lightcurves overlap after the -0.73 years correction for component A.

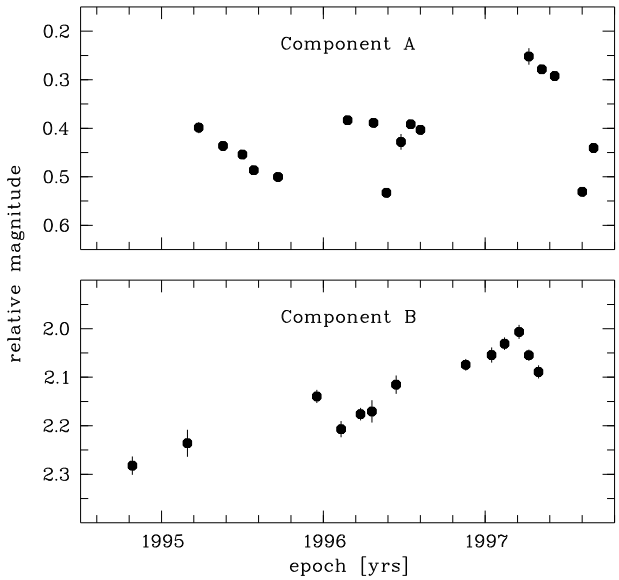

FIGURE 4.2: The first point of the whole dataset has been removed and the points that do not fall in the same time interval once we have shifted the A lightcurve with the value of the first time delay estimation, $\Delta t_{B-A} = -0.73$ years. Thus component A has now 16 points and component B 13 points. If the procedure were self-consistent and the first time delay estimation right, we would naturaly expect a confirmation of this value in a second measurement of the delay by using the new dataset.

Now we again apply the dispersion spectra method to the 'clean' dataset, i.e. a second iteration is made. The result is surprising: $\Delta t_{B-A} = -0.38$ years. The technique should converge to a value near to that of the first result, if the previous estimation was correct and the technique is self-consistent. For consistency, we repeat this analysis assuming a time delay of -0.38 years, i.e., a third iteration. The result is again unexpected: we recover the previous value of -0.73 years. These results can be seen in Fig. 4.3, upper panel (dispersion with all points), middle panel (borders and gap corrected around 1 year) and bottom panel (borders and gap corrected around half a year) where the minimum of the function gives the time delay. The solid and broken lines in each figure correspond to two slightly different decorrelation lengths ($\delta_1 = 0.3$ years, $\delta_2 = 0.4$ years).

This clearly means that the method is not self-consistent when applying it to the current data set. The dispersion spectra method is very sensitive to individual points, and in poorly sampled sets such as this one, these points are critical. It is obvious that we need better techniques for the determination of the time delay. But these techniques must not be interpolating ones because the lightcurves have lots of variability and wide gaps, and any simple interpolation scheme might introduce spurious signals.

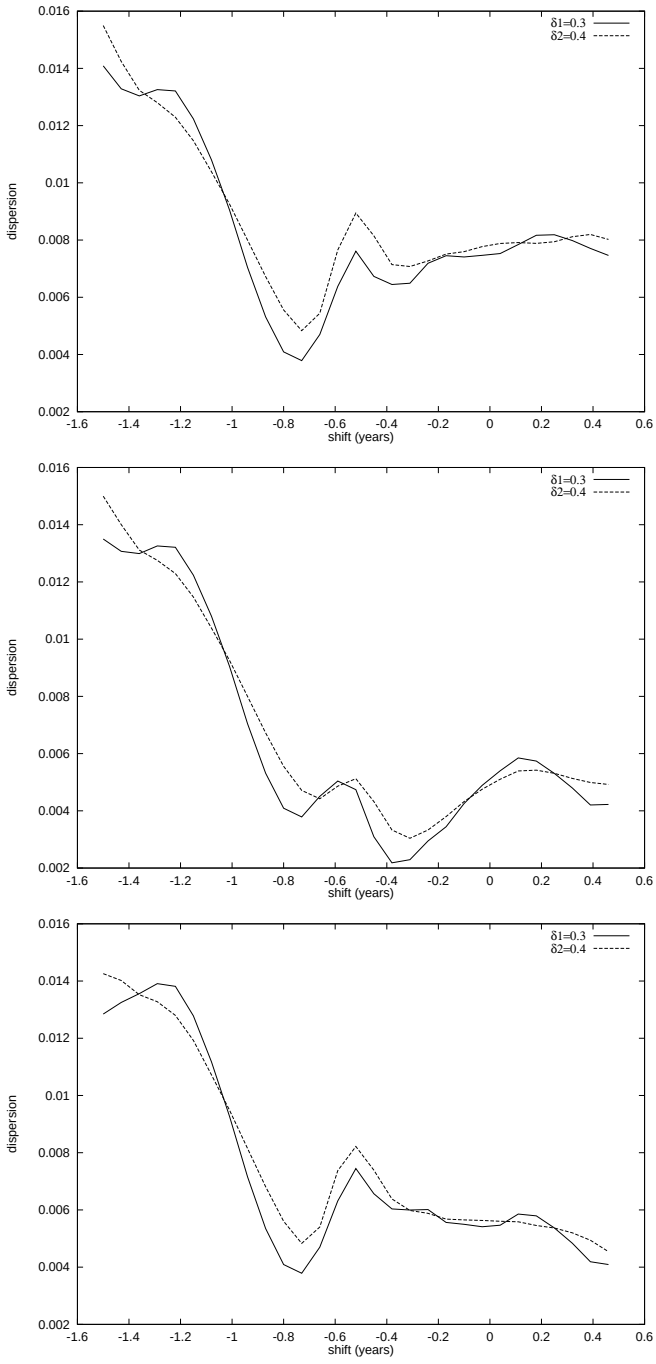

FIGURE 4.3: Dispersion spectra: The *upper panel* shows the result when all the points are taken into account. In the *middle panel*, the result after correcting borders with the first estimation of the time delay, i.e. $\Delta t_{B-A} = -0.73$ years. In the *bottom panel* we use a correction of -0.38 years obtained in the middle panel. We recover the previous value for the time delay of $\Delta t_{B-A} = -0.73$ years, showing the inconsistency of the method. In each subfigure, two curves are plotted for two different values of the decorrelation length: solid for $\delta_1 = 0.3$ years and broken for $\delta_2 = 0.4$ years.

4.3.3 Techniques based on the discrete correlation function

4.3.3.1 Reasons for 'clean' datasets

Many authors have applied different versions of the discrete correlation function (DCF) since it was introduced by Edelson & Krolik (1988; hereafter EK88). Here we have selected five of them. These techniques take into account the global behavior of the curves, rather than 'critical points'. But in order to properly apply all these methods one has to eliminate border effects and gaps as described previously. If one does not do this, one will lose signal in the peak of the DCF and secondary peaks could appear, which can bias the final result. We will demonstrate this last point later (Fig. 4.7, described in Sect. 4.3.3.4, is used for this purpose).

4.3.3.2 Standard DCF plus a parabolic fit.

First we apply the usual form of the DCF to the data set. We briefly recall the expression, following EK88:

$$DCF(\tau) = \frac{1}{M} \sum_{ij} \frac{(a_i - \bar{a})(b_j - \bar{b})}{\sqrt{(\sigma_a^2 - \epsilon_a^2)(\sigma_b^2 - \epsilon_b^2)}}, \tag{4.6}$$

where M is the number of data pairs (a_j, b_j) in the bin associated with the lag τ, ϵ_x the measurement error, σ_x the standard deviation and $\bar{x}$ the mean of x. $DCF(\tau)$ gives the cross correlation between both components at lag τ by considering bins that include all pairs of points (a_j, b_j) verifying $\tau - \alpha \leq (t_j - t_i) < \tau + \alpha$, where α is the bin semisize. In DCF-based techniques, one always needs to find a compromise between the bin size and the error for each bin: increasing the former decreases the latter, but resolution with respect to τ is lost. The result of applying this procedure to the HE 1104−1805 data is a function with a few points and without a prominent feature around the peak, because of our sparse sampling. The position of the peak gives the time delay: $\Delta t_{B-A} = -0.91$ years.

A modification of this method was suggested by Lehár et al. (1992). They proposed to fit a parabola to the peak of the function in case the peak is not resolved. Doing this fit, we obtain a time delay of $\Delta t_{B-A} = -0.89$ years. These results are shown in Fig. 4.4. The noise level is computed as $\sqrt{M}$, M being the number of pairs in each bin. The problem in this case is that the peak of the function is defined with only two points above the noise level. We used a bin semisize of $\alpha = 0.07$ years. Increasing the bin semisize to $\alpha = 0.14$ years does not improve the result in the sense that the peak is defined by only one point, and the fit does not modify the location of this peak. The obtained value for the time delay in this case ($\alpha = 0.14$ years) is $\Delta t_{B-A} = -0.84$ years.

4.3.3.3 Locally normalized discrete correlation function: averaging in each bin

The locally normalized discrete correlation function (LNDCF) was also proposed by Lehár et al. (1992). Its main difference to the simple DCF is that it computes the means and variances locally, i.e. in each bin:

$$LNDCF(\tau) = \frac{1}{M} \sum_{ij} \frac{(a_i - \bar{a}_*)(b_j - \bar{b}_*)}{[(\sigma_{a_*}^2 - \epsilon_a^2)(\sigma_{b_*}^2 - \epsilon_b^2)]^{1/2}}, \tag{4.7}$$

computing the sum over all pairs where $\tau - \alpha \leq (t_j - t_i) < \tau + \alpha$. The mean, $\bar{x}_*$, and the standard deviations, $\sigma_{a_*}^2$, are calculated for each bin. Again a parabolic fit is needed for a more accurate

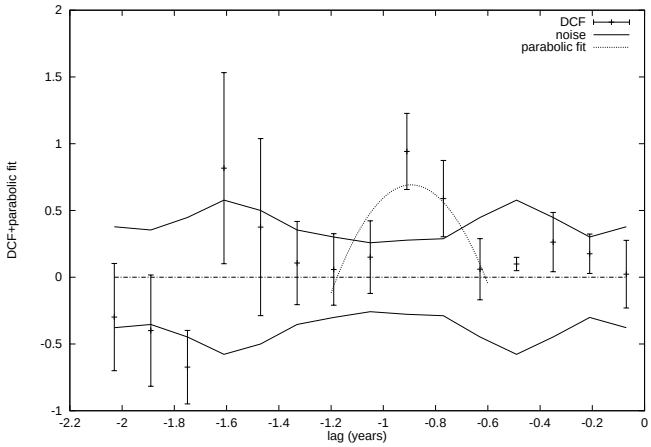

FIGURE 4.4: The standard DCF and an added fit are shown in this figure. The peak is located at -0.89 years (-0.91 without fit) using a bin semisize $=$ 0.07 years. The continuous lines are the noise levels and the zero level is also plotted. Only two points defining the peak are outside the noise band.

value of the peak, which then gives the time delay. For the same reasons as in Sect. 4.3.3.2 we choose a bin semisize $\alpha = 0.07$ years. The result is shown in Fig. 4.5. As in the case of the standard DCF, the peak is just defined by two points. The obtained time delay in this case is $\Delta t_{B-A} = -0.87$ years (the value without the fit is -0.91 years). Furthermore, a secondary competing peak appears at -0.35 years, with more points, although these points have larger errorbars. This is an interesting aspect, because it was this secondary peak which 'confused' the dispersion spectra technique and it may suggest a close relation between these two techniques (both favour 'local' behaviour of the signals, rather than 'global' ones). This possible relation merits more attention and will be investigated in future work. In any case, the poorly defined peak means the technique is again quite sensitive to our poor sampling. We look for a method less sensitive to this problem. The two following techniques are two different ways of trying to solve the problem of not having many points around the prominent peak.

4.3.3.4 Continuously evaluated discrete correlation function: overlapping bins in the DCF

The continuously evaluated discrete correlation function (CEDCF) was introduced by Goicoechea et al. (1998a). The difference to the standard way of computing the DCF in this method is that the bins are non disjoint (i.e. each bin ovelaps with other adjacent bins, see paragraph 4.3.3.2 where the bins do not overlap each other). One has to fix the distance between the centers of the bins in addition to their width. In this way it is possible to evaluate the DCF at more points, having a more continuously distributed curve. We will have also more significant points around the peak, i.e. above the noise level, and there is no need for fitting. Selecting the distance between the centers of the bins is again a matter of compromise: increasing the distance requires wider bins and, thus, loses resolution. The adopted time resolution should depend on the sampling; it seems reasonable to select a value slightly less then the inverse of the highest frequency of sampling ($1/f \simeq 0.1$ years). We choose 0.05 years as the best value for the distance between bin centers and two values for bin semisizes: $\alpha = 0.14$ and $\alpha = 0.21$ years. The overlapping between bins allows us to consider slightly wider bin sizes. We plot the results in Fig. 4.6, upper and lower panel, respectively.

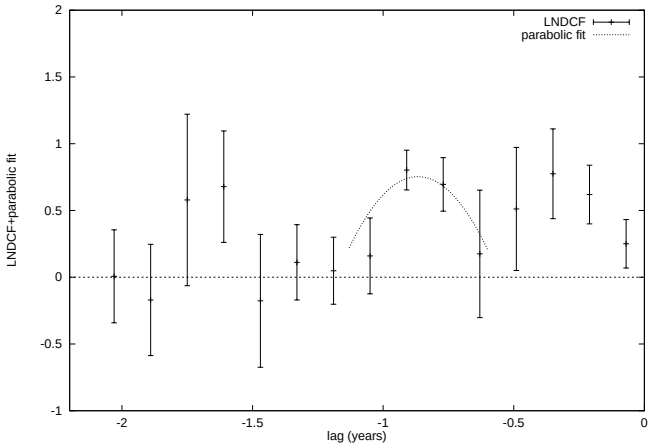

FIGURE 4.5: The LNDCF is evaluated with a 0.07 years bin semisize and the peak is fitted with a parabolic law. The result is a time delay $\Delta t_{B-A} = -0.87$ years (-0.91 years without the fit). A secondary peak appears at -0.35 years, although with larger error bars. This peak was the feature that "confused" the dispersion spectra.

The continuous lines are the noise levels. The $\alpha = 0.14$ years semisize shows a peak at -0.85 years, whereas with the $\alpha = 0.21$ years semisize the peak is at -0.80 years.

Now we need a good reason for preferring one over the other bin size. This reason could be the signal-to-noise ratio of the peak: in the first case $\alpha = 0.14$ years, $S/N = 3.9$, and in the second $\alpha = 0.21$ yrs, $S/N = 3.8$. Clearly, the difference of these two values is not high enough to conclude that one of them is the best.

In spite of the insignificant difference in this case, we notice that the signal-to-noise ratio is an important aspect and it is here where we justify the need for using 'clean' data sets, i.e. border effects and gaps corrected. In Fig. 4.7 we plot the CEDCF for the original dataset (without any correction): the peak is located at -0.90 years, but the signal-to-noise is 1.95!. The main peak loses signal recovered by a secondary competing peak around lag zero and by the wings. Although this secondary peak is very unlikely to be the delay peak, Fig. 4.7 cannot solve this ambiguity, which demonstrates that border effects can be dramatic in some cases. In Sect. 4.3.4 we will discuss the criteria to select a particular bin size.

4.3.3.5 Continously evaluated bins and locally normalized discrete correlation function: overlapping bins in the LNDCF

To our knowledge, this technique has not been applied before, but it seems a natural step as a combination of the two former techniques (i.e., the LNDCF and the CEDCF). From the one side, we use Eq. (4.7) for computing the DCF, i.e., it is a locally normalized discrete correlation function. From the other side, we use the idea of overlapping bins described in Sect. 4.3.3.4. Thus, the final result is a 'continuously evaluated bins and locally normalized discrete correlation function' (CELNDCF). Again, we fix the distances between the bins and also their width. The result will be a function similar in shape to the LNDCF in Fig. 4.5 but with more points evaluated.

The method was applied for three different values of the bin semisize: $\alpha = 0.07$, 0.14 and 0.21 years. The first value is not a good choice, it gives relatively large errorbars for the points of the

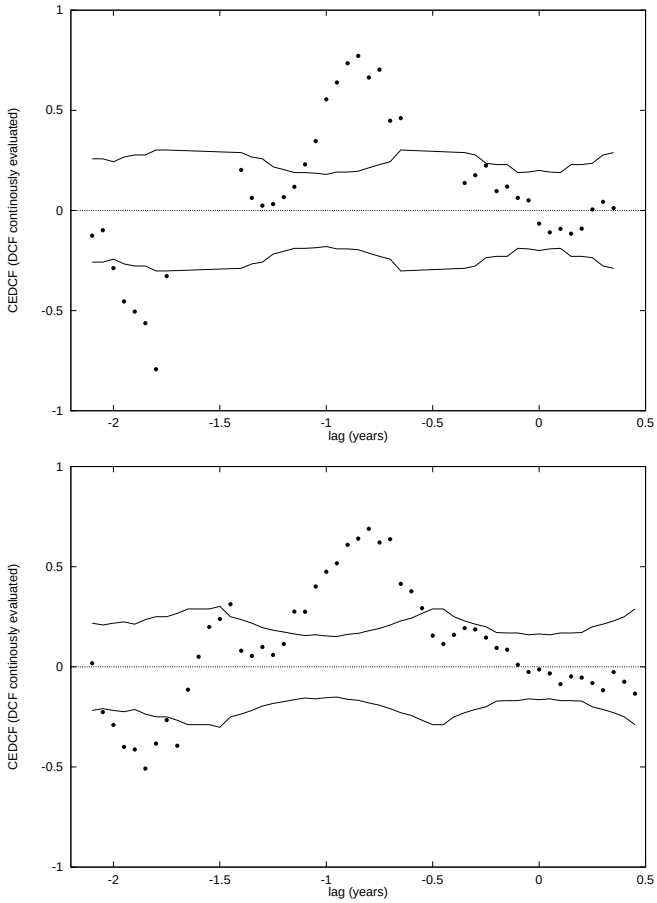

FIGURE 4.6: The CEDCF is a DCF which is evaluated with overlapping bins. *Top panel*: using a bin semisize of $\alpha = 0.14$ years we obtain a peak at -0.85 years with a good signal-to-noise ratio equal to 3.9. *Bottom panel*: with a bin semisize equal to $\alpha = 0.21$ years, the peak is at -0.80 years. Although it seems that the function is better defined, i.e. with more points, the signal-to-noise ratio at the peak is 3.8. The continuous lines are the noise levels in both panels (cf. also Fig. 4.7).

CELNDCF, since the number of points per bin is low. Selecting the last two values, i.e. $\alpha = 0.14$ yrs. and $\alpha = 0.21$ yrs., we obtain Fig. 4.8. The first one gives a time delay of $\Delta t_{B-A} = -0.85$ years and the second one a value of $\Delta t_{B-A} = -0.75$ years. This second result is very close to the first estimation in W98. The reader can easily compare the results with and without overlapping bins (Fig. 4.8 and Fig. 4.5, respectively) and clearly see the advantages of this second procedure. Nevertheless, there is a relatively large difference between selecting one or the other value of the bin semisize (i.e. $\alpha = 0.14$ years vs. $\alpha = 0.21$ years). This means the technique is also very sensitive to the poor sampling. The next and final technique will clarify which is the best bin size selection.

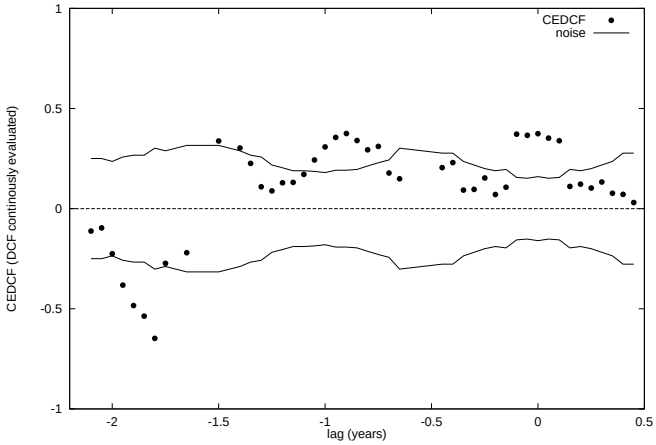

FIGURE 4.7: Not eliminating borders can be crucial in DCF-based methods. Here the CEDCF has been computed with the original data set, i.e. using all points. There is a peak at -0.90 years, with a signal-to-noise value of 1.95. Other points around a secondary peak located at time zero describe another feature. The great amount of information lost in the main peak is obvious.

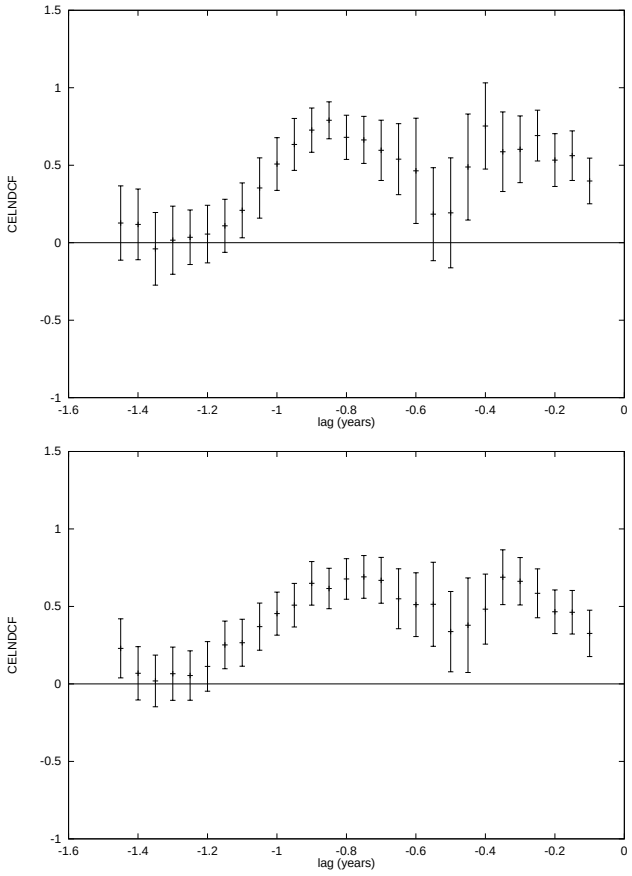

FIGURE 4.8: *Top panel*: The CELNDCF is evaluated with $\alpha = 0.14$ years bin semisize and a distance between bin centers of 0.05 years. The result is a time delay $\Delta t_{B-A} = -0.85$ years. *Bottom panel*: The CELNDCF computed with $\alpha = 0.21$ years bin semisize. The distances between the bin centers is also 0.05 years. The peak is obtained at -0.75 years where it is assumed to be the time delay.

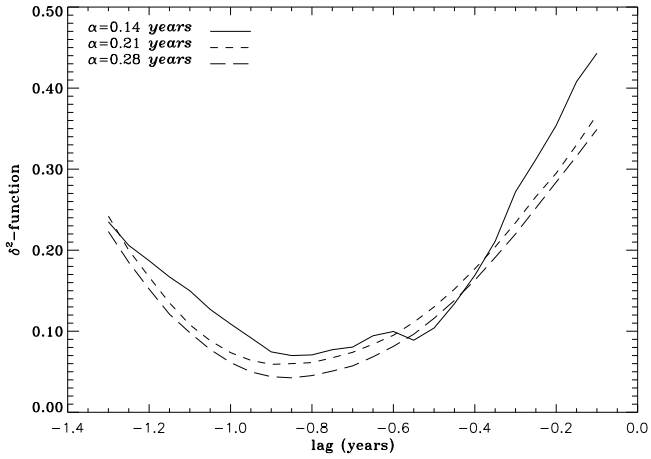

FIGURE 4.9: The δ^2 function for three different values of the bin semisize α: solid line 0.14 years, short dashed 0.21 years and long dashed 0.28 years. Since $\delta^2_{\rm min}(\alpha = 0.28) < \delta^2_{\rm min}(\alpha = 0.21) < \delta^2_{\rm min}(\alpha = 0.14)$, the minimum value in δ^2 for $\alpha = 0.14$ years is unlikely to be an artifact (see text for more details).

4.3.4 The δ^2 technique: a comparison between the cross correlation function and the autocorrelation function

The following method, called δ^2, was introduced by Goicoechea et al. (1998b) and Serra-Ricart et al. (1999). Its expression is

$$\delta^2(\theta) = \frac{1}{N}\sum_{i=1}^{N} S_i[DCC(\tau_i) - DAC(\tau_i - \theta)]^2 \tag{4.8}$$

where $S_i = 1$ if $DCC(\tau_i)$ and $DAC(\tau_i - \theta)$ are both defined and $S_i = 0$ otherwise. The DCC is the continuously evaluated discrete correlation function, and the DAC is the discrete autocorrelation function. The method uses the DCC and the DAC of one of the components, and tries to get the best match between them by minimizing its difference. If one has two equal signals, these functions must be identical. The δ^2 function reaches its minimum $\theta_0 = \Delta t_{B-A}$ at the time delay. We note that the match of both functions is not a match between their peaks, but rather a global match.

We have selected component B for computing the DAC, because component A has more variability (presumably due to microlensing). We compute δ^2 for different values of the bin semisize. Adopting a bin semisize $\alpha = 0.14$, the function shows some features and reaches its minimum at -0.85 years (see Fig. 4.9, solid line). Now we compute δ^2 for a bin semisize $\alpha = 0.21$ years, which yields a minimum at -0.90 years (Fig. 4.9, long dashed line). The question now is: are we loosing resolution using this last bin semisize ($\alpha = 0.21$ years) or is this minimum at -0.90 years a better estimate? The reader could argue that $\delta^2_{\rm min}(\alpha = 0.21) < \delta^2_{\rm min}(\alpha = 0.14)$, so that the agreement between DAC and DCC is better for $\alpha = 0.21$. This is not so. Consider a bin semisize $\alpha = 0.28$ years (Fig. 4.9, short dashed line): We obtain a minimum at -0.85 years while again $\delta^2_{\rm min}(\alpha = 0.28) < \delta^2_{\rm min}(\alpha = 0.21)$. This indicates that the minimum located at -0.85 years with $\alpha = 0.14$ years was not an artifact of some noise features, but that these features are real. To clarify this, Fig. 4.10 shows the comparison between the DCC and DAC function for the three different

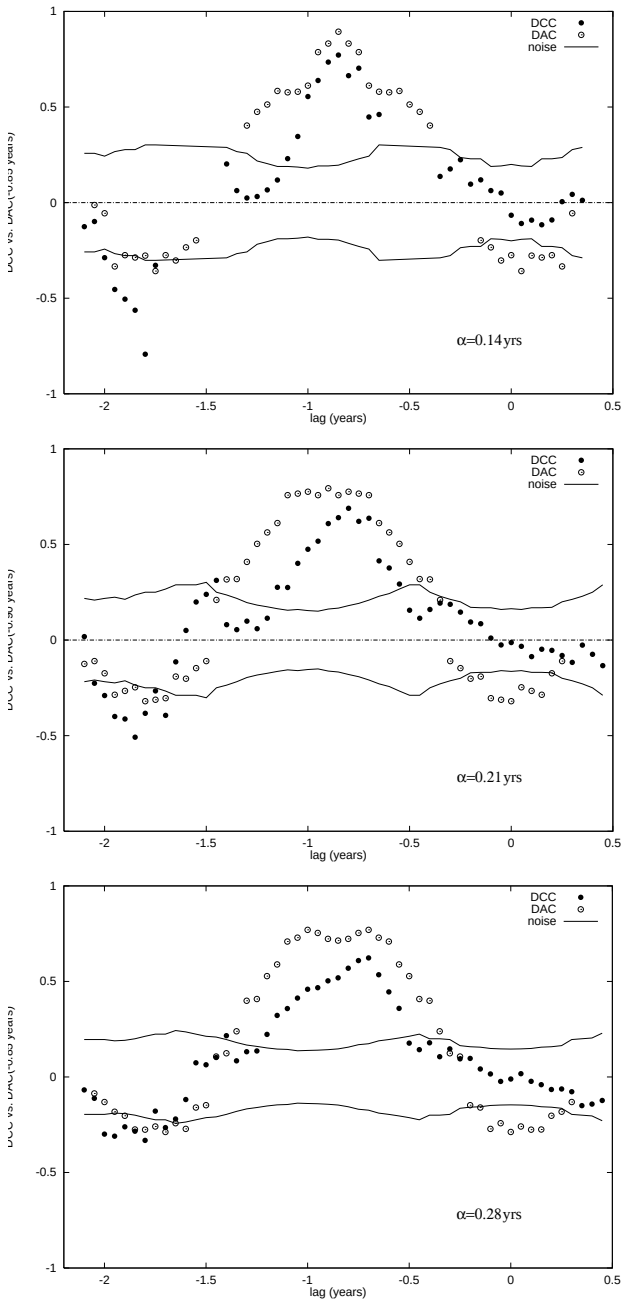

FIGURE 4.10: *Upper panel*: both DCC (filled circles) and DAC (open circles) are plotted. The bin semisize is $\alpha = 0.14$ years and the DAC has been shifted by -0.85 years, which is the value for the time delay obtained with the δ^2 technique. *Middle panel*: the bin semisize is now $\alpha = 0.21$ years. DAC (open circles) has now been shifted by -0.90 years, which is the value obtained with the δ^2 technique. The bin semisize is now $\alpha = 0.21$ years. *Bottom panel*: for $\alpha = 0.28$, $\delta^2_{min} = -0.85$ again, so the DCC (filled circles) is shifted by that value. In the three subfigures the solid lines indicate the noise levels. The best agreement between DCC and DAC is for $\alpha = 0.14$ years (upper panel).

values of the bin semisize α (0.14, 0.21 and 0.28 years in the upper panel, middle panel and bottom panel, respectively). Accordingly, we consider the $\alpha = 0.14$ years the best bin semisize and we analyse δ^2 for that value.

In order to better study the features in the δ^2 function, we plot it normalized to its minimum in Fig. 4.11. This figure is quite illustrative: (i) The minimum is reached at -0.85 years. (ii) The trend of the main feature is asymmetric, with a relatively slow rise at the right hand side, favoring values in the range $[-0.9, -0.7]$, including most of the estimates from other techniques or binning. (iii) A 'secondary minimum' is present at -0.55 years. This may be due to the fact remarked already by W98: for such a lag, the observing periods of one component coincides with the seasonal gaps in the lightcurve of the other. (iv) The feature in the range $[-0.3, -0.4]$ is not present, meaning that this value is very unlikely (this was the value that appeared with dispersion spectra, LNDCF and CELNDCF methods).

To obtain an estimate for the formal error of this method, we used 1000 Monte Carlo simulations. For each simulation we did the following: for each epoch t_i we associated a value in magnitudes $x_i + \Delta x_i$, where x_i is the observed value and Δx_i is a Gaussian random variable with zero mean and variance equal to the estimated measurement error. The histogram is presented in Fig. 4.12. The simulations reproduce all the information contained in the δ^2 function in Fig. 4.11: the most probable value is -0.85 years (599 simulations); it also appears in a number of simulations around -0.90 years (57 simulations), -0.80 years (285 simulations), -0.75 years (5 simulations) and around -0.70 years (20 simulations). A few simulations (36) are also located around -0.55 years, which is very close to the one considered in W98 as spurious (a value around half a year). In any

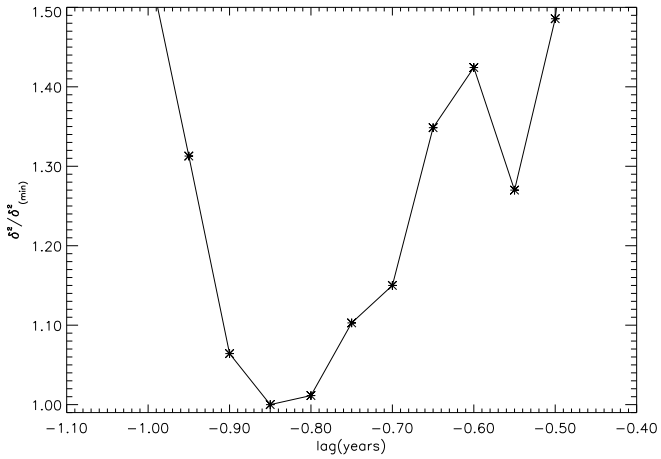

FIGURE 4.11: The minimum of the δ^2 function at -0.85 years gives the time delay between the components. We have normalized it with its minimum. A secondary peak is present around -0.55 years, a value also considered by W98. The trend of the main feature is asymmetric, favoring values for the time delay in the range [-0.9, -0.7], including several best estimates of the time delay from other techniques or binning.

case, the simulations are in very good agreement with the information contained in the δ^2 function. As 95% of the simulations claim a time delay in the interval $[-0.90, -0.80]$, we can adopt a value of $\Delta t_{B-A} = (-0.85 \pm 0.05)$ years for the time delay of this system, with a 2σ confidence level (formal or internal error). Fig. 4.13 shows the lightcurves with component A shifted by the adopted time delay.

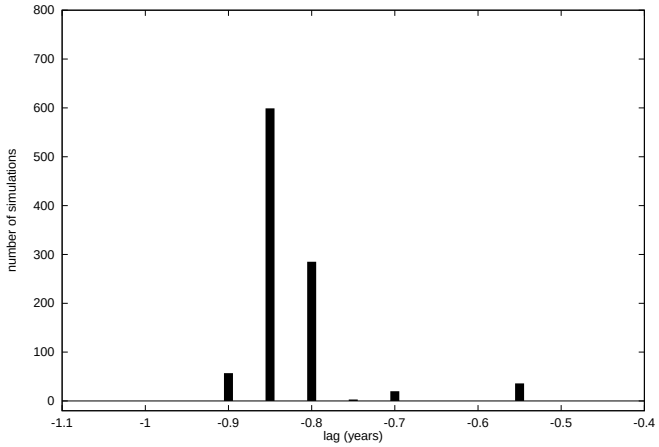

FIGURE 4.12: Histogram of time delays obtained in 1000 Monte Carlo simulations, using the δ^2 technique.

4.4 Discussion

4.4.1 Comparison of the different techniques

From our tour through the different techniques we can learn several useful things. First of all, when only one technique is selected for deriving a time delay between two signals, it is important to check the internal consistency of the method and its behaviour with a given data set. We have demonstrated in Sect. 4.3.2 that dispersion spectra does not pass this test at least in this case (see Fig. 4.3). We have then applied and discussed the discrete correlation function and several of its modifications. The standard DCF (Fig. 4.4) had problems to properly define the peak in the case of very poorly sampled lightcurves; although a fit was proposed to solve this problem, there were only two points above the noise level in the best case and the fit was not very plausible. The LNDCF (Fig. 4.5), based on locally normalized bins, had a similar behaviour and although the error bars of each point are smaller, the peak is not well defined either. The CEDCF (Fig. 4.6) and the CELNDCF (Fig. 4.8) worked better under these circumstances, but we found the problem of selecting the bin size; in the case of the CEDCF the difference between the two selected bin sizes was smaller than in the case of the CELNDCF. Finally applying the δ^2 technique, we found a good reason for selecting one bin size: the match between the DAC and the DCC. The resulting estimate and its uncertainty include, as a 'byproduct', the results of the rest of the techniques for the same bin size (except the dispersion spectra method which was not self-consistent). This fact is not the same as applying all the techniques to obtain an uncertainty. This frequently appears in the time delay determination literature, although it is not at all clear which was the weight of each technique when computing the final result. We note that for consistency we should apply a correction to the original data set with the final adopted time delay of -0.85 years. Due to the (very) sparse sampling of our data set, this correction gives a reduced data set identical to the previous 'clean' data set obtained with a correction of -0.73 years, so we do not need to repeat the whole process. The procedure is self-consistent.

It is important to notice that we have not meant to establish any general hierarchy between all these techniques. The hierarchy is valid in our particular case study. Nevertheless, the idea, not

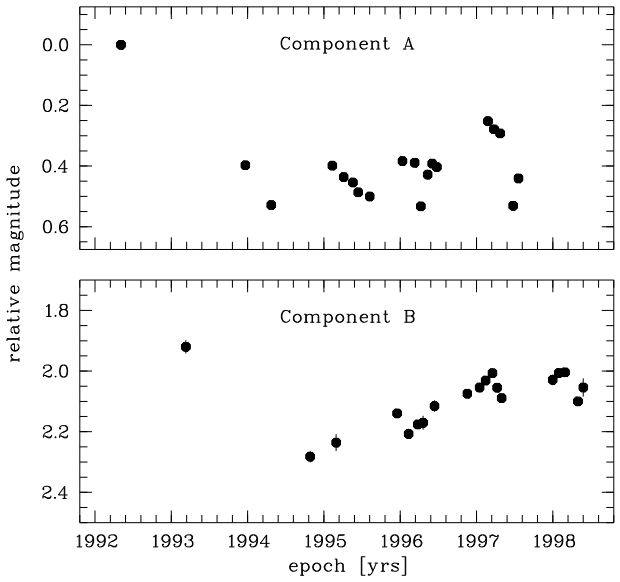

FIGURE 4.13: The original dataset with the component A shifted by the new adopted time delay, $\Delta t_{B-A} = -0.85$ years.

new, of correcting border effects in the signals with first estimations has been proved to be a good procedure in DCF based techniques.

4.4.2 Investigation of secondary minima/maxima

In some of the techniques we have discussed and applied here for the data of HE 1104−1805, there appear secondary peaks/dips located at different values for the time lags (see Fig. 4.5, Fig. 4.8 and Fig. 4.11). Here we investigate two obvious effects that might cause such behaviour, namely microlensing and sampling. We do this only as a case study for the δ^2 technique, but assume that our conclusions can be generalized to the other methods as well.

4.4.2.1 Microlensing

Microlensing affects the two quasar lightcurves differently. That means that the two lightcurves will not be identical copies of each other (modulo offsets in magnitude and time), but there can be minor or major deviations between them. On the other hand, experience from other multiple quasar systems tells us that microlensing cannot dominate the variability, because otherwise there would be no way to determine a time delay at all. In any case, microlensing is a possible source of 'noise' with respect to the determination of the time delay.

A complete analysis of microlensing on this system is beyond the scope of this Section, and will be addressed in a future work. Here we present a simple, but illustrative, approach to the way microlensing can affect the determination of the time delay, and in particular its effect on the δ^2 technique. An 'extreme' view of microlensing was investigated by Falco et al. (1991), who showed for the Q0957+561 system that it is very unlikely that microlensing can mimic 'parallel' intrinsic fluctuations causing completely wrong values for the time delay correlations. But

strong microlensing clearly affects the features of the cross-correlation function (Goicoechea et al. 1998a). Depending on the exact amplitude and shape of the microlensing event, the main and secondary peaks of this function can be distorted, possibly inducing wrong interpretations.

In order to study this effect here, we do the following: we consider the lightcurve of component B (assumed to reflect only intrinsic quasar variability) and a copy of it, shifted by 0.85 years, which we shall call B′. Obviously, any technique will give a time delay value of $\Delta t_{B-B'} = -0.85$ years between B and B′. In the case of the δ^2 technique, a very sharp minimum is located at this lag. Now we introduce artificial 'microlensing' as a kind of Gaussian random process with zero mean and a certain standard deviation $\sigma_{\rm ML}$ to the lightcurve B′. We consider three cases: $\sigma_{\rm ML} = 0.050$ mag, 0.075 mag and 0.100 mag. Although microlensing is in general obviously not a random process (it depends a bit on the sampling), we use this simple approximation in order to study whether and how secondary peaks can appear in time delay determinations. The resulting δ^2-functions can be seen in Fig. 4.14, which can be compared to Fig. 4.11. It is very obvious that for the 'smallest' microlensing contribution ($\sigma_{\rm ML} = 0.050$ mag, thin solid line) the minimum of the δ^2 normalized function is still a very sharp feature. For the next case ($\sigma_{\rm ML} = 0.075$ mag, dashed line) the δ^2 function gets wider and 'noisier', and for the strongest influence of microlensing ($\sigma_{\rm ML} = 0.1$ mag, thick solid line) a secondary features appears. But in no case the distortion prohibits a clear and correct time delay determination, the primary minimum is still clearly identifiable (microlensing fluctuations during the period covered by our monitoring are of the order of 0.07 mag rms; Wisotzki, 2001, priv.comm.).

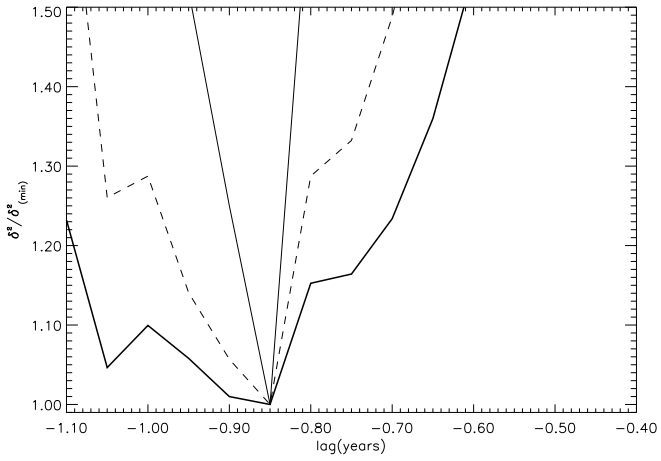

FIGURE 4.14: We calculate the time delay between the lightcurves B and B′ with the δ^2 technique. B′ is a copy of B, shifted 0.85 years and with a gaussian random process added in order to simulate microlensing. *Thin solid line*: the gaussian random process has a standard deviation of 0.05 mag. There are no secondary peaks. *Dashed line*: If the standard deviation of the gaussian random process is 0.075 mag., some secondary features appear. *Thick solid line*: the δ^2 normalized function is much more distorted, but the technique can calculate the shifted value of 0.85 years.

To make sure that this is not a chance observational effect of this particular selected lag, we repeat this exercise for an assumed shift of -0.5 years between the observed lightcurve and its shifted copy, plus added 'artificial microlensing' with $\sigma_{\rm ML} = 0.1$ mag. Again, the correct value is clearly recovered in all realisations. This is particularly convincing because a lag of 0.5 years

is the 'worst case scenario' with minimal overlap between the two lightcurves. To summarize, moderate microlensing can be a cause of distortions of the time delay determination function, but it is unlikely that microlensing dominates it completely in this dataset.

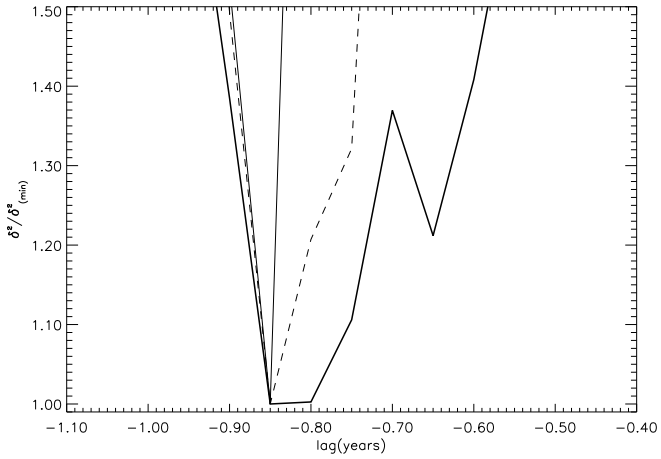

FIGURE 4.15: We analyse the sampling effect in the δ^2 technique. We use lightcurves B and B′, B′ being a copy of B shifted 0.85 years and removing a number of points. *Thin solid line*: we remove two random points in the component B′. *Dashed line*: when removing four random points, there appears secondary structure in the δ^2 function. *Thick solid line*: if three adjacent points are removed, the δ^2 normalized function is very similar to the one computed with lightcurves A and B (see Fig. 4.11).

4.4.2.2 Sampling

In order to study the effect of sampling on the shape of the δ^2 function, we proceed as follows: again, we consider the lightcurve of component B and an identical copy of it shifted by 0.85 years, lightcurve B′. Now we remove some points from lightcurve B′. Resulting δ^2 functions are shown in Fig. 4.15 for three cases. The thin solid line is a case in which two random points have been removed from B. The minimum of the δ^2 normalized function is still well defined, with no secondary structure. For the dashed curve in Fig. 4.15, four random points were taken away. The shape of the function is distorted and a secondary dip appears. For the thick solid line, three adjacent hand-picked points (epochs 1997.12, 1997.21, 1997.27) were excluded. Surprisingly, although all the remaining data points have identical spacing in B′ as in B, the removal of the three points causes a secondary minimum in the δ^2 function, which is very similar to the one obtained for the real data, using the observed lightcurves A and B (Fig. 4.11). This case is very illustrative: it suggests that the sampling alone could be responsible for the secondary minimum found in the real data (Fig. 4.11). This effect certainly deserves more study. From this preliminary analysis it appears that better and denser sampling of quasar lightcurves could be much more important for time delay studies than fewer data points with higher photometric precision.

As above, we also want to check whether the particular value of the time lag plays an important role, and we again repeat the simulation exercise with an assumed lag of -0.5 years, and 4 randomly selected points removed. The result is again $\Delta t_{B-B'} = -0.5$ years, recovering the assumed lag in all cases.

4.4.2.3 Summary of microlensing/sampling effects

Summarizing, we can state that both microlensing and sampling differences affect the shape of the time delay determination function. However, moderate microlensing will have only small effects on these curves, whereas moderate (and unavoidable!) differences in the sampling for the two lightcurves can easily introduce effects like secondary minima. The primary minimum of the δ^2 method in all cases considered was still clearly representing the actual value of the time delay. Applied to HE 1104−1805, this means that most likely microlensing does not affect much the time delay determination, the features in the time delay determination function can be easily explained by the sampling differences, and the primary minimum appears to be a good representation of the real time delay.

4.4.3 Implications for H_0 determination

If one wants to use the time delay to estimate the Hubble parameter H_0, one needs to know the geometry and mass distribution of the system. Accurate astrometry is available from HST images presented by Lehar et al. (2000). There are also several models for the lens in the literature. In W98, two models are described: a singular isothermal sphere with external shear and a singular isothermal ellipsoid without external shear. The first model is similar to Remy et al. (1998) and Lehar et al. (2000). Courbin et al. (2000) also present two models: a singular ellipsoid without external shear and a singular isothermal ellipsoid plus an extended component representing a galaxy cluster centered on the lens galaxy.

The redshift of the lens in this system has been establish by Lidman et al. (2000) to be $z_d = 0.729$. Note that HE 1104−1805 is somehow atypical, in the sense that the brightest component is closer to the lens galaxy. We use the most recents models by the CASTLES group (Lehár et al. 2000), described by a singular isothermal ellipsoid (SIE) and a constant mass-to-light ratio plus shear model ($M/L + \gamma$). The derived value for the Hubble constant using the first model (SIE) is $H_0 = (48 \pm 4)\ \mathrm{km\ s^{-1}\ Mpc^{-1}}$ with 2σ confidence level. A ($M/L + \gamma$) model gives $H_0 = (62 \pm 4)\ \mathrm{km\ s^{-1}\ Mpc^{-1}}$ (2σ), both for $\Omega_0 = 1$. The formal uncertainty in these values are very low, due to the low formal uncertainties both in the time delay estimation and in the models. Nevertheless, the mass distribution is not well constrained, since a sequence of models can fit the images positions (Zhao & Pronk 2000). We note that other models in Lehar et al. (2000) will give very different results for H_0, but we did not use them because no error estimate was reported for them. Moreover, the angular separation is big enough to expect an additional contribution to the potential from a group or cluster of galaxies (Muñoz 2001, priv. comm.).

4.5 Conclusions

We have shown that the existing data allow us to constrain the time delay of HE 1104−1805 with high confidence between 0.8 and 0.9 years, slightly higher than the one available previous estimate. We have demonstrated that the six different techniques employed in this study were not equally suited for the available dataset. In fact, this case study has demonstrated that a very careful analysis of each technique is needed when applying it to a certain set of observations. Such an analysis becomes even more important in the case of poorly sampled lightcurves. In this

sense, the δ^2 technique showed the best behaviour against the poor sampling: unless the lack of information due to sampling is so severe that it prevents the determination of well defined discrete autocorrelation (DAC) and cross-correlation (DCC) functions, the minimum of the δ^2 function will be a robust estimator for the time delay.

Our proposed time delay estimate yields a value of the Hubble parameter which now depends mostly on the uncertainties of the mass model. The degeneracies inherent to a simple 2-image lens system such as HE 1104−1805 currently preclude to derive very tight limits on H_0. We note, however, that there are prospects to improve the constraints on the model e.g. by using the lensed arclet features visible from the QSO host galaxy. Even now, there seems to be a remarkable trend in favour of a relatively low value of H_0, consistent with other recent lensing-based estimates (Schechter 2000).

Soon after this work was finished, Pelt et al. (2002) argued that the uncertainties in our time delay estimation were underestimated, probably due to the poorly sampled lightcurves. They forgot that this was exactly our exercise: extract information when sampling is far from optimal. They also argued that our notion of consistency regarding dispersion minimization method was inappropiate. Nevertheless, they did not explain why the inconsistency we found in their method does not appear in all the other techniques.

Recently, two teams have presented new photometries on HE 1104−1805. Schechter et al. (2003) showed three years of photometry obtained with the OGLE 1.3m telescope. Although the sampling was three points per month, they found such a strong microlensing signal that they were unable to estimate a time delay for they system. Instead, they analysed a variety of possible causes for the microlensing signal. They concluded that the most likely scenario was to consider multiple hotspots in the quasar accretion disk, an idea based on Gould & Miralda-Escudé (1997) and numerically simulated by Wyithe & Loeb (2002).

Ofek & Maoz (2003) observed HE 1104−1805 with the Wise Observatory 1m telescope. They combined their photometry with that by Schechter et al. (2003), covering a total observing period of five years. They measured a time delay of $\Delta t_{A-B} = -161^{+7,+34}_{-7,-11}$ days (1σ and 2σ errors). There are various problems in this new estimate of the time delay that will be discussed in a future work. We point them out here. The combination of the photometries is a very delicated issue. A little offset in it can induce wrong time delay estimates. Furthermore, they detect a high microlensing variability with a timescale of a month. But they do not show a detailed analysis of the influence of such a signal in the measured time delay nor in the error estimate. Obviously, microlensing is a source of noise when computing time delays that has to be carefully taken into account.

Chapter 5

Analysis of difference lightcurves: disentangling microlensing and noise in the double quasar Q0957+561⋆

Link. *After carrying out a monitoring campaign of a multiple image lensed quasar and correcting for the time delay between the images, one is able to do microlensing studies of the system. There are different ways of exploring the possible microlensing fluctuations in the difference lightcurves. One way is using Monte Carlo simulations. This kind of simulations can be very useful in disentangling microlensing and other possible sources of noise, which are quite easy to mix up.*

Abstract. From optical R band data of the double quasar Q0957+561A,B, we made two new difference light curves (about 330 days of overlap between the time-shifted light curve for the A image and the magnitude-shifted light curve for the B image). We observed noisy behaviours around the zero line and no short-timescale events (with a duration of months), where the term event refers to a prominent feature that may be due to microlensing or another source of variability. Only one event lasting two weeks and rising - 33 mmag was found. Measured constraints on the possible microlensing variability can be used to obtain information on the granularity of the dark matter in the main lensing galaxy and the size of the source. In addition, one can also test the ability of the observational noise to cause the rms averages and the local features of the difference signals. We focused on this last issue. The combined photometries were related to a process consisting of an intrinsic signal plus a Gaussian observational noise. The intrinsic signal has been assumed to be either a smooth function (polynomial) or a smooth function plus a stationary noise process or a correlated stationary process. Using these three pictures without microlensing, we derived some models totally consistent with the observations. We finally discussed the sensitivity of our telescope (at Teide Observatory) to several classes of microlensing variability.

⋆Chapter based on the refereed publication Gil-Merino et al., 2001, MNRAS, 322, 397

5.1 Introduction

5.1.1 Microlensing caused by the Milky Way and other galaxies

Dark matter dominates the outer mass of the Milky Way. In principle, the population of the Galactic dark halo may include astrophysical objects like black holes, brown dwarfs, white dwarfs or MACHOs (MAssive Compact Halo Objects) with stellar or substellar mass, as well as elementary particles (a smooth component). Today, from microlensing surveys, we have some information about the granular component (MACHOs). The absence of very short duration events – from a fraction of an hour to a few days – implies that the dark halo cannot be dominated by planetary objects – with masses $10^{-8}\ M_{\odot} \leq M_{\rm planet} \leq 10^{-3}\ M_{\odot}$. A joint analysis by the *EROS* and *MACHO* collaborations indicated that MACHOs in the mass range $10^{-7} M_{\odot} \leq M \leq 10^{-3} M_{\odot}$ make up less than 25% of the dark halo (Alcock et al. 1998). From a likelihood analysis, the *MACHO* collaboration concluded that a population of objects of mass $\sim 0.5\ M_{\odot}$ is consistent with their first two year of data. These MACHOs with stellar mass would have an important contribution to the total mass (Alcock et al. 1997; Gould 1997; Sutherland 1999; Mao 2000). However, very recent results by the *MACHO* team, based on approximately six years of observations, point to a relatively small mass fraction (Alcock et al. 2000). For a typical size halo, the maximum likelihood estimates suggest the existence of a Milky Way dark halo consisting of 20% MACHOs with mass of $\sim 0.6\ M_{\odot}$ (with a 95% confidence interval of 8%-50%). The *EROS* collaboration also agrees with this small contribution to the dark halo by $\sim 0.6\ M_{\odot}$ objects (Lasserre et al. 2000). Lasserre et al. (2000) derived strong upper limits on the abundance of MACHOs with different masses. For example, less than 10% of the dark halo resides in planetary objects. Moreover, they ruled out a standard spherical halo in which more than 40% of its mass is made of dark stars with $1\ M_{\odot}$. Finally, we remark that the Milky Way dark halo inferred from the maximum likelihood method (best standard fits by Alcock et al. 2000) is consistent with the *HST* (Hubble Space Telescope) detection of a halo white dwarf population (Ibata et al. 1999). A population of cool white dwarfs contributing 1/5 of the dark matter in the Milky Way could explain all new observational results, but this hypothesis presents some difficulties (e.g., Mao 2000; Alcock et al. 2000): e.g., if the MACHOs are white dwarfs, these stars will produce too much chemical enrichment in the halo (Freese et al. 2000); also the fraction of MACHOs is larger – the exact value depends on the adopted cosmology – than the baryon fraction expected from nucleosynthesis.

The information on the nature of galaxy dark haloes is still largely based on a local spiral galaxy (the Galaxy), and so, the study of other galaxies seems an interesting goal.

The Einstein Cross (Q2237+0305) is a z = 1.69 quasar lensed by a face-on barred Sb galaxy at z = 0.0394 (Huchra et al. 1985). The time delay between the four quasar images is expected to be less than a day (Rix et al. 1992; Wambsganss & Paczyński 1994), and so, one can directly separate intrinsic variability from microlensing signal. For this lens system, light rays of the 4 images pass through the bulge of the foreground galaxy and there is robust evidence that microlensing events occur (e.g., Irwin et al. 1989; Wozniak et al. 2000). The observed events are interpreted as a phenomenon caused by the granularity of the matter associated with the nearby spiral. For providing an interpretation of the *OGLE* Q2237+0305 microlensing light curve, Wyithe, Turner & Webster (2000a) used the contouring technique of Lewis et al. (1993) and Witt (1993) to put limits on the microlenses mass function, ruling out a significant contribution of Jupiter-mass compact objects to the mass distribution of the galactic bulge of the lensing galaxy (see Chapter 6 for more

details on this system).

B1600+434 is another interesting gravitational mirage lensed by an edge-on disk galaxy. Koopmans & de Bruyn (2000) measured the radio time delay between the two images of the system and derived a radio difference light curve which is in disagreement with zero. They investigated both scintillation and microlensing as possible causes of the non-intrinsic radio variability. If microlensing is the origin of the 'anomalous' difference light curve, then it could indicate the presence of a lens galaxy dark halo filled with MACHOs of mass $\geq 0.5 M_{\odot}$.

5.1.2 Microlensing in the first gravitational lens system (Q0957+561)

A third well-known microlensed quasar is the z = 1.41 double system Q0957+561A,B (Walsh et al. 1979). The main lens galaxy is an elliptical galaxy (cD) at z = 0.36 (Stockton 1980). While the light associated with the image B crosses an internal region of the lens galaxy, the light path associated with the component A is $\approx$ 5 arcsec away from the centre of the galaxy. The cD galaxy is close to the centre of a galaxy cluster, and consequently, the normalized surface mass densities κ_A and κ_B are the projected mass densities of the lensing galaxy plus cluster along the line of sight, normalized by the critical surface mass density. Pelt et al. (1998) used the values κ_A = 0.22 and κ_B = 1.24, which originate from an extended galaxy halo consisting of the elliptical galaxy halo and additional matter related to the cluster. It is possible that a considerable part of the extended halo mass does consist of a dark component, although an estimate of the stellar contribution (luminous stars) to κ_A and κ_B is not so easy as in the Milky Way. For the image B, if the fraction of mass in granular form κ_{BG} is dominated by normal stars and dark stars (i.e., MACHOs) similar to the objects that have been discovered in the Milky Way (Alcock et al. 2000), and simultaneously, the main part of the halo mass is due to a smooth component ($\kappa_{BG} << \kappa_B$, $\kappa_{BG} << 1$) and the source quasar is small, then we must expect some long-timescale microlensing event caused by one star (luminous or dark) crossing the path of this image. In the case of small source/one star approximation, the timescale of an Einstein radius crossing will be t_o(years) $\approx 17 \sqrt{M(M_{\odot})}[600/v_t(km \cdot s^{-1})]$, where v_t is the effective transverse velocity. The magnification of the B component has a typical duration from months to several years – depending on the exact values of the source size and the effective transverse velocity – for a 0.5-1 $M_{\odot}$ star. When κ_{BG} is high ($\kappa_{BG} \sim 1$) and/or the source is large, several stars at a time must be considered and the model by Chang & Refsdal (1984) is not suitable. The small source/one star model by Chang & Refsdal (1984) was generalized in the case of a small source and a large optical depth (Paczyński 1986a) and the case of an extended source and an arbitrary optical depth (Kayser, Refsdal & Stabell 1986; Schneider & Weiss 1987; Wambsganss 1990). Therefore, the formalisms by Chang & Refsdal (1984), Paczyński (1986a) and Wambsganss (1990) as well as new analytical approximations seem useful tools for a detailed analysis of the optical microlensing history of Q0957+561. A long-timescale microlensing signal was unambiguously observed from 1981 to 1999; see Pelt et al. (1998), Press & Rybicki (1998), Serra-Ricart et al. (1999, subsequently SR99). In this Chapter, we concentrate on the rapid fluctuations.

In the past, using a record of brightness as a function of time including photometric data (in the R band) up to 1995 and assuming a time delay of 404 days, Schild (1996, hereafter S96) analyzed the possible existence of short-timescale microlensing (rapid external variability on a timescale of months) and very rapid microlensing events (with duration of $\leq$ 3 weeks) in the

double Q0957+561A,B. He found numerous events with quarter-year and very short timescales (a few days). S96 also claimed that the slower component (events with a width of 90 days) can be interpreted as the imprint of an important population of microlenses with planetary mass of $\sim 10^{-5} M_{\odot}$. Assuming an improved delay value of 417 days, Goicoechea et al. (1998, subsequently G98) showed a difference light curve corresponding to the 1995/1996 seasons in Schild's dataset. G98 obtained fluctuations which could be associated with microlensing events, in fact, those results are in agreement with the existence of strong microlensing: the fluctuations in the difference light curve are clearly inconsistent with zero and similar to the fluctuations in the quasar signal (in amplitude and timescale). New work by Schild and collaborators pointed in the same direction: adopting a time delay of 416.3 days, Pelt et al. (1998) found that Schild's photometry shows evidence in favour of the presence of short-timescale microlensing; Schild (1999) made a wavelet exploration of the Q0957+561 brightness record, and reported that the rapid brightness fluctuations observed in the A and B quasar images (whose origin may be some kind of microlensing) are not dominated by observational noise; and Colley & Schild (1999), from a new reduction of 'old' photometric data – subtracting out the lens galaxy's light according to the *HST* luminosity profile and removing cross talk light from the A and B image apertures – , derived a structure function for variations in the R-band from lags of hours to years, a time delay of 417.4 days and a microlensing candidate on a timescale less than a day, which could imply planetary MACHOs in the lens galaxy halo. So, from the photometry taken at Whipple Observatory 1.2 m telescope by Schild, one obtains two important conclusions. First, there is evidence in favor of the existence of a short-timescale microlensing signal. Second, this rapid signal seems to support the presence of MACHOs (in the halo of the cD galaxy) having a very small mass. However we note that Gould & Miralda-Escudé (1997) have introduced an alternative explanation to the possible rapid microlensing in the double Q0957+561A,B, which is related to hot spots or other moving structures in the accretion disk in the quasar, and so, planetary objects are not involved.

Q0957+561A,B was photometrically monitored at Apache Point Observatory (Kundić et al. 1995, 1997) in the g and r bands, during the 1995 and 1996 seasons. Schmidt & Wambsganss (1998, hereafter SW98) analyzed this photometry and searched for a microlensing signature. Considering the photometric data in the g band and a delay of 417 days, SW98 produced a difference light curve covering $\approx$ 160 days and concluded that it is consistent with zero. There is no variation in the difference light curve with an amplitude in excess of $\pm$ 0.05 mag and the total magnitude variation of a hypothetical microlensing signal is assumed to be less than 0.05 mag (see the dashed lines in Fig. 1 in SW98). They employed this last upper limit to obtain interesting information on the parameter pair MACHO-mass/quasar-size. The lack of observed fluctuations rules out a population of MACHOs with $M \leq 10^{-3}\ M_{\odot}$ for a quasar size of 10^{14} cm (25%-100% of the matter in compact dark objects). However, other possible scenarios (e.g., a small source and a halo consisting of MACHOs with $M \geq 10^{-2}\ M_{\odot}$, a source size of 10^{15} cm and a halo with compact dark objects of mass $\leq 10^{-3}\ M_{\odot}$, etc.) cannot be ruled out from the bound on the microlensing variability in the 160 days difference light curve. In short, SW98 have not found reliable evidence for the presence of rapid microlensing events.

The gravitational lens system Q0957+561 was also monitored with the IAC-80 telescope at Teide Observatory, from the beginning of 1996 February to 1998 July (see SR99). We re-reduced the first 3 seasons (1996-1998) of Q0957+561 observations in the R band, made the difference light curves for 1996/1997 seasons and 1997/1998 seasons and studied the origin of the deviation

between the light curves of the two images. All the results are presented as follows: in Sect. 5.2 we present the difference light curves and report on new constraints on microlensing variability. In Sect. 5.3 we suggest different models that explain the difference signal. In Sect. 5.4 we discuss the sensitivity of the telescope to different microlensing 'peaks'. In Sect. 5.5, we summarize our results.

5.2 Q0957+561 difference lightcurves in the R band

We have been monitoring Q0957+561 from February 1996 with the 82 cm IAC-80 telescope (at Teide Observatory, Instituto de Astrofisica de Canarias, Spain) and have obtained a large R band dataset. The contribution to the solution of the old controversy regarding the value of the time delay ($\approx$ 400-440 days or $>$ 500 days ?) was the first success of the monitoring program (Oscoz et al. 1996; see also Kundić et al. 1995, 1997; Oscoz et al. 1997).

In order to give refined measurements of both time delay and optical microlensing, we have introduced some improvements with respect to the original aperture photometry (see Oscoz et al. 1996). Reduction of the images A and B is complicated by the presence of cross contamination and contamination from light of the main lensing galaxy. The two kinds of contamination depend on the seeing, and it is not clear what is the optimal way of obtaining the best photometric accuracy. Here each available night was reduced by fitting a profile to the images, which is consistent with the point spread function of comparison stars. This new method of reduction and the photometry from 1996 to 1998 (the first 3 seasons) are detailed in SR99. A table including all data is available at `http://www.iac.es/project/quasar/lens7.html`.

In the Q0957+561 quasar, a time delay of $\approx$ 420 days is strongly supported (e.g., G98). Using the first 3 seasons of data, the time delay estimates (in SR99) are of (425$\pm$4) days (from the δ^2-test, which is based on discrete correlation functions) and (426$\pm$12) days (from dispersion spectra). A comparison between the discrete cross-correlation function and the discrete autocorrelation function, indicates that a time delay of $\leq$ 417 days is in disagreement with the photometry (see Fig. 16 in SR99), while a delay of about 425 days is favoured. Thus, we adopted a time delay of 425 days.

We concentrate now on the difference lightcurves. In order to estimate the difference lightcurve (DLC hereafter) for the 1996/1997 and the 1997/1998 seasons, we used 30 observations of image A corresponding to the 1996 season ($A96$), 28 observations of image B corresponding to the 1997 season ($B97$), 44 photometric data of image A in the 1997 season dataset ($A97$) and 84 photometric data of image B in the 1998 season dataset ($B98$). There are about 100 days of overlap between the time-shifted (with time delay 425 days) lightcurve $A96$ and the lightcurve $B97$, and about 230 days of overlap between the time delay-corrected lightcurves $A97$ and $B98$. The main problem of the IAC-80 telescope (using the available observational time of 20-30 min/night) is related to the photometric errors. The mean errors in the initially selected datasets are approximately 19 mmag ($A96$), 24 mmag ($B97$), 28 mmag ($A97$) and 24 mmag ($B98$). For short-timescale and small amplitude microlensing studies, these errors are large and one must re-reduce the data (binning them for obtaining lower errors). Because of the possible rapid microlensing variability on one month timescale, the timescale of the bins should not be too large ($\leq$ 10 days); it should not be too small for having a sufficient number of data, and so, relatively small errors. The re-reduced photometry consists of 12, 11, 22 and 36 'observations' in four new (and final) datasets $A96$, $B97$, $A97$ and $B98$, respectively. For bins in $A96$, the timescales are less than 3 days and the mean error

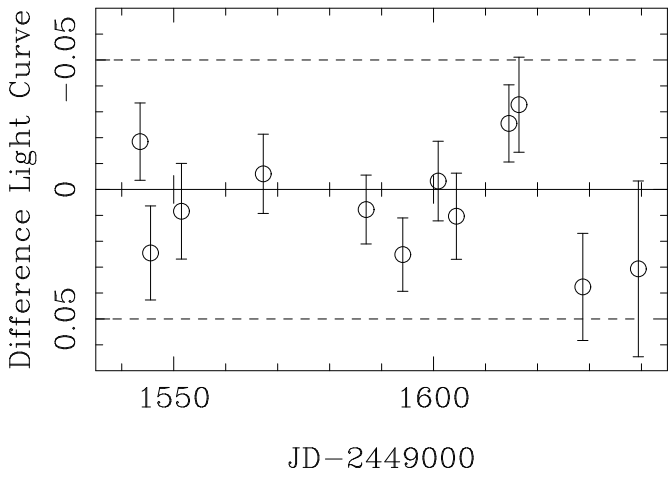

FIGURE 5.1: Difference lightcurve for 1996/1997 seasons – in the R band (magnitudes) –. We used bins with semi-size of 9 days and adopted a time delay of 425 days. The times associated with the circles are the dates in the time-delay shifted lightcurve $A96$ (see main text).

is of $\approx$ 12 mmag, for bins in $B97$, the timescales are $\leq$ 8 days and the mean uncertainty is of $\approx$ 16 mmag, for bins in $A97$, the timescales are also $\leq$ 8 days and the mean error is lowered to $\approx$ 20 mmag, and for bins in $B98$, the maximum timescale and the mean uncertainty are 6 days and 16 mmag, respectively. Therefore, making bins with a maximum timescale of $\approx$ 1 week (the mean timescale is of $\approx$ 2 days), the mean errors are lowered by 7-8 mmag.

As we have seen in the previous paragraph, the brightness record for the A image ($A96$ or $A97$) is measured only at a set of discrete times t_i (i = 1,...,N) and the lightcurve for the B image ($B97$ or $B98$) is also determined at discrete times t_j (j = 1,...,M). Since the observational lightcurves are irregularly sampled signals, to obtain the DLC ($A96/B97$ or $A97/B98$), we can use different methodologies, for example, the interpolation suggested by SW98 or the binning that appears in G98. Here, we are interested in the DLC binned in intervals with size 2α – α is then the semisize of the bin, see below – around the dates in the lightcurve A^{TS} (time delay-shifted lightcurve A). In other words, each photometric measurement A_i^{TS} at the date t_i + $\Delta\tau_{BA}$, where $\Delta\tau_{BA}$ is the time delay, will be compared to the observational data B_j^{MS} = B_j + $< A >$ - $< B >$ at t_i + $\Delta\tau_{BA}$ - α $\leq t_j \leq t_i$ + $\Delta\tau_{BA}$ + α (B^{MS} is the magnitude-shifted lightcurve B). The values B_j^{MS} within each bin are averaged to give $< B_j^{MS} >_i$ (i = 1,...,N), and one obtains the difference lightcurve (DLC)

$$\delta_i =< B_j^{MS} >_i - A_i^{TS}, \tag{5.1}$$

being i = 1,...,N.

The observational process $A^{TS}(t)$ can be expanded as an intrinsic signal $s(t)$ plus a noise process $n_A(t)$ related to the procedure to obtain the measurements, and a microlensing signal $m_A(t)$. Hence, $B^{MS}(t)$ = $s(t)$ + $n_B(t)$ + $m_B(t)$. So, the deviation δ_i must be interpreted as a combination of several factors, i.e.,

$$\delta_i = [< s_j >_i - s_i] + [< n_{Bj} >_i - n_{Ai}] + [< m_{Bj} >_i - m_{Ai}]. \tag{5.2}$$

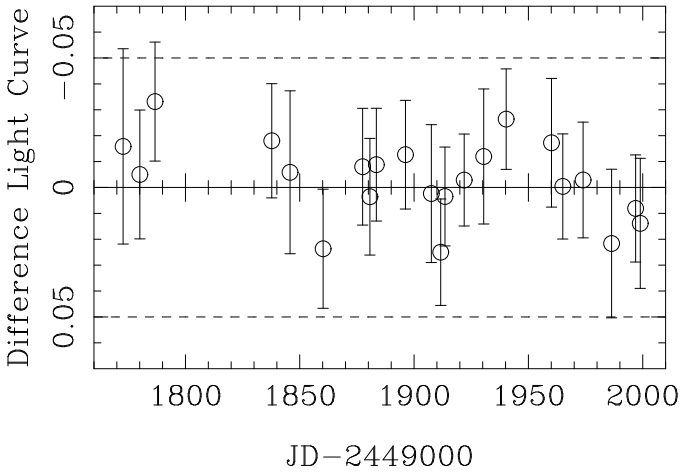

FIGURE 5.2: Difference lightcurve for 1997/1998 seasons – in the R band (magnitudes) –. We used bins with semi-size of 8 days and adopted a time delay of 425 days. The deviations [δ_i; see Equation 5.1] are evaluated at discrete dates corresponding to the time-delay shifted lightcurve $A97$.

If $s(t)$ is a smooth function, then s_i = $s(t_i)$ and s_j = $s(t_j)$, while when $s(t)$ is a stochastic process, s_i represents a realization of the random variable $s(t_i)$ and s_j denotes a realization of the random variable $s(t_j)$. With respect to the observational noise, n_{Ai} is a realization of the random variable $n_A(t_i)$ – similarly, n_{Bj} is one of the possible values of $n_B(t_j)$ –. Also, in Equation 5.2, m_{Ai} = $m_A(t_i)$ and m_{Bj} = $m_B(t_j)$. From Equation 5.2 it is inferred that the difference signal will be never zero, even in absence of microlensing. There is a background dominated by observational noise, which is present in any realistic situation. In the case of very weak or zero microlensing, we expect a trend of the DLC rather consistent with zero (taking into account the standard errors ϵ_1,...,ϵ_N in the deviations estimated from Equation 5.1). However, in the case of strong microlensing, several deviations $|\delta_i|$ should be noticeably larger than the associated uncertainties ϵ_i.

For the 1996/1997 seasons (from the final datasets $A96$ and $B97$), using a time delay of 425 days and bins with semisize of α = 9 days, we derived the DLC that appears in Figure 5.1. Two thresholds are also illustrated: $\pm$0.05 mag (discontinuous lines). In Figure 5.1, there is a 'peak' around day 1615: two neighbour points significantly deviated from the zero line, that verify $|\delta_i| > \epsilon_i$. If the whole DLC is modelled as a single Gaussian event and the data are fitted to the model, we obtain that the amplitude and the full-width at one-tenth maximum (FWTM) of the Gaussian law must be $\approx$33 mmag and $\approx$14 days, respectively (best-fit characterized by χ^2/N $\approx$ 1). Apart from this very short duration event, which is probably caused by observational noise (see next section), there is no evidence in favor of the existence of an event on longer timescales. We note that 'event' is used in a general sense, and it may be due to true microlensing, observational noise, a combination of both or other mechanisms. In particular, no Schild-event (events having a width of three months and an amplitude of $\pm$ 50 mmag; see S96) is found. Although the difference signal is only tested during a 100 days period, the 'sampling' would be sufficient to find a Schild-event belonging to a dense network of similar fluctuations (positive and negative). In any case, from

our second DLC (see here below), we must be able to confirm/reject the existence of a network of events with quarter-year timescale and an amplitude of $\pm$ 50 mmag. Finally, there are bounds derived on the amplitude of the microlensing fluctuations of $\pm$ 0.05 mag, which are similar to the bounds for 1995/1996 seasons.

For the 1997/1998 seasons (from the final datasets $A97$ and $B98$), we also made the corresponding DLC. In Figure 5.2, the DLC and two relevant thresholds are depicted. The difference signal is in apparent agreement with zero, i.e., Figure 5.2 shows a noisy relationship $B^{MS} = A^{TS}$. We observe no Schild-events, and therefore, *the total difference signal ($\approx$ 1 year of overlap between the time-shifted lightcurve for the A component and the magnitude-shifted lightcurve for the B component) is in clear disagreement with the claim that 90 days and $\pm$ 50 mmag fluctuations occur almost continuously*. One can also infer constraints on the microlensing variability. In good agreement with the DLCs for 1995-1997 seasons, a hypothetical microlensing signal cannot reach values outside the very conservative interval [- 0.05 mag, + 0.05 mag]. We finally remark that the methodology introduced by SW98 (the technique of interpolation) leads to DLCs similar to the DLCs discussed here – i.e., Figs. 5.1 and 5.2 present no significant differences from those obtain by SW98 –.

5.3 Interpretation of the difference signal

The DLCs presented in Section 5.2 are in apparent agreement with the absence of a microlensing signal. However, to settle any doubts on the ability of the observational noise in order to generate the observational features (e.g., the very rapid event in Fig. 5.1) and the measured variabilities (rms averages), a more detailed analysis is needed. In this section, we are going to test three simple mechanisms without microlensing. In brief, the ability of some models for generating combined lightcurves and difference signals similar to the observational ones is discussed in detail.

The observational combined photometry consists of both lightcurves A^{TS} and B^{MS} – hereafter, we use 'combined photometry' always in these terms and it will be a synonym of 'combined lightcurve' –. Thus, assuming that $m(t)$ = 0, the combined lightcurve (CLC hereafter) must be related to a process $C(t)$ = $s(t)$ + $n(t)$. The intrinsic signal $s(t)$ is chosen to be either a smooth function (polynomial; picture I) or a polynomial plus a stationary noise process (picture II) or a correlated stationary process (picture III). In the first case (picture I), we work with $s(t) = \sum_{p=0}^{n} a_p t^p$ (when the CLC is reasonably smooth, this intrinsic signal is a suitable choice). The polynomial law leads to $C_k = \sum_{p=0}^{n} a_p t_k^p + n_k$ at a date t_k, where C_k (k = 1,...,N+M) are the combined photometric data. Considering that the process $n(t)$ is Gaussian with $< n(t) >$ = 0 and $\sigma_n^2(t) = < n^2(t) >$, and identifying the measurement errors σ_k^2 with the noise process $\sigma_n^2(t_k)$, the probability distribution of n_k at a given time t_k is $P_k(n_k, t_k) = (1/\sqrt{2\pi}\sigma_k) \exp(-n_k^2/2\sigma_k^2)$. Here, the angle brackets denote statistical expectation values. As the random variables $n(t_k)$, k = 1,...,N+M, are independent (the noise is uncorrelated with itself), the joint probability distribution of the noise

vector $\mathbf{n}$ = (n_1,...,n_{N+M}) is given by

$$P(\mathbf{n}) = \prod_{k=1}^{N+M} P_k$$

$$= (2\pi)^{-\frac{N+M}{2}} \prod_{k=1}^{N+M} (1/\sigma_k) \exp\{-[C_k - \sum_{p=0}^{n} a_p t_k^p]^2/2\sigma_k^2\}. \quad (5.3)$$

Maximizing the likelihood function L =$\ln P$ with respect to the parameters a_p, or equivalently, minimizing χ^2 = $\sum_{k=1}^{N+M}[C_k - \sum_{p=0}^{n} a_p t_k^p]^2/\sigma_k^2$, we find a possible reconstruction of the intrinsic signal (and thus, a model). If this procedure does not work (e.g., χ^2/dof is relatively large, with dof = N+M-(n+1) being the number of degrees of freedom), we perform a fit including a stationary intrinsic noise as an additional ingredient (picture II). This new ingredient can account for noisy CLCs. The intrinsic noise $\eta(t)$ is taken to be Gaussian with $< \eta(t) >$ = 0 and $\sigma_\eta^2(t) = \sigma_{int}^2$, and moreover, $\eta(t)$ is uncorrelated with both $n(t)$ and with itself. Now, $C(t)$ = $\hat{s}(t)$ + $\xi(t)$, where $\hat{s}(t)$ = $\sum_{p=0}^{n} a_p t^p$ and $\xi(t)$ = $n(t)$ + $\eta(t)$, and we focus on the global noise process $\xi(t)$. As the processes $n(t)$ and $\eta(t)$ are Gaussian and mutually independent, their sum is again Gaussian, and the average and variance of $\xi(t)$ are the sums of the averages and variances of both individual noise processes. The probability distribution of ξ_k at an epoch t_k can be written as $P_k(\xi_k, t_k)$ = [$1/\sqrt{2\pi}(\sigma_k^2+\sigma_{int}^2)^{1/2}$] exp[-$\xi_k^2/2(\sigma_k^2 + \sigma_{int}^2)$], and the joint probability distribution of the noise vector ξ = (ξ_1,...,ξ_{N+M}) should be $P(\xi)$ = $\prod_{k=1}^{N+M} P_k(\xi_k, t_k)$. Finally, instead of the standard procedure (to maximize the likelihood function), we equivalently minimize the function

$$\hat{\chi}^2 = \sum_{k=1}^{N+M} \{\ln(\sigma_k^2 + \sigma_{int}^2) + [C_k - \sum_{p=0}^{n} a_p t_k^p]^2/(\sigma_k^2 + \sigma_{int}^2)\}. \quad (5.4)$$

Through this method, the intrinsic signal is partially reconstructed. We find the coefficients of the polynomial and the variance of the intrinsic noise, but after the fit, the realizations η_k (k = 1,...,N+M) remain unknown. However, the derived model permits us to make simulated CLCs and DLCs, since only the knowledge of the smooth intrinsic law and the statistical properties of the noise processes are required for this purpose.

A very different procedure was suggested by Press, Rybicki & Hewitt (1992 a,b, hereafter PRH92). They assumed the intrinsic signal to be a correlated stationary process. For this case III, it is possible to reconstruct the realizations of $s(t)$, provided that the correlation properties are known. PRH92 considered that the observational noise $n(t)$ is uncorrelated with $s(t)$ (and with itself), and therefore, only the autocorrelation function $K_s(\tau) = < \tilde{s}(t)\tilde{s}(t+\tau) >$ is needed, being $\tilde{s}(t) = s(t) - < s >$. The autocorrelation function of the intrinsic signal is not known a priori and must be estimated through the CLC. We can relate the autocorrelation properties to the first-order structure function $D_s^{(1)}(\tau)$ by

$$D_s^{(1)}(\tau) = (1/2\nu) \sum_{l,m} (s_m - s_l)^2$$

$$\approx \frac{1}{2} < [\tilde{s}(t+\tau) - \tilde{s}(t)]^2 >= K_s(0) - K_s(\tau), \quad (5.5)$$

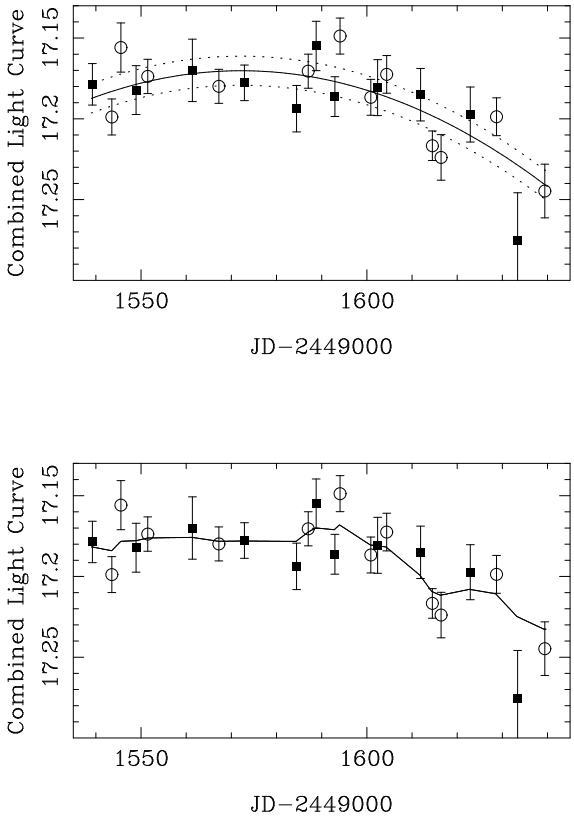

FIGURE 5.3: The combined photometry of Q0957+561A,B for the 1996/1997 seasons in the R band (magnitudes) – at Teide Observatory –. The open circles trace the time-shifted (+ 425 days) lightcurve $A96$ and the filled squares trace the magnitude-shifted (+ 0.0658 mag) lightcurve $B97$. The lines are related to two reconstructions of the intrinsic signal: considering an intrinsic signal of the kind polynomial plus stationary noise (top panel) and the optimal reconstruction following the PRH92 method (bottom panel).

where the sum only includes the (l,m) pairs verifying that $t_m - t_l \approx \tau$ (the number of such pairs is ν). From the CLC, one infers (e.g., Haarsma et al. 1997)

$$D_s^{(1)}(\tau) \approx (1/2\nu) \sum_{l,m} [(C_m - C_l)^2 - \sigma_l^2 - \sigma_m^2], \tag{5.6}$$

which is an evaluation of the difference $K_s(0)$ - $K_s(\tau)$. As usual we assume a power-law form for the first-order structure function, and perform a fit to the power law. Finally, the variance of the intrinsic process $K_s(0)$ is assumed to be the difference between the variance of the CLC and a correction due to the observational noise. The whole technique is described in PRH92 and other more recent papers (e.g., Haarsma et al. 1997).

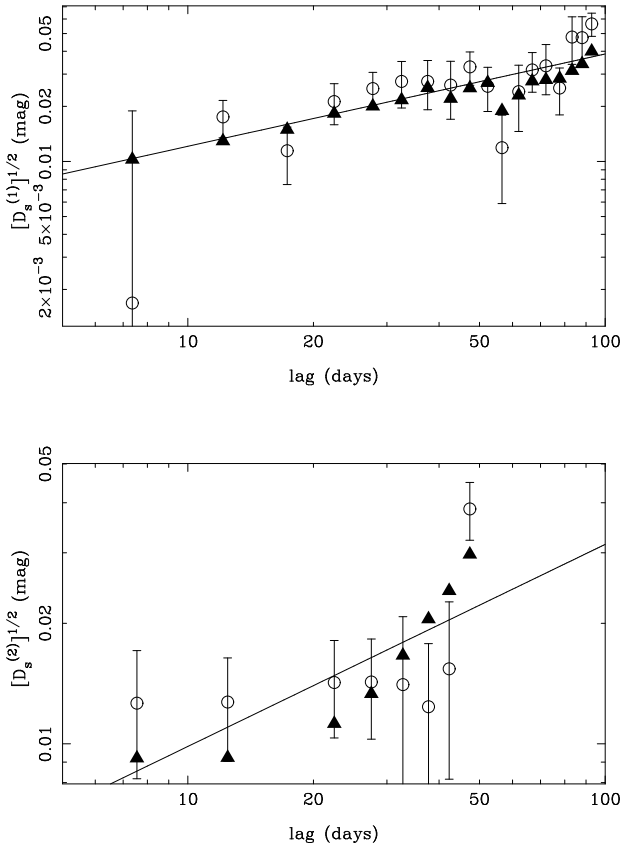

FIGURE 5.4: The first-order and second-order structure functions (1996/1997 seasons of Q0957+561 in the R band). The open circles are the values inferred from the observational data and the filled triangles are the predictions from the reconstruction using a polynomial + stationary noise. The observational first-order structure function was fitted to a power-law $E\tau^{\varepsilon}$ (solid line in the top panel). Assuming this fit as an estimation of the autocorrelation properties of a hypothetical correlated stationary process ($K_s(0)$ - $K_s(\tau)$), the predicted second-order structure function is illustrated by a solid line in the bottom panel.

5.3.1 The 1996/1997 seasons

For the 1996/1997 seasons, we first determined the corresponding combined lightcurve (CLC). In a second step, using the picture I (see above), we attempted to fit the combined photometry. A quadratic law (n = 2) gives χ^2/dof = 1.65 (best fit), whereas $\chi^2/dof(n = 1)$ = 2.52, $\chi^2/dof(n = 3)$ = 1.74 and $\chi^2/dof(n = 4)$ = 1.83. Thus the modelling of the CLC has proven to be difficult. Fortunately, the inclusion of intrinsic noise (picture II) with moderate variance helps to generate an acceptable fit. When the intrinsic signal is the previous best quadratic fit to which an intrinsic noise with σ_{int} = 9 mmag is added, we obtain χ^2/dof = 1.15 ($\chi^2/(N+M) = 0.95$ and $dof = N + M - 1$). The quality of the fit has improved significantly with the addition of the new noise, whose variance (σ_{int} = 9 mmag) is less than the mean variance of the observational noise (= 12-16 mmag). In Figure 5.3 (top panel) the CLC and the reconstruction are presented. The open circles represent the time-shifted lightcurve $A96$, while the filled squares are the magnitude-shifted

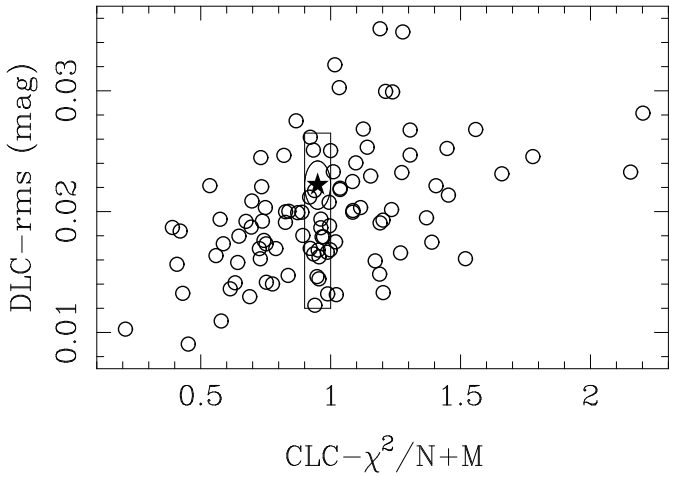

FIGURE 5.5: Global properties of the measured photometry for Q0956+561 data of the 1996/1997 seasons (filled star) and 100 simulation lightcurves (open circles). The rectangle highlights the simulations with $0.9 \leq \chi^2/(N+M) \leq 1.0$. The numerical simulations arise from M1, which is a model with three ingredients: polynomial law + intrinsic noise + observational noise.

lightcurve $B97$. The best polynomial (n = 2) is traced by means of a solid line, and the two lines with points are drawn at $\pm$ 9 mmag (the best value of σ_{int}) from the polynomial. Apart from the CLC, we checked the observational structure functions $D_s^{(1)}$ (see Equation 5.5) and $D_s^{(2)}$ (Equation 5.7)as well as the predictions (with respect to the structure functions) from our first succesful reconstruction. The observational second-order structure function is computed in the following way (see Simonetti, Cordes & Heeschen 1985; we take a normalization factor equal to 1/6):

$$D_s^{(2)}(\tau) \approx (1/6\mu) \sum_{l,m,n} [(C_n - 2C_m + C_l)^2 - \sigma_l^2 - 4\sigma_m^2 - \sigma_n^2], \tag{5.7}$$

where μ is the number of (l,m,n) valid triads so that $t_m - t_l \approx \tau$ and $t_n - t_l \approx 2\tau$. The predicted structure functions are

$$D_s^{(1)}(\tau) \approx (1/2\nu) \sum_{l,m} [\hat{s}(t_m) - \hat{s}(t_l)]^2 + \sigma_{int}^2,$$
$$D_s^{(2)}(\tau) \approx (1/6\mu) \sum_{l,m,n} [\hat{s}(t_n) - 2\hat{s}(t_m) + \hat{s}(t_l)]^2 + \sigma_{int}^2, \tag{5.8}$$

where $\hat{s}(t)$ is the fitted quadratic law. Figure 5.4 shows the good agreement between the observational values (open circles) and the predicted trends (filled triangles). This result confirms that the reconstruction is reliable. The meaning of the two straight lines in Figure 5.4 will be explained here below.

Our interest in this work is less directly in the details of a given reconstruction of the underlying intrinsic signal than it is in analyzing simulated datasets consistent with the reconstruction and

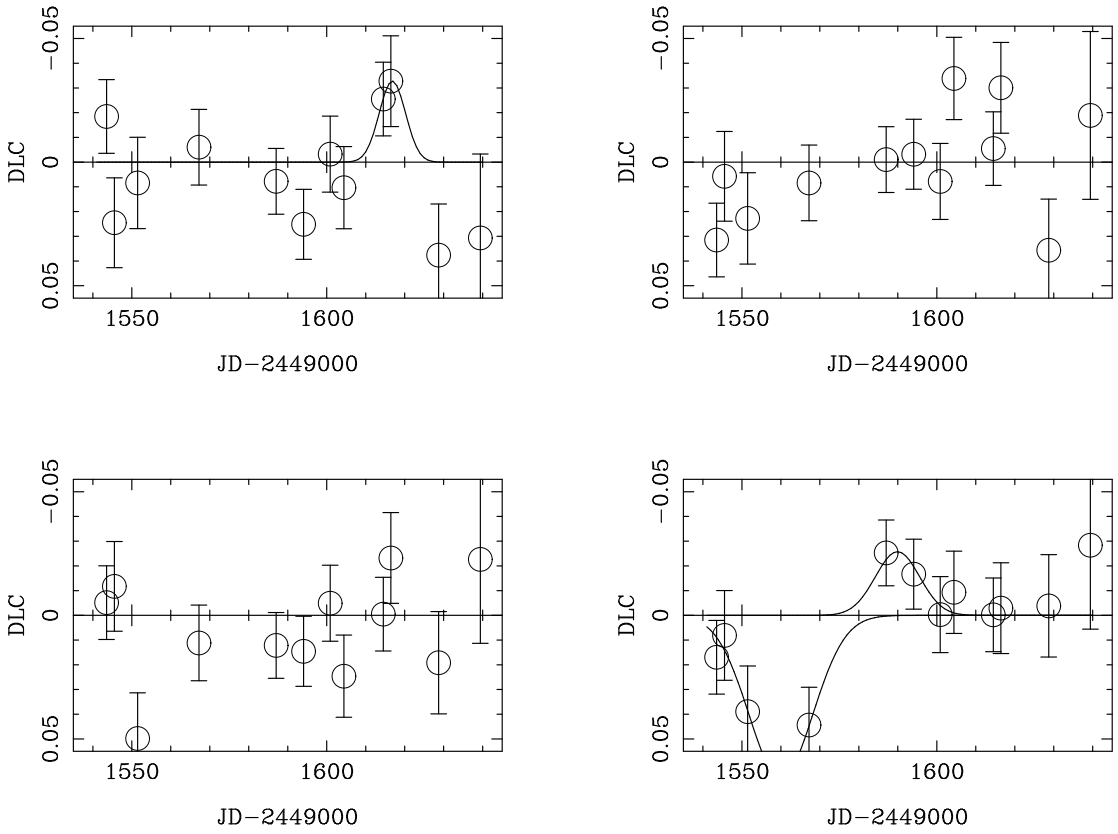

FIGURE 5.6: The true DLC for 1996/1997 seasons (left-hand top panel) together with 3 simulated DLCs (via M1) – all in magnitudes –. The solid lines are fits to Gaussian events. A curious result observed in the simulated DLCs is the existence of events, which could be naively interpreted as microlensing fluctuations.

with the same sampling (dates) and errors as the measured data. The first model (M1) comprises the best quadratic fit in the absence of intrinsic noise (a smooth component) and a Gaussian noise process characterized by a known variance at discrete times t_k: σ_k^2 + σ_{int}^2. From M1 we derived 100 simulated CLCs and the corresponding DLCs. We remark that, in each simulation (CLC), N simulated data points represent a synthetic lightcurve A^{TS}, while the other M data are simulated measurements of the magnitude-shifted lightcurve B. Figure 5.5 shows the relationship between the values of χ^2/(N+M) (χ^2 = $\sum_{k=1}^{N+M}[C_k - \hat{s}(t_k)]^2/[\sigma_k^2 + \sigma_{int}^2]$) and the rms averages of the DLCs (rms = $[\frac{1}{N}\sum_{i=1}^{N}\delta_i^2]^{1/2}$). The 100 open circles are associated with the simulated photometries and the filled star is related to the measured lightcurve. The true (measured) lightcurves appears as a typical result of the model. One sees in the figure a broad range for CLC-χ^2/(N+M) (0.2-2.2) and DLC-rms (8-36 mmag), and the true values of CLC-χ^2/(N+M) = 0.95 and DLC-rms = 22 mmag are well placed close to the centre of the open circle distribution. Thus, the measured combined photometry seems a natural consequence of M1, which is a model without rapid and very rapid microlensing. However, due to the event found in Figure 5.1 (around day 1615) and other local features less prominent than the event, we check this conclusion analysing the details in the synthetic DLCs. In Figure 5.5, to provide some guidance, the open circles corresponding

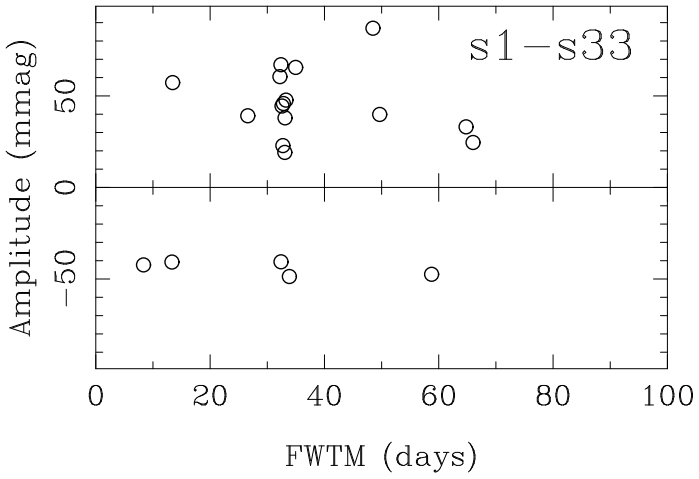

FIGURE 5.7: Gaussian events (they are classified according to their amplitude and FWTM) found in the first 33 simulations via M1. The number of features as well as the amplitudes and time-scales show that noise can explain most of the fluctuations.

to simulated datasets with CLC-χ^2/(N+M) similar to the measured value have been enclosed in a rectangular box. Also, we have drawn an elliptical surface centred on the filled star, which includes (totally or partially) three open circles associated with the synthetic lightcurves analogous (global properties of both the CLC and the DLC) to the true brightness record. As we must put into perspective the very rapid event and other local properties discovered in the true DLC for 1996/1997 seasons, this DLC and its features were compared with the three DLCs that arise from the simulations. In Figure 5.6 we present the comparison. All events (each event includes a set of two or more consecutive deviations which have equal sign and are not consistent with zero) has been fitted to a Gaussian law and marked in the figure. The measured DLC (left-hand top panel and Fig. 5.1) is not different to the other three. In fact, in our 100^{th} simulation (s100; right-hand bottom panel), two events appear. The positive event is more prominent than the negative event, and this last one is similar to the measured one. With respect to the regions without events, the true variability cannot be distinguished from the simulated ones – i.e., the observed variability is entirely consistent with noise –. To throw more light upon the problem, we searched for Gaussian events in 1/3 of all simulations (s1-s33), as a sample of the whole set of simulations because the computation turned out to be very time-consuming. The results are plotted in Figure 5.7: amplitude of each event (mmag) vs. FWTM (days). There are a lot of events with amplitude in the interval [- 50 mmag, + 90 mmag] and duration $<$ 70 days. In particular, the probability of observing a negative event is 15% and the probability of observing one or more events is about 50%. So, it must be concluded that *the noisy (around zero) difference lightcurve based on observations is totally consistent with M1, and the deviations from the zero line can be caused by the combined effect of the processes $n(t)$ – the Gaussian noise process – (main contribution) and $\eta(t)$* – the stationary noise process –.

We also propose a reconstruction of the underlying intrinsic signal as realizations of a correlated

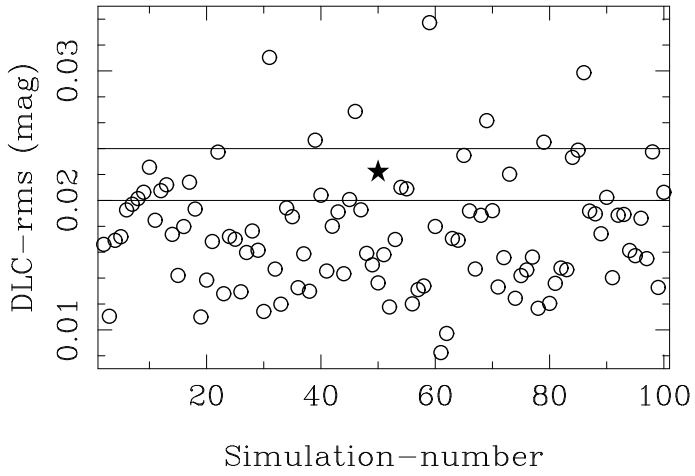

FIGURE 5.8: Global properties of the true DLC for 1996/1997 seasons (filled star) and 100 simulated DLCs (open circles). The numerical simulations were made through a model including the optimal reconstruction of a correlated stationary process and a Gaussian observational noise process whose variance at the dates of the real data is known.

stationary process (picture III). The observational first-order structure function can be fitted to a power-law $E\tau^{\varepsilon}$ (see Fig. 5.4, solid line in the top panel). If one considers this fit as an estimate of the difference $K_s(0)$ - $K_s(\tau)$ for a correlated stationary process, then it is straightforward to obtain the predicted second-order structure function (see Fig. 5.4, solid line in the bottom panel: the prediction is irrelevant to reconstruct the intrinsic signal, but it is necessary for testing the consistency of the starting point $K_s(0)$ - $K_s(\tau) = E\tau^{\varepsilon}$) and to apply the reconstruction formalism by PRH92. Therefore, we are able to find the realizations of the intrinsic process at the observational times t_k (k = 1,...,N+M) as well as in the gaps between the observations. The PRH92 technique leads to an acceptable fit with χ^2/dof = 1.18 (dof = N+M-1), and our second successful reconstruction is showed in Figure 5.3 (bottom panel). The knowledge of both the optimal reconstruction and the properties of the Gaussian observational noise process at discrete times t_k (k = 1,...,N+M), permits us to make 100 new simulations. In Figure 5.8 details of the rms averages of the DLCs are provided (open circles). The observational DLC has a rms average (filled star) similar to the rms average in a 1/5 (20%) of the simulated DLCs. Furthermore, four simulated DLCs with rms in the interval [20 mmag, 24 mmag] (in Fig. 5.8, this range of variability is labeled with two horizontal lines) appear in Figure 5.9. From the new model (M2), DLCs with no events (as in the analysis presented above, the Gaussian events are related to 'peaks', or in other words, we only made events around consecutive multiple deviations with equal sign and well separate from zero) and DLCs that incorporate more or less prominent features are derived. We note that one DLC (right-hand bottom panel) has an event almost identical to the true one in Figures 5.1 and 5.6. Figure 5.10 shows the properties of all Gaussian events in the simulated DLCs with rms in the vicinity of the observational rms (open circles). The measured event is also depicted (filled star), and we can see two simulated events analogous to it. We finally conclude that *the observational DLC is in clear agreement with M2,*

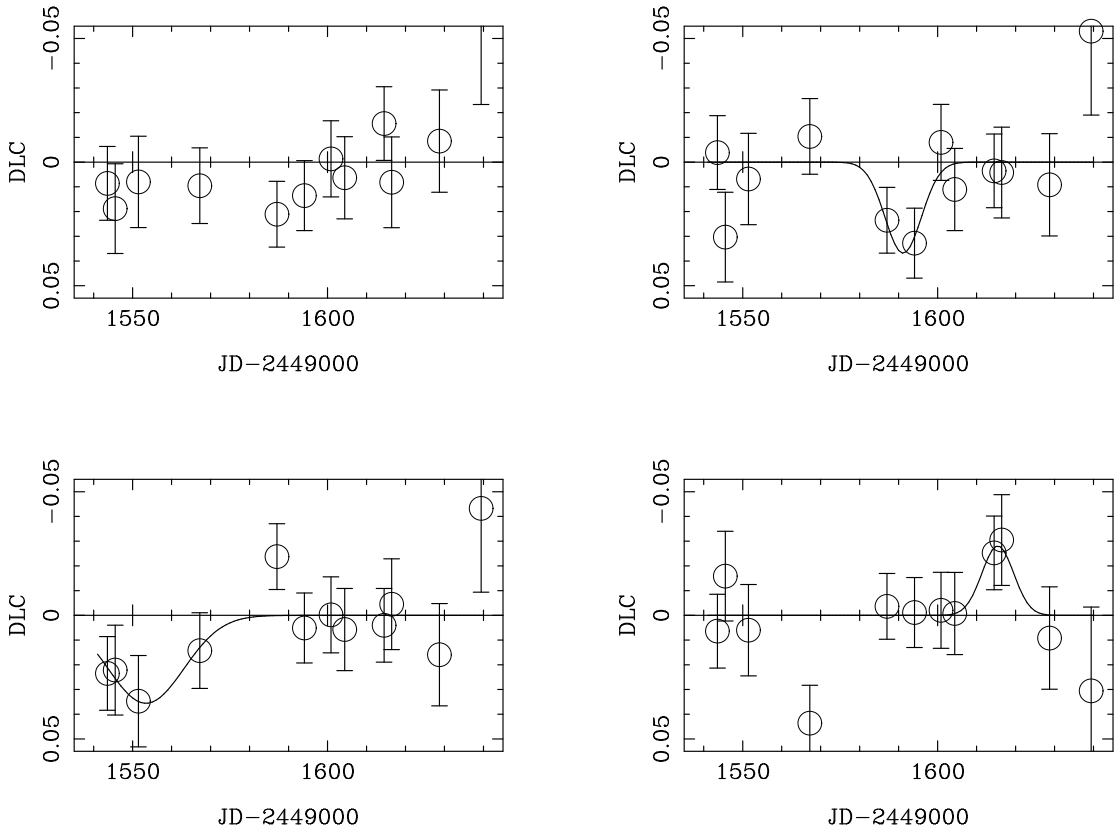

FIGURE 5.9: Four simulated DLCs (via M2). For comparison with the true event in Figure 5.1 (see also Fig. 5.6), the Gaussian events have been clearly marked on the panels.

and so, microlensing would be not advocated. In this framework (M2), the observational noise process can originate the measured deviations.

5.3.2 The 1997/1998 seasons

The combined photometry for 1997/1998 seasons and the reconstruction based on a polynomial fit are showed in Figure 5.11 (top panel). The open circles represent the time-shifted lightcurve $A97$ and the filled squares are the magnitude-shifted brightness record $B98$. There is no need for the presence of an intrinsic noise, and a simple quadratic law works well, leading to χ^2/dof = 0.85 (best fit). In Figure 5.11 (top panel), the solid line traces the reconstruction of the intrinsic signal. Besides the comparison between the measured CLC and the fitted polynomial, we tested the predicted structure functions. In Figure 5.12 we present the observational $D_s^{(1)}$ and $D_s^{(2)}$ (open circles; see Eqs. (6-7)) and the predictions from the best quadratic fit (filled triangles; see Eqs. (8) with σ_{int} = 0). The laws traced by the dashed and solid lines in this figure will be discussed below. It is evident that the behaviours deduced from observations and the predicted trends agree very well, and this result indicates that the reconstruction is robust.

The first model for 1997/1998 seasons (M3) consists of the best quadratic fit together with a

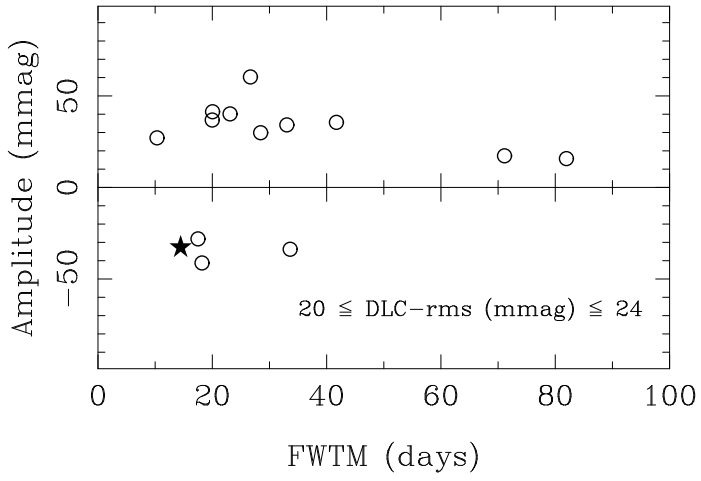

FIGURE 5.10: Gaussian events found in the numerical simulations (via M2) with 20 $\leq$ rms (mmag) $\leq$ 24 (open circles). Events very similar to the real event (filled star) are produced in two simulations.

Gaussian observational noise process (whose variance is σ_k^2 at discrete times t_k, k = 1,...,N+M, being σ_k the measurement errors at the dates of observation t_k). Using M3 we performed 100 simulated CLCs (and consequently, 100 simulated DLCs). The global properties of the simulated photometries (open circles) and the true dataset (filled star) are depicted in Figure 5.13. If we concentrate on the simulations with χ^2/N+M similar to the measured value (rectangular box), the true DLC has a rms relatively small (of about 15 mmag), but consistent with the rms distribution associated with the simulated DLCs. We remark that 3 simulations (open circles in the elliptical surface around the filled star) are analogous to the real brightness record, and in Figure 5.14, their DLCs can be compared with the true DLC. The measured difference signal (left-hand top panel and Fig. 5.2) is a quasi-featureless trend and similar to the other synthetic DLCs. There are no significant events in these four DLCs with small global variability. We conclude that *a model with no microlensing (M3) has the ability of generating ligth curves like the real data for 1997/1998 seasons*. Henceforth, we are going to treat the 'peaks' as top-hat fluctuations, i.e., given a 'peak' including deviations δ_{P1},...,δ_{PP} at times t_{P1},...,t_{PP}, the amplitude and duration of the associated top-hat profile will be evaluated as the average of the individual deviations and the difference $t_{PP} - t_{P1}$, respectively. In Figure 5.14, a 'peak' (defined by two contiguous negative deviations, which are inconsistent with zero) appears in the DLC from the 7^{th} simulation (s7; right-hand top panel). The 'peak' is marked by a double arrow that represents the amplitude and duration of the associated top-hat profile.

The analysis of the observational first-order structure function (see Fig. 5.12) suggests that the underlaying law could be intricate. To find the autocorrelation properties of a possible and plausible correlated stationary process causing the main part of the observed signal (picture III), this observational structure function was firstly fitted to a non-standard law $D_s^{(1)}(\tau) = E\tau^{\varepsilon}/[1+(\tau/T)^{\lambda}]^2$. As showed in Figure 5.12 (dashed line in the top panel), the fit is excellent. However, when we attempt to reproduce the observational second-order structure function, an inconsistent prediction

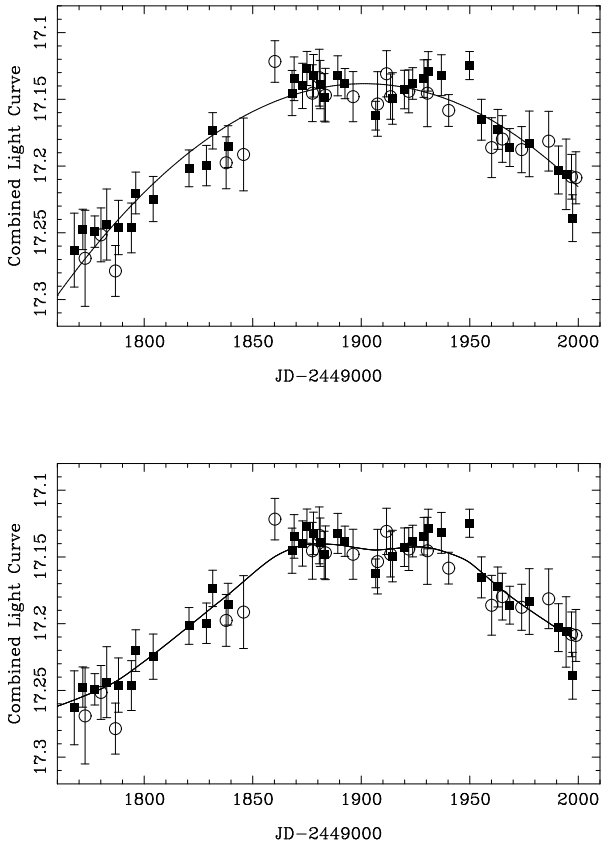

FIGURE 5.11: The combined photometry for 1997/1998 seasons in the R band (at Teide Observatory). The open circles trace the time-shifted (+ 425 days) lightcurve $A97$ and the filled squares trace the magnitude-shifted (+ 0.0603 mag) lightcurve $B98$. The solid lines represent two reconstructions of the intrinsic signal: the best quadratic fit (top panel) and the optimal reconstruction following the PRH92 method (bottom panel).

is derived (dashed line in the bottom panel). The prediction fails at $\tau < 70$ days. Other functions led to fits more or less successful, and finally we adopted the point of view by PRH92. In Figure 5.12 (top panel) one sees a power-law behaviour up to τ = 140 days. The drop at the largest lags is due to the coincidence of values in the starting and ending parts of the measured CLC. Therefore, we assume that the observational first-order structure function is a reliable estimator of $K_s(0)$ - $K_s(\tau)$ at $\tau \leq 140$ days, whereas it is a biased estimator at $\tau > 140$ days. The power-law fit to the data at lags $\tau \leq 140$ days gives the autocorrelation properties for the correlated stationary process, shown as a solid line in the Figure 5.12 (top panel). The predicted second-order structure function (Fig. 5.12, solid line in the bottom panel) is consistent with the observational one up to a lag of 70 days, and it deviates from the observational trend at $\tau > 70$ days. However, since the observational second-order structure function at lag τ is associated with the autocorrelation at lag 2τ, the observational $D_s^{(2)}(\tau > 70$ days) will be related to the autocorrelation at $\tau > 140$ days, which is poorly traced from observations. Thus the deviation at largest lags is reasonable and the

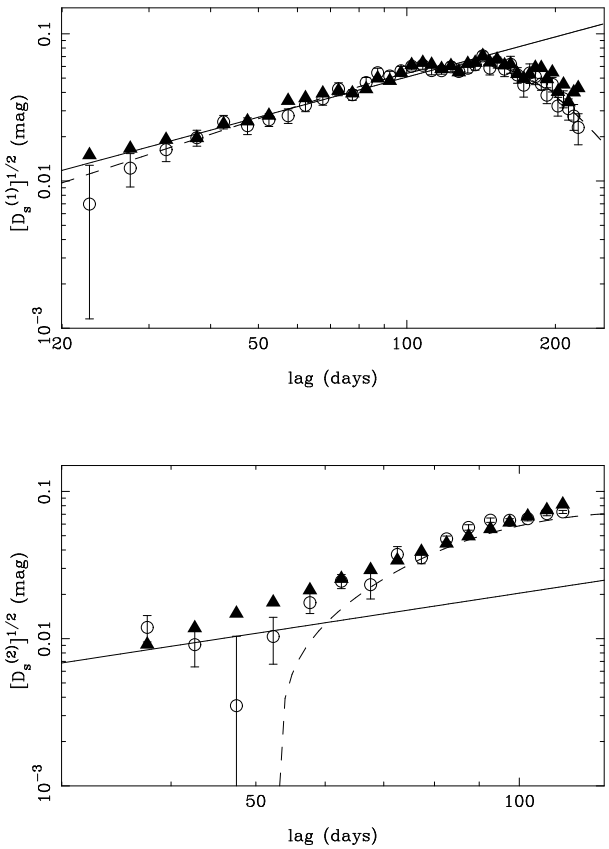

FIGURE 5.12: The first-order and second-order structure functions (1997/1998 seasons in the R band). The open circles are the values inferred from the observational data and the filled triangles are the predictions from the reconstruction of the kind polynomial. The observational first-order structure function was fitted to different laws, and two 'reasonable' fits are drawn in the top panel (dashed and solid lines). If the fits are interpreted as the difference $K_s(0)$ - $K_s(\tau)$ for a correlated stationary process, the corresponding predicted second-order structure functions are illustrated by two lines in the bottom panel.

global prediction should be considered as a consistent result.

Once the relationship between the structure function and the autocorrelation has been established, we can directly obtain both an optimal reconstruction of the realizations of the intrinsic signal and a new model (M4). The relatively smooth reconstruction is showed in Figure 5.11 (bottom panel; the χ^2/dof value is of 0.86), and the associated model leads to 100 simulations, whose global properties (rms averages of the DLCs) are presented in Figure 5.15 (open circles). In Figure 5.15, a filled star represents the true rms average, which is consistent (although marginally) with the rms distribution from simulations. Finally, four simulated DLCs with rms $\leq$ 17 mmag (in Fig. 5.15, the upper limit of 17 mmag is marked with one horizontal line) have been selected for a more detailed inspection. We found noisy behaviours around zero and no events in these synthetic DLCs, i.e., the results agree with the analysis of the real difference signal for 1997/1998 seasons. The 4 quasi-featureless simulated DLCs appear in Fig. 5.16. We again showed that *microlensing*

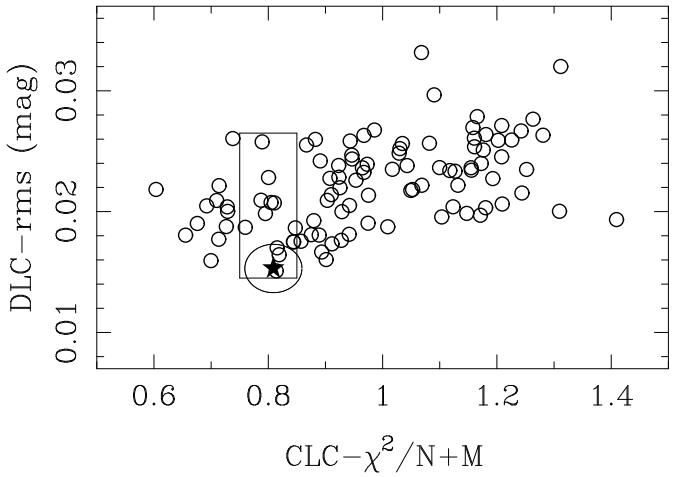

FIGURE 5.13: Global properties of the true photometry for 1997/1998 seasons (filled star) and 100 simulated photometries (open circles). The numerical simulations are based on a polynomial plus observational noise model.

is not necessary. The real combined photometry and difference signal can be due to a set of realizations of two very different processes: a correlated stationary process (intrinsic) and a Gaussian noise (observational).

5.4 The ability of the IAC-80 telescope to detect microlensing 'peaks'

The sensitivity of the IAC-80 telescope to microlensing variability in a given observational DLC is an important issue which merits more attention. To explain the observations for 1996/1997 seasons and 1997/1998 seasons, we proposed (in Sect. 3) four models based on pictures including only an intrinsic signal and observational noise. The simulations arising from these models (100 simulated difference lightcurves per model) are a useful tool to study the statistical properties of the expected difference signal in the absence of microlensing, and so, to test the resolution of the IAC-80 telescope for microlensing variability. In Figure 5.17 we present the probability distributions of the rms values (DLCs) derived from M1 (solid line) and M2 (dashed line). A value of about 20 mmag has a relatively high probability of 20-40%, while a rms exceeding 36 mmag is inconsistent with both models, as can be seen in Figure 5.17. Figure 5.18 also shows the probability of observing (in the absence of microlensing) different rms values: via M3 (solid line) and via M4 (dashed line). The rms averages in the interval 19-27 mmag are highly probable (20-40%), but a global variability characterized by either rms $\leq$ 12 mmag or rms $\geq$ 38 mmag can be excluded. As a general conclusion, the rms of the difference signal induced by noise does not exceed a threshold of 37 mmag. Therefore, *the rms values of future observational DLCs can be used to discriminate between the presence of the expected background (global variability with rms*

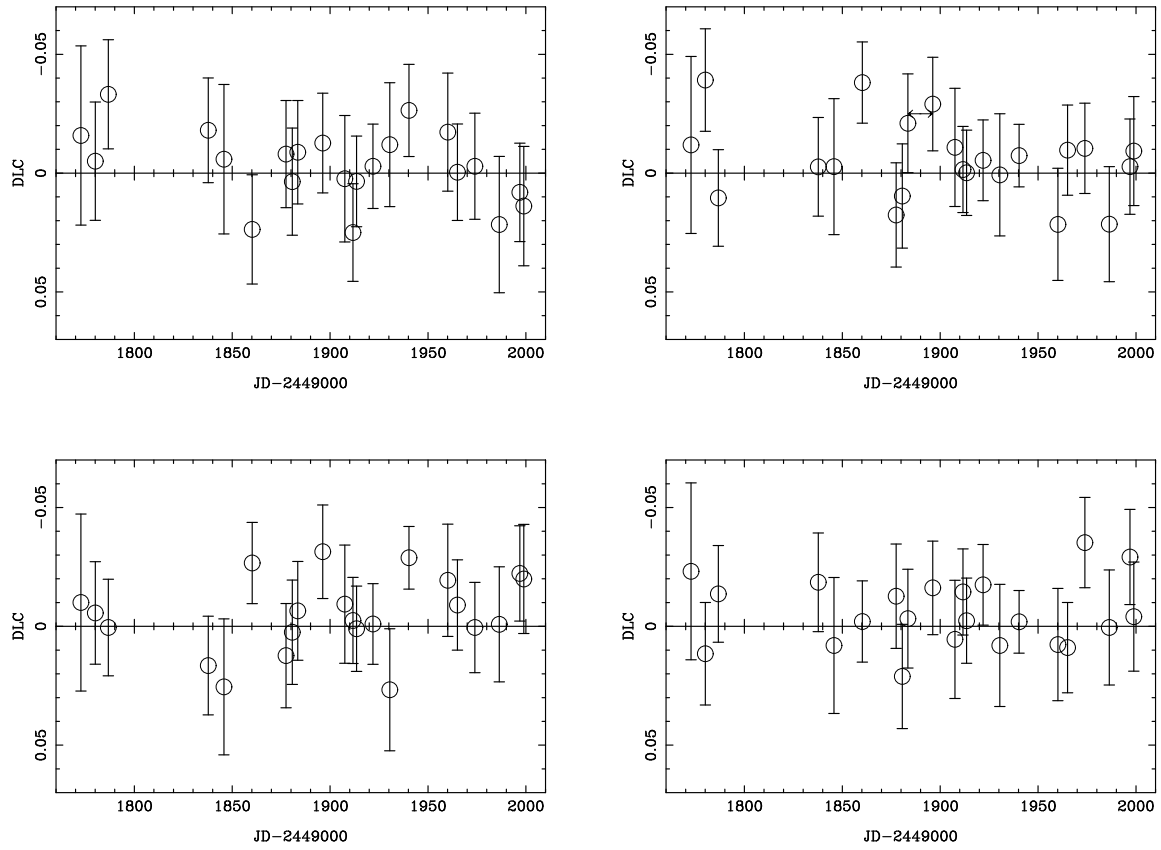

FIGURE 5.14: The true DLC for 1997/1998 seasons (left-hand top panel) together with 3 simulated DLCs (via M3). An only 'peak' is marked by a double arrow (see right-hand top panel).

$<$ 40 mmag) and the probable existence of true microlensing signal (rms $\geq$ 40 mmag).

The previous discussion on the global variability is interesting, but it is not the main goal of this section. Our main goal lies in discussing the sensitivity of the telescope (taking into account typical sampling, photometric errors, re-reduction and making of bins) to several classes of microlensing 'peaks' (the cores of the microlensing events). We have seen, in Sect. 3, a figure that shows the properties of the Gaussian events (amplitude and FWTM) found in a subset of simulations from M1 (see Fig. 5.7). Figure 5.7 can be compared to the distribution of top-hat fluctuations found in all DLCs generated with M1. In Figure 5.19 the distribution of the top-hat fluctuations (basically the properties of the 'peaks' associated with them) appears, and a direct comparison between Figures 5.7 and 5.19 indicates the logical fact that Gaussian fits lead to longer durations than top-hat estimates. In the case of Gaussian fits, events with a duration (FWTM) of 1-2 months are abundant and only features with a timescale $>$ 70 days are ruled out. However, the 'peaks' (from M1) with a timescale of about one month are scarce. To discuss the power of resolution of the telescope for local microlensing variability we chose the top-hat fluctuations ('peaks') instead of the events. The properties of an event (around a 'peak') depend on the assumed profile (e.g., Gaussian, Lorentzian, etc.) and the global behaviour of the DLC, whereas the top-hat shape directly traces the 'peaks', avoiding to make assumptions on their wings and the use of the rest of the corresponding DLCs.

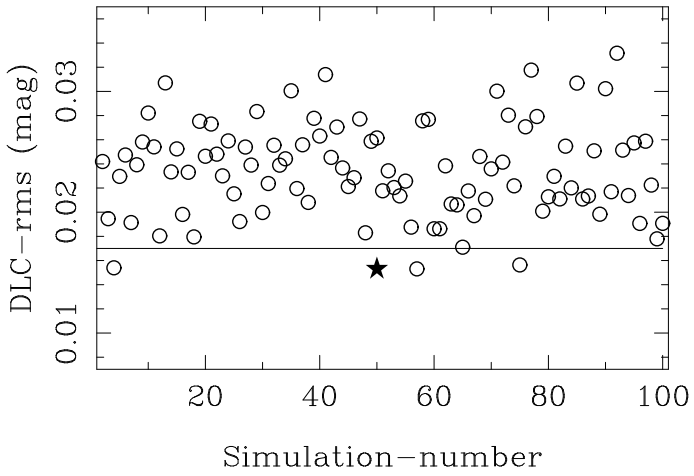

FIGURE 5.15: Global properties of the true DLC for 1997/1998 seasons (filled star) and 100 simulated DLCs (open circles). The numerical simulations were made from M4 (see main text).

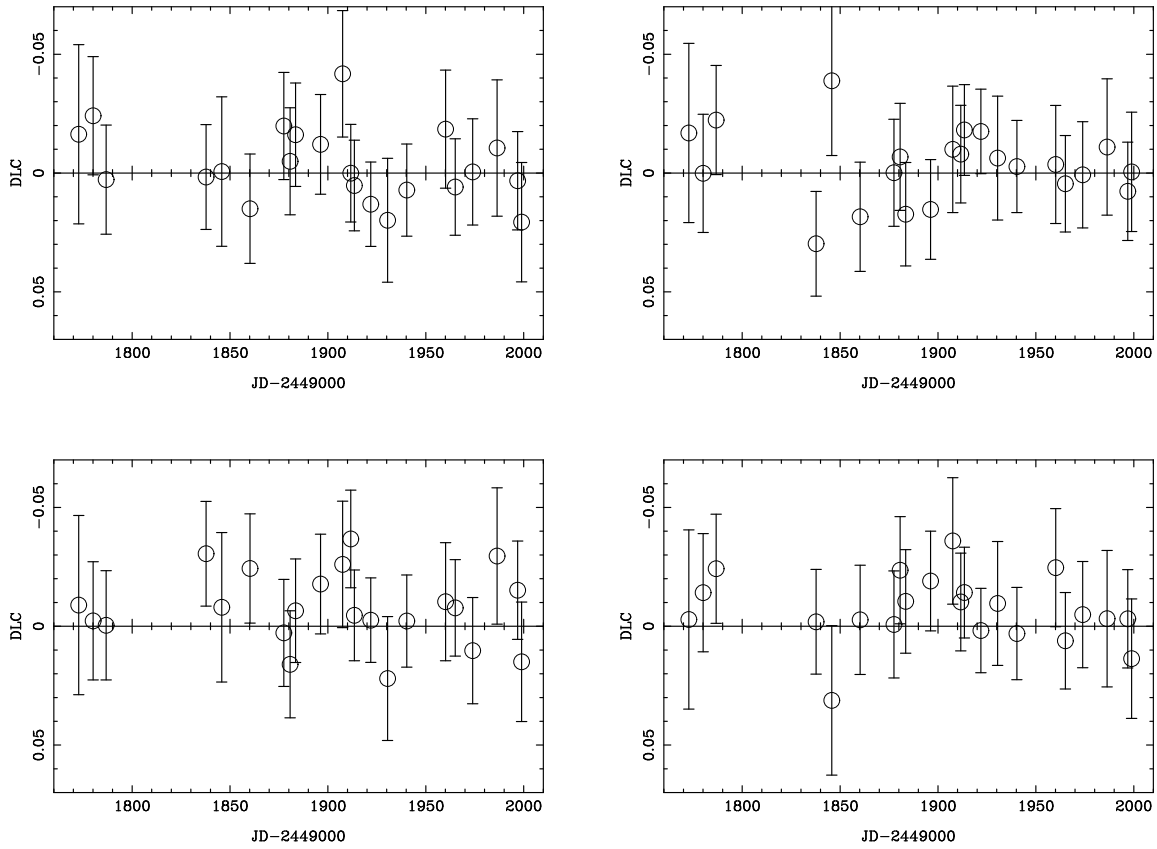

FIGURE 5.16: Four simulated DLCs via M4. No events are found (for a comparison, see Fig. 5.2).

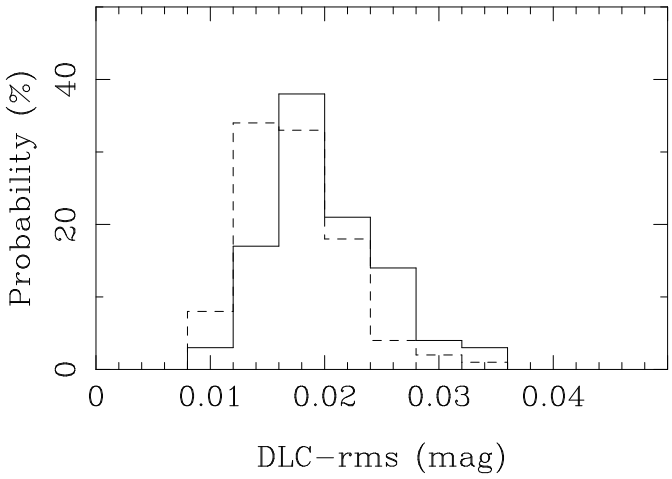

FIGURE 5.17: Probability distributions of the rms averages of the synthetic DLCs. The numerical simulations were made from M1 (solid line) and M2 (dashed line).

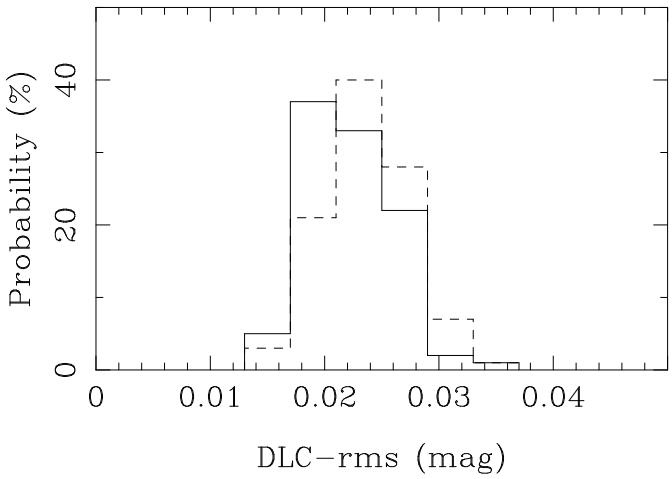

FIGURE 5.18: Probability distributions of the rms averages of the synthetic DLCs. The numerical simulations are based on M3 (solid line) and M4 (dashed line).

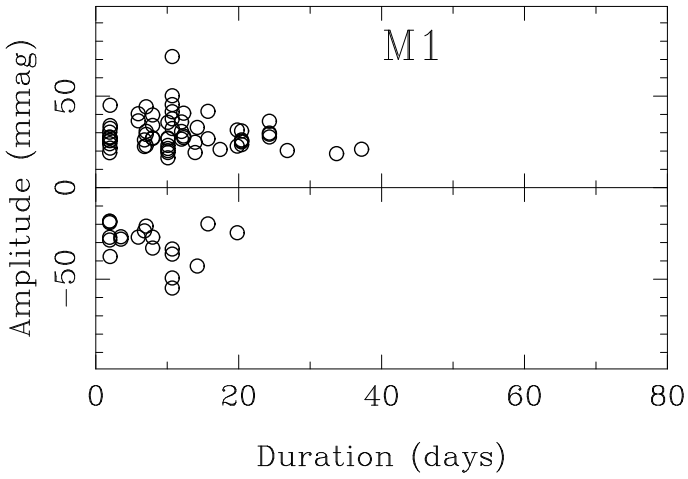

FIGURE 5.19: Top-hat fluctuations found in the numerical simulations based on M1. We show 84 features that appear in 100 simulated DLCs.

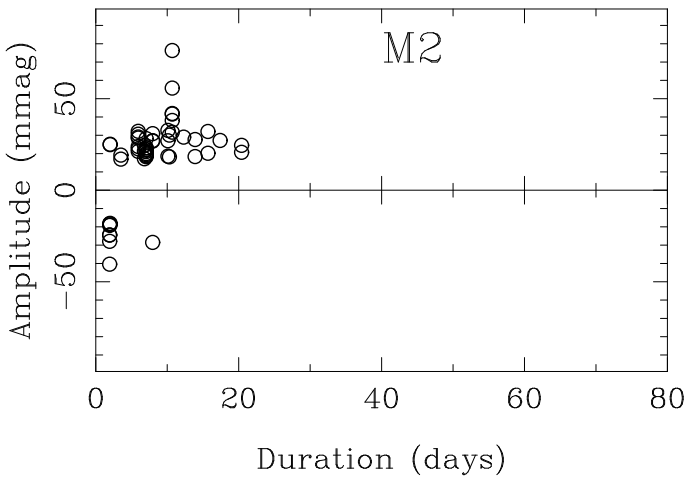

FIGURE 5.20: Top-hat fluctuations in 100 simulated (via M2) DLCs. They were found 55 'peaks'.

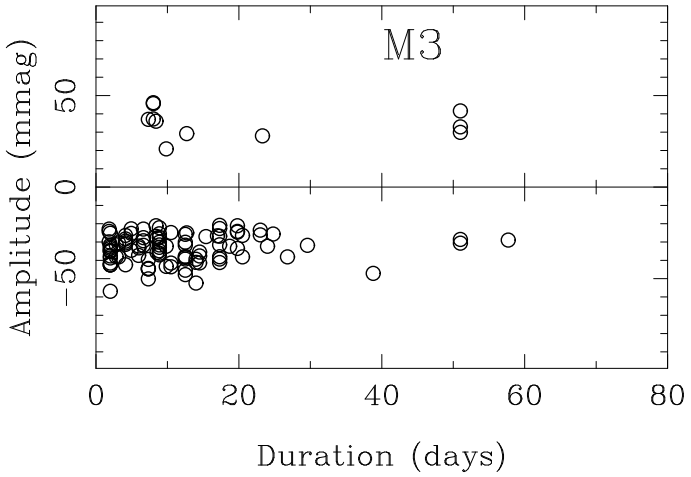

FIGURE 5.21: Top-hat fluctuations from M3. We note the existence of noise 'peaks' with a duration longer than 40 days. All these features are however associated with an unfortunate small gap in our photometry.

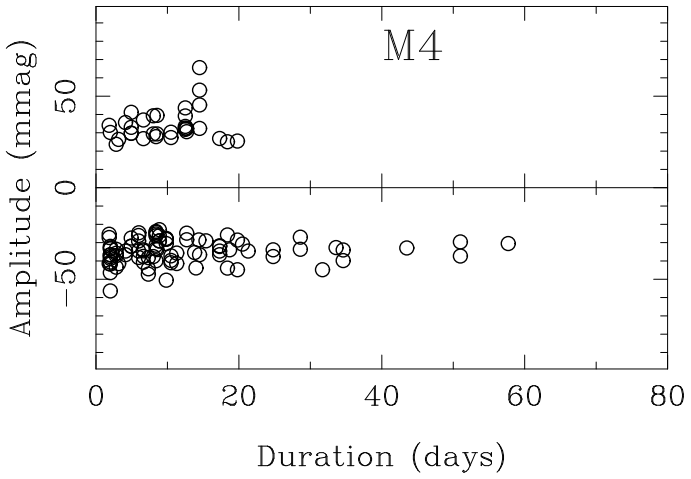

FIGURE 5.22: 'Peaks' from M4.

In a few words, the top-hat structures are more local and free from assumptions than the events.

The 'peaks' from M2 (Fig. 5.20) are not so numerous as the top-hat fluctuations inferred from the first model (M1). Moreover, the new cloud of points (open circles) is more concentrated towards shorter durations. In fact, all 'peaks' have a timescale of ≤ 20 days. When one takes M3 (Fig. 5.21) and M4 (Fig. 5.22) the situation is also somewhat different. The probability of observing a 40-60 days top-hat fluctuation is now of about 5%, although most features are due to a small gap of about 50 days around day 1815 (see SR99 and Fig. 5.2). Finally, Figures 5.19 and 5.22 inform on the true ability of the IAC-80 telescope to detect microlensing fluctuations in an observational DLC free from gaps: *a 'peak' with a timescale > 40 days should be interpreted as a feature related to microlensing or other mechanisms different to the observational noise, while as mainly caused by the poor resolution at the expected amplitudes within the interval [- 50 mmag, + 50 mmag], the ≤ 20 days microlensing 'peaks' cannot be resolved. Even in the unlikely case of very short-timescale microlensing signal with high amplitude, due to the smoothing by both the re-reduction and the binning as well as the current uncertainty of one week in the true time delay, it would be not possible to reliably reconstruct the microlensing 'peaks'.*

5.5 Conclusions

Several $\sim$ 1m class telescopes around the world are at present involved in different optical monitoring programs of quasars with the goal to detect microlensing. There are at least two 'modest' telescopes searching for microlensing signal related to a far elliptical galaxy (which is responsible, in part, for the gravitational mirage Q0957+561). The data taken at Whipple Observatory 1.2 m telescope and at Teide Observatory IAC-80 telescope together with the photometry from a 3.5 m telescope (at Apache Point Observatory) represent a great effort in order to obtain an accurate time delay in Q0957+561, follow the long-timescale microlensing event in that system and find some evidence in favour of very rapid and rapid microlensing (Kundić et al. 1995, 1997; Oscoz et al. 1996, 1997; Pijpers 1997; Schild & Thomson 1997; SR99; S96; Pelt et al. 1998; SW98; G98).

With respect to the very rapid (events with a timescale ≤ 3 weeks) and rapid (events with a duration of 1-4 months) microlensing, the previous results (before this work) are puzzling. The combined photometries (CLCs) from data taken at Whipple Observatory only can be well explained in the context of a picture including intrinsic variability, observational noise and microlensing variability on different timescales: from days to months (e.g., S96). The long-timescale microlensing does not play any role in a CLC. In particular, S96 reported on the existence of a network of rapid events with a few months timescale and an amplitude of about $\pm$ 50 mmag (these features found by Schild are called Schild-events). However, SW98 concluded that a picture with intrinsic signal and observational noise (without any need to introduce very rapid and rapid microlensing) is consistent with the observations at Apache Point Observatory. SW98 really show a difference lightcurve in global agreement with the zero line, but some doubt remains on the ability of the observational noise for producing the negative and positive measured events around 'peaks' (a 'peak' is constituted by a set of two or more consecutive deviations which have equal sign and are not consistent with zero). In any case, SW98 observed no Schild-events.

In this work, motivated by the mentioned intriguing results on microlensing variability, we analyzed the data from our initial monitoring program with the IAC-80 telescope (see SR99). We focused on the possible presence of rapid microlensing events in the lightcurves of Q0957+561

and the sensitivity of the telescope (using typical observational and analysis procedures) to microlensing 'peaks'. Our conclusions are:

1. Using photometric data (in the R band) for the 1996-1998 seasons, we made two difference lightcurves (DLCs). The total difference signal, which is based on ~ 1 year of overlap between the time-shifted lightcurve for the A component and the magnitude-shifted lightcurve for the B component, is in apparent agreement with the absence of microlensing signal. We can reject the existence (in our DLCs) of events with quarter-year timescale and an amplitude of $\pm$ 50 mmag, and therefore, Schild-events cannot occur almost continuously. On the contrary, they must be either rare phenomena (originated by microlensing or another physical process) or, because two observatories (Apache Point Observatory and Teide Observatory) found no Schild-events, artificial fluctuations associated with the observational procedure and/or the reduction of data at Whipple Observatory.

2. From a very conservative point of view, in our data, the amplitude of any hypothetical microlensing signal should be in the interval [- 50 mmag, + 50 mmag]. The rms averages of the DLCs (global variability) are of about 22 mmag (1996/1997 seasons) and 15 mmag (1997/1998 seasons), and reasonable constraints on the possible microlensing variability lead to interesting information on the granularity of the dark matter in the main lensing galaxy (a cD elliptical galaxy) and the size of the source (QSO). Thus the set of bounds derived from 1995-1998 seasons (SW98 and this work) rules out an important population of MACHOs with substellar mass for a small quasar size (Schmidt 1999).

3. In order to settle any doubt on the ability of the observational noise for generating the global (rms averages) and local (events and other less prominent features) properties of the DLCs, we have also carried out several experiments as 'Devil's advocates'. The measured variability (the rms value, a very rapid event and some minor deviations) in the DLC for 1996/1997 seasons can be caused, in a natural way, by the observational noise process. In the absence of microlensing signal, we proposed two different models (M1 and M2; see subsection 3.1) whose associated photometries (simulations) are consistent with the observations. In addition, the DLC for 1997/1998 seasons is a quasi-featureless trend with relatively small rms average. To explain the variability in our second observational DLC, we again showed that microlensing is not necessary. Two new models (M3 and M4; see subsection 3.2) only including the reconstruction of the intrinsic signal (assumed as a polynomial or a correlated stationary process) and a Gaussian observational noise process, led to simulated DLCs in agreement with the measured behaviour.

4. We finally show that from a typical monitoring with our telescope (observing times, method of analysis, etc.) is not possible to resolve microlensing 'peaks' with $\leq$ 20 days. The confusion with noise does not permit the separation between true microlensing features and 'peaks' due to the observational noise. However, all hypothetical 'peaks' with a timescale $>$ 40 days must be interpreted as phenomena which are not associated with the observational noise (e.g., microlensing fluctuations). At intermediate timescales (of about one month) the situation is somewhat intricate. Given a measured DLC, the probability of observing one noise 'peak' (with a duration of about 30 days) is less than 10%. Therefore, if we search

for microlensing signal and find an ‘intermediate peak’, the relative probabilities that the fluctuation is a noise feature or a microlensing ‘peak’ are $< 1{:}10$.

The same procedure used in this work was applied by David Alcalde (Alcalde, 2002) to the next two campaigns (1998-2000) from the same telescope, arriving to the same conclusions as described here. Recently, Colley et al. (2003) found that many rapid fluctuations in this system might be due to seeing effects, in well agreement with our noisy processes.

Since the microlensing study is done after correcting for the time delay between the components, a wrong estimate of the delay can originate erroneous microlensing conclusions. Goicoechea (2003) has suggested that multiple time delays could be the solution to the discrepancy between different time delay estimates (425 vs. 417 days). This suggestion is based on Yonehara’s idea (Yonehara 1999) that the variability from the quasar accretion disk takes place at different positions of the disk, introducing an additional delay. Ovaldsen et al. (2003) also found evidences in this direction. This issue is very important in order to extract information from the difference light curve regarding microlensing.

Chapter 6

Microlensing Simulations: limits on the transverse velocity in the quadruple quasar Q2237+0305⋆

Link. *Apart from Monte Carlo simulations seen in the previous Chapter, microlensing studies can also be carried out by means of ray-shooting simulations. The method is quite powerful: the microlensing fluctuations are statistically reproduced and tracks in these maps can be translated into physical lightcurves. Again, one can statistically asign probabilities to a certain fluctuation to be produced by a microlens. If microlensing fluctuations cannot be found in a given system when expected, this can also be translated into some physical information. In this Chapter we refine this procedure and apply it in a not previously used manner.*

Abstract. We determine upper limits on the transverse velocity of the lensing galaxy in the quadruple system Q2237+0305, based on four months of high quality monitoring data. By comparing the very flat lightcurves of components B and D with extensive numerical simulations, we make use of the absence of microlensing in these two components to infer that a period of that length is only compatible with an effective transverse velocity of the lensing galaxy of $v_{\rm bulk} \leq 570$ km/s for microlenses masses of $M_{\mu{\rm lens}} = 0.1 M_{\odot}$ (or $v_{\rm bulk} \leq 2000$ km/s for microlenses masses of $M_{\mu{\rm lens}} = 1.0 M_{\odot}$).

⋆Chapter based on the refereed publication Gil-Merino, Wambsganss, Goicoechea & Lewis, 2002, A&A, submitted

6.1 Introduction

Measurements of the peculiar motions of galaxies can provide strong constraints on the nature of dark matter and the formation and evolution of structure in the Universe. However, determining such 'departures from the Hubble flow', utilizing standard distance indicators as the Tully-Fisher relation for spirals and the $D_n - \sigma$ method for ellipticals (e.g., Peebles 1993), have proved to be quite difficult. While these methods provide radial peculiar motions, transverse peculiar motions are also required to fully constrain cosmological models. However, the determination of transverse velocities is an extremely difficult task, generally beyond the reach of current technology. Recently, Peebles et al. (2001) suggested the use of the space missions SIM and GAIA to estimate the transverse displacements of nearby galaxies. Roukema and Bajtlik (1999) claimed that transverse galaxy velocities could be inferred from multiple topological images, under the hypothesis that the 'size' of the Universe is smaller than the apparently 'observable sphere'. In spite of these efforts, the transverse motions of galaxies are currently unknown.

Dekel et al. (1990) showed that the local galaxy velocity field can be reconstructed assuming that this field is irrotational, and thus, the measurement of the transverse velocities could be used to test this assumption. In fact the determination of transverse motions would be very useful to discuss the quality of the whole reconstruction. From another point of view, the reconstruction methods are powerful tools to estimate galactic transverse motions.

Grieger, Kayser and Refsdal (1986) also suggested using gravitational microlensing of distant quasars to determine the transverse velocity of the lensing galaxy via the detection of a 'microlens parallax' as the quasar is magnified during a caustic crossing (see also Gould 1995). The determination of this parallax, however, requires not only ground-based monitoring, but also parallel measurements from a satellite located at several AU.

The gravitational lens Q2237+0305 consists of four images of a $z_q = 1.695$ quasar lensed by a low redshift $z_g = 0.039$ spiral galaxy (Huchra et al. 1985). Photometric monitoring revealed uncorrelated variability between the various images, interpreted as being due to gravitational microlensing (Irwin et al. 1989). This interpretation was confirmed with dedicated monitoring programs (e.g., Østensen et al. 1996; Woźniak et al. 2000a,b; Alcalde et al. 2002). Q2237+0305 is the best studied quasar microlensing system. Using ten years of monitoring data, Wyithe et al. (1999) recently used the derivatives of the observed microlensing lightcurves to put limits on the lens galaxy tranverse velocity of Q2237+0305.

Here in this contribution, we also determine upper limits on the transverse velocity of the lensing galaxy G2237+0305 using a different method, based on a comparison between about four months of high quality photometric monitoring of the four quasar images and intense numerical simulations. The details of the simulations are discussed in Section 6.2. In Section 6.3 we briefly present and review the lens monitoring results, discuss the variability of the two faintest components, and outline our method to obtain limits on the transverse velocity. The results of this approach – the constraints on the transverse velocity of the lensing galaxy – are presented in Section 6.4 and discussed in sections 6.6 and 6.5.

6.2 Microlensing simulations background

6.2.1 Lens models of Q2237+0305

Several approaches have been employed in modeling the observed image configuration in the system Q2237+0305 (Schneider et al. 1988, Wambsganss and Paczyński 1994, Chae et al. 1998, Schmidt et al. 1998). These models provide the parameters relevant to microlensing studies: the surface mass density, Σ, and the shear, γ, at the positions of the different images. The former represents the mass distribution along the light paths projected into the lens plane, while the latter represents the anisotropic contribution of the matter outside the beams. We can normalize the surface mass density with the critical surface mass density (see Section 2.2.1 and Schneider et al. 1992 for more details),

$$\Sigma_{\rm crit} = \frac{c^2}{4\pi G}\frac{D_s}{D_d D_{ds}} \tag{6.1}$$

where D_s, D_d and D_{ds} are the angular diameter distances between observer and source, observer and deflector and between deflector and source, respectively, c is the velocity of light and G is the gravitational constant. The resulting normalized surface mass density (also called *convergence* or *optical depth*) is expressed as $\kappa = \Sigma/\Sigma_{\rm crit}$.

We use here two different sets of values for κ and γ for the four components (Tab. 6.1), corresponding to the Schneider et al. (1988) and the Schmidt et al. (1998) lens models, respectively. We will demonstrate using these two sets that slightly different values for the two local lensing parameters do not change the results, and hence that some uncertainty in κ and γ of the images does not affect the conclusions.

	Schneider et al. (1988)		Schmidt et al. (1998)	
Image	κ	γ	κ	γ
A	0.36	0.44	0.36	0.40
B	0.45	0.28	0.36	0.42
C	0.88	0.55	0.69	0.71
D	0.61	0.66	0.59	0.61

Table 6.1: Two different sets of values for the surface mass density, κ, and the shear, γ, of the four images are used, in order to see the dependence of the result on the lens model (see References for details).

6.2.2 Simulations

We use the ray-shooting technique (see Wambsganss 1990, 1999) to produce the 2-dimensional magnification maps for each of the gravitationally lensed images. All the mass is assumed to be in compact objects – such as stars and planets – with no smoothly distributed matter (this assumption is valid since the images are projected to the inner part of the lens galaxy, where stars is the dominant matter component). All of the microlensing objects are assumed to have a mass of $M_{\mu\rm lens}$ and are distributed randomly over the lens plane. Taking into account the effect of the

shear and the combined deflection of all microlenses, light rays are traced from the observer to the source. This results in a non-uniform density of rays distributed over the source plane. The density of rays at a point is proportional to the microlensing magnification of a source at that position; hence the result of the rayshooting technique is a map of the microlensing magnification as a function of position in the source plane. The relevant scale factor, the Einstein radius in the source plane, is defined as

$$r_E = \left(\frac{4GM_{\mu\mathrm{lens}}}{c^2} \frac{D_s D_{ds}}{D_d} \right)^{1/2} . \tag{6.2}$$

Finally, the magnification pattern is convolved with a particular source profile. Linear trajectories across this convolved map, therefore, result in microlensing light curves (see also Schmidt and Wambsganss 1998).

In general, the details of a quasar microlensing light curve depend on several unknown parameters: the masses and positions of the microlenses and the size, profile and effective transverse velocity of the source. For this reason, the comparison of the simulated microlensing lightcurves to the observed ones cannot be done individually, but rather in a statistical sense.

6.3 The Method

6.3.1 The idea in a nutshell

Before going into details of the method we use, we present a very simple hypothetical scenario to better illustrate the procedure. Generally, microlensing magnification maps possess significant structure, in particular they consist of an intricate net of very high magnification regions, the caustics . The density and the length of the caustics vary with the values of surface mass density κ and shear γ. However, for a given pair of parameters κ and γ, there is something like a *typical* distance between adjacent caustics, though with quite a large dispersion. For illustration purposes, we assume now that we have a magnification pattern with caustics that are equally spaced horizontal and vertical lines (see, e.g., Fig. 6.1). Though this is far from being a realistic magnification pattern, its simplicity allows us to explain the relation between fluctuations in the microlensing lightcurves and the velocity of the source in simple terms. The pattern shows schematically the typical low (dark) and high (white) magnification areas. The length and width of the low magnification areas is exactly one unit length, l_{unit}. If we compute the magnification along a linear track *inside* one of this regions, the resultant lightcurve will be flat. However, there is a maximum length for such flat lightcurves: there cannot be any flat lightcurves with length larger than $l_{\mathrm{max}} = \sqrt{2}\, l_{\mathrm{unit}}$. Now suppose that this magnification map corresponds to a certain hypothetical gravitationally lensed system and we have a flat observed microlensing lightcurve corresponding to an observing period of t_{obs}. Then we can calculate an upper limit for the velocity of the source: $V_{\mathrm{max}} = \sqrt{2} l_{\mathrm{unit}} / t_{\mathrm{obs}}$. As stated above, true microlensing magnification maps are much more complex than the idealized case presented in Figure 6.1. But, nevertheless we can determine an upper limit on the track lengths in any magnification pattern in a statistical sense, by just replacing the ***fixed*** distance between caustics by the realistic distribution of caustic distances: this way we can get an upper limit on the track lengths (in r_E) that are consistent with the observed variability. This upper limit on the track length is labelled l_{upper}. Since we know the duration of the observing period t_{obs} from the actual monitoring campaign, it is straightforward to obtain the upper limit on the transverse velocity

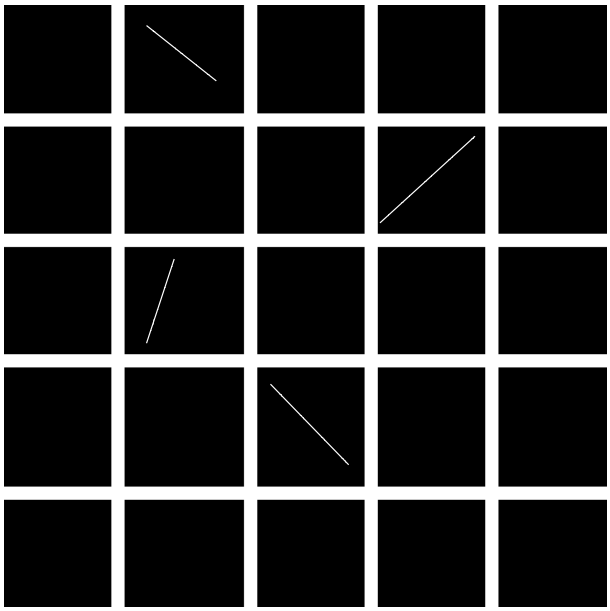

FIGURE 6.1: Idealized magnification pattern to illustrate the idea of the method: Black areas are low magnification zones, the regular grid of thick white lines represent the caustics (high magnification areas) and the thin white lines are example tracks due to the effective transverse motion of the source which result in *flat* lightcurves.

for assumed values of the lens mass $M_{\mu\mathrm{lens}}$ and the source size/profile: $V_{\mathrm{upper}} = l_{\mathrm{upper}}/t_{obs}$.

Although the effective transverse velocity has contributions from all three components source, lens, and observer as shown below, for the system Q2237+0305, the effective transverse velocity is dominated by the effective transverse velocity of the lensing galaxy.

6.3.2 Monitoring Observations of Q2237+0305 to be compared with

This study employs the results of the GLITP (Gravitational Lenses International Time Project) collaboration which monitored Q2237+0305 from October 1st, 1999 to February 3rd, 2000, using the 2.56 m Nordic Optical Telescope (NOT) at El Roque de los Muchachos Observatory, Canary Islands, Spain (see Alcalde et al. 2002 for data reduction details and results).

The R band photometry employed here is shown in Fig. 6.2. It is clear that whereas components A and C show a relatively significant variability (see Shalyapin et al. 2002 and Goicoechea et al. 2002 for the analysis of the brightest component A), images B and D remain relative flat, showing no signs of strong microlensing during the monitoring period. As the expected time delays between the images are short (≤ 1 day), intrinsic fluctuations would show up in all 4 images almost simultaneously and microlensing fluctuations are relatively easy to distinguish. Keeping in mind the idea expressed in the previous subsection, we used the flatness of these two components to statistically infer upper limits on the length of linear tracks in the corresponding magnification patterns.

For a given component (we here consider B and D), the largest fluctuation in the lightcurve is given by the difference between the maximum and the minimum magnitudes. Thus $\Delta m_X = m_{X,\mathrm{max}} - m_{X,\mathrm{min}}$, where X denotes component B or D. For the simulated microlensing lightcurves

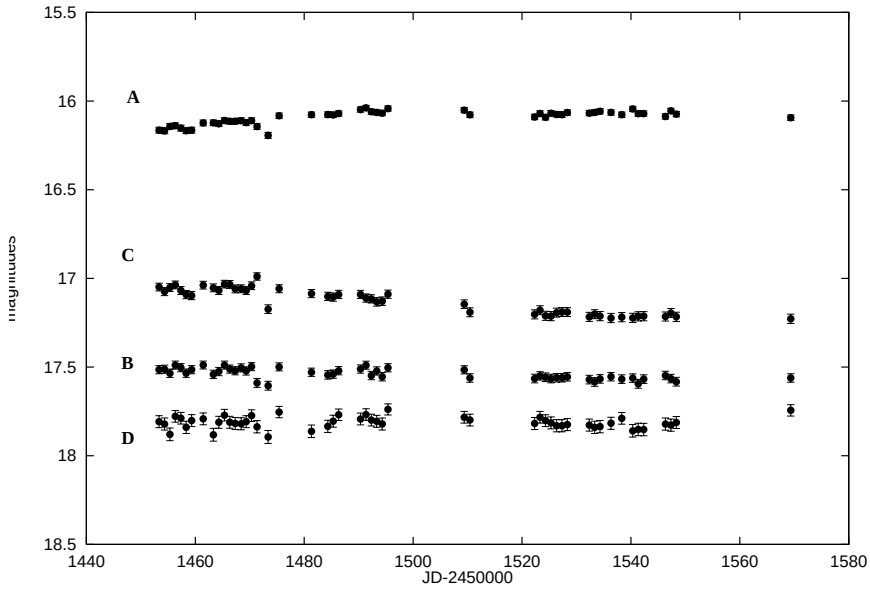

FIGURE 6.2: The R band photometry of Q2237+0305 from the GLITP collaboration. The observing period was from October 1st, 1999 (JD 2459452) to February 3th, 2000 (JD 2459577) with the Nordic Optical Telescope at Canary Islands, Spain (details in Alcalde et al. 2002). The components are labeled from A to D (Yee 1988).

the condition to be fulfilled then is: $\Delta m_X(simul) \leq \Delta m_X$, where $\Delta m_X(simul)$ is the difference between the maximum and the minimum in the simulated lightcurve (again X is component B or D). For component B we obtained $\Delta m_B = 0.116$ mag and for component D, $\Delta m_D = 0.155$ mag (see Fig. 6.3).

6.3.3 Microlensing Simulations

We computed magnification patterns for quasar images B and D, using the Schmidt et al. (1998) model for the values of κ and γ (cf. Table 1). We assumed all compact objects have the same mass, $M_{\mu\mathrm{lens}}$. The physical sizes lengths of these maps were $15\ r_E$ covered by 4500 pixels, resulting in a spatial resolution of 300 pixels per Einstein radius r_E. The effect of the finite source size is included by convolving the magnification patterns with a certain source profile. We adopted a Gaussian surface brightness profile for the quasar. The source size is defined by the Gaussian width σ_Q. We used three different values of σ_Q= $0.003\ r_E$, $0.01\ r_E$ and $0.05\ r_E$. This corresponds to 'physical' sizes from 2×10^{14} cm to 3×10^{15} cm for $M_{\mu\mathrm{lens}} = 0.1 M_\odot$, and a factor of $\sqrt{10}$ larger for lens masses of $M_{\mu\mathrm{lens}} = 1.0 M_\odot$ (range of sizes favoured by various authors: e.g. Wambsganss et al. 1990, Wyithe et al. 2000b).

In Fig. 6.4 we show a portion of one of these magnification patterns (for component D): the side length is $4\ r_E$, and it was convolved with a gaussian profile of $\sigma_Q = 0.01\ r_E$. White color indicates high magnification while black means low magnification. The linear track drawn inside Fig. 6.4 illustrates the calculation procedure: we start at a random position and with a random direction. This is indicated by an arrow at the beginning of the white line at the top. We determine the magnification along the track and construct in this way a lightcurve point by point. When $\Delta m_D(simul)$

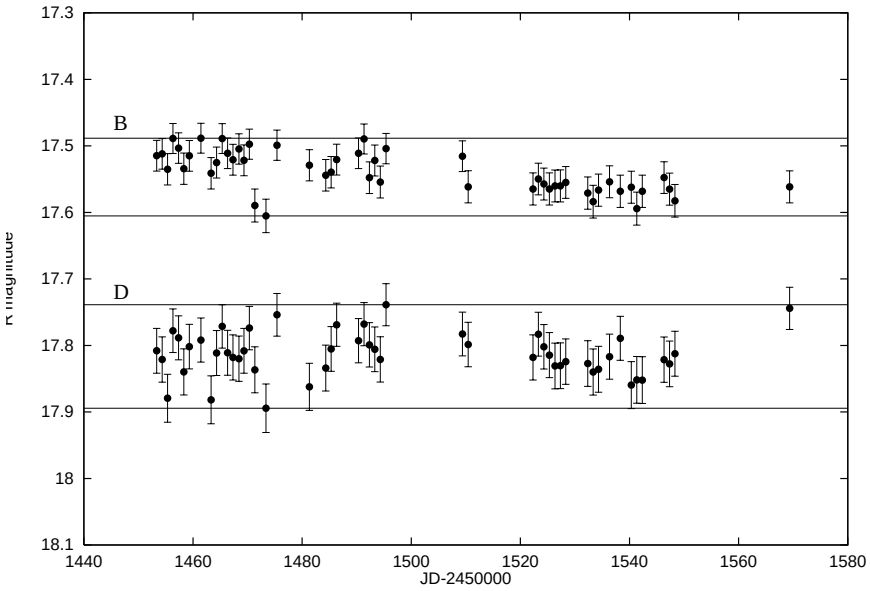

FIGURE 6.3: R band lightcurves of images Q2237+0305 B and D on an expanded scale, with the bands defined by the the maximum and the minimum in each component. The widths of these bands are $\Delta m_B = 0.116$ mag and $\Delta m_D = 0.155$ mag.

– the amplitude between maximum and minimum of the so far constructed lightcurve – gets larger than Δm_D the construction of this particular light curve is stopped, and the length of the track, l, is determined. This corresponds to the white part in Fig. 6.4.

In order to statistically infer an upper limit on the permitted length of the linear tracks across the magnification maps we do the following (for a given source size): we randomly select a starting pixel in the magnification pattern of one of the images, let us assume it is component B. Then we also select a random direction for which the magnification along a linear track is going to be computed.

As the next step, a random starting point in the magnification pattern of the other image D is selected. However, this time the direction is not arbitrary: The direction of motion in the two images relative to the external shear is fixed, the displacements of the source in the magnification maps B and D are no longer independent. In fact, because of the cross-like geometrical configuration of the system, they are orthogonal to each other (see Fig. 6.5 motivated by Kent & Falco, 1988; Witt and Mao, 1994; Schmidt et al., 1998). Thus, once the direction in the magnification pattern B is selected, the one in the magnification pattern D is determined as well. So in this way we construct simultanously the lightcurves for quasar images B and D point by point along linear tracks.

When either $\Delta m_B(simul)$ or $\Delta m_D(simul)$ – the amplitudes between maximum and minimum of the so far constructed lightcurves for images B and D – are larger than Δm_B or Δm_D, respectively, then the construction of this particular pair of lightcurves is stopped, and the length of the two tracks, l, is determined. This corresponds to the white part in Fig. 6.4.

We did this for 10^5 pairs of tracks and stored these 10^5 values for the respective maximum lengths l. From this distribution we can now derive $l_{\rm upper}$ from the cumulative probability $P(l \leq l_{\rm upper})$ = 95%, i.e., the 95 per cent upper limit on the allowed path lengths. The whole procedure was repeated for magnification patterns constructed with the κ and γ values of the Schneider et al.

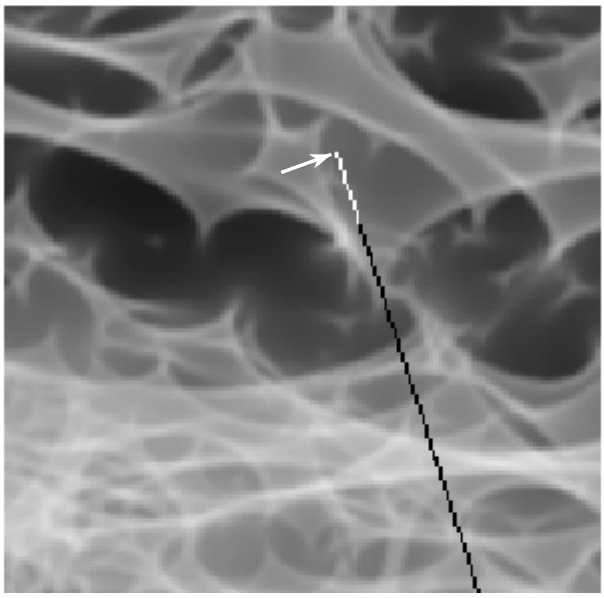

FIGURE 6.4: A small part of the total magnification pattern for component D, convolved with a gaussian profile with $\sigma_Q = 0.01\ r_E$. The sidelength is $4\ r_E$. The length of the track is determined in such a way as to fulfill the criterion $\Delta m_D(simul) > \Delta m_D$, which corresponds to the white part (the beginning of the track is indicated by the arrow.

(1988) model, see Table 1. The results were indistinguishable.

6.4 Results

The resulting cumulative probability distributions for the various simulations are shown in Fig. 6.6. These lines represent the integrated probabilities for certain track lengths in units of Einstein radii. The three curves represent the three different source sizes we considered: $\sigma_Q = 0.003\ r_E$ (thin line), $\sigma_Q = 0.01\ r_E$ (medium line) and $\sigma_Q = 0.05\ r_E$ (thick line).

From each distribution we can determine the upper limit on the length of the tracks consistent with the variability of the observed lightcurves defined by the bands described before. The three limits are (95% confidence limit):

$$l_{\rm upper} = 0.11\ r_E \ \text{ for } \ \sigma_Q = 0.003\ r_E,$$

$$l_{\rm upper} = 0.12\ r_E \ \text{ for } \ \sigma_Q = 0.01\ r_E,$$

and

$$l_{\rm upper} = 0.12\ r_E \ \text{ for } \ \sigma_Q = 0.05\ r_E.$$

We can also estimate an error for these numbers from the $\sqrt{N}$ – it is a Poissonian process, as the photon statistics in CCDs – , where N is the number of simulations at the 95% point. The error is $\pm 0.02\ r_E$. So within this error estimation, the results are compatible being the same for the

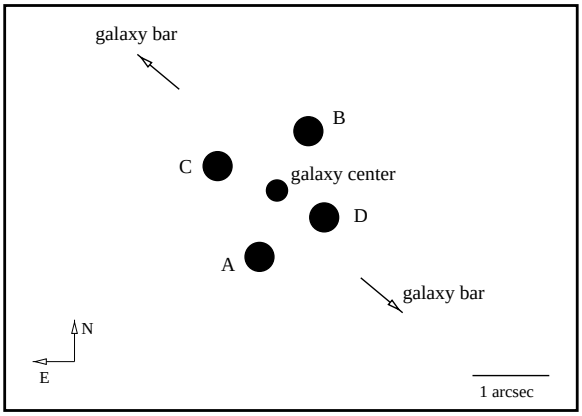

FIGURE 6.5: Relative positions of the quasar images, galaxy centre and galaxy bar. The direction of motion relative to the external shear is not independent between the images because of the cross-like geometrical configuration. This is orthogonal between images A⊥C and B⊥D.

three source sizes considered. These numbers can be converted into physical quantities by using Eq. 6.2 and a given value for the mass of the microlenses, $M_{\mu\rm lens}$. As we are observing the inner part of the lens galaxy, a resonable range for the microlenses mass is $0.1M_{\odot} \leq M_{\mu\rm lens} \leq 1M_{\odot}$ (Alcock et al. 1997, Lewis & Irwin 1995, Wyithe et al. 2000a). Using the observing period time, $t_{\rm obs} = 126$ days, we can then deduce $v_{\rm upper}$, the 95% limit on the effective tranverse velocity in this lens system.

In calculating the effective transverse velocity of the lens in the lens plane from these numbers, we need to use the following expression (Kayser et al. 1986):

$$\vec{V} = \frac{1}{1+z_s}\,\vec{v}_s - \frac{1}{1+z_d}\frac{D_s}{D_d}\,\vec{v}_d + \frac{1}{1+z_d}\frac{D_{ds}}{D_d}\,\vec{v}_{\rm obs}, \tag{6.3}$$

where $\vec{V}$ is the effective transverse velocity of the system, $\vec{v}_s$ the velocity of the source, $\vec{v}_d$ the velocity of the deflector (lens), and $\vec{v}_{\rm obs}$ the velocity of the observer. The effective transverse motion of the lens includes the true transverse velocity of the galaxy as a whole and an effective contribution due to the stellar proper motions. The adopted cosmology is $\Omega_o = 0.3$, $\Lambda_o = 0.7$ and $H_0 = 66$ km sec^{-1} Mpc^{-1}. and z_s, z_d are the redshifts of the source and deflector, respectively. Putting in the respective values in Eq. 6.3, we get:

$$V = 0.37\,v_s - 10.55\,v_d + 10.18\,v_{\rm obs}. \tag{6.4}$$

Comparison of the Earth's motion relative to the microwave background (Lineweaver et al. 1996) with the direction to the quasar Q2237+0305 indicate that these vectors are almost parallel, so that the last term in the right side of Eq. 6.4 can be neglected. Furthermore, assuming that the peculiar velocities of the quasar and the lensing galaxy, v_s and v_d, are of the same order, the first term can be neglected as well, since its weight is only about 4% of the total. In this way, we just keep the expression

$$V \;\simeq\; 10.55\,v_d. \tag{6.5}$$

An upper limit for the effective transverse velocity of the lens measured in the lens plane, v_d, can now be calculated by just setting $V = v_{\rm upper}$, where $v_{\rm upper}$ is the 95% limit on the effective

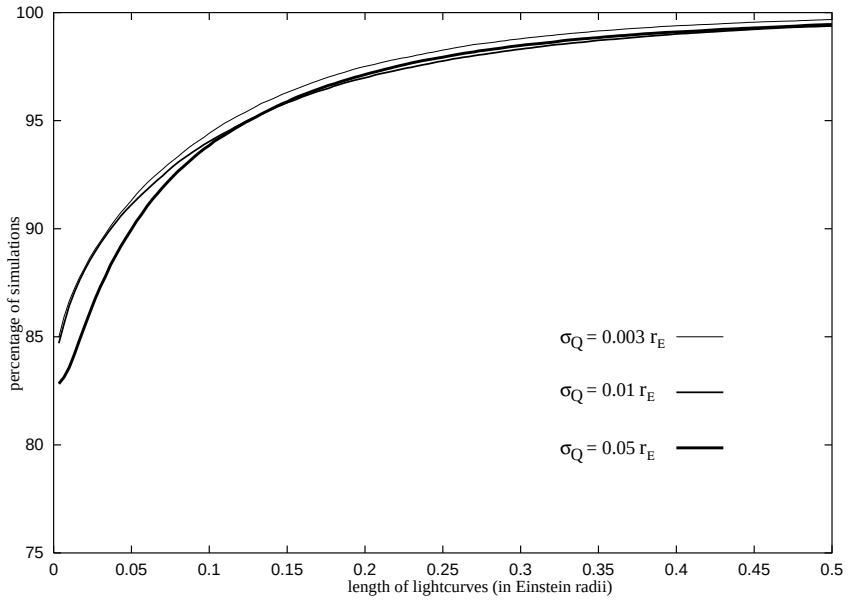

FIGURE 6.6: Cumulative probability distribution for the maximum lengths of the lightcurves determined by the criterion $\Delta m_B(simul) > \Delta m_B$ or $\Delta m_D(simul) > \Delta m_D$ for three different source sizes: $\sigma_Q = 0.003\, r_E$ (thin line), $\sigma_Q = 0.01\, r_E$ (medium line), and $\sigma_Q = 0.05\, r_E$ (thick line).

transverse velocity, as inferred from the simulations. The resulting value for the limit on the transverse velocity of the lensing galaxy obtained in this way depends on the assumed mass of the microlenses and on the quasar size. For $M_{\mu\mathrm{lens}} = 0.1 M_\odot$, the numbers are:

$$v_d = 580 \text{ km/s}$$

for the smallest source size, and

$$v_d = 633 \text{ km/s}$$

for the two larger sources sizes. The limits for masses of $M_{\mu\mathrm{lens}} = 1.0 M_\odot$ are

$$v_d = 1840 \text{ km/s} \text{ and } v_d = 2005 \text{ km/s} \text{ respectively.}$$

The results are summarized in Tab. 6.2.

source size (r_E)	l_{upper} (r_E)	$M = 1 M_\odot$	$M = 0.1 M_\odot$
0.003	0.11	1840 km/s	580 km/s
0.010	0.12	2005 km/s	633 km/s
0.050	0.12	2005 km/s	633 km/s

Table 6.2: The limiting transverse velocity v_d of the lens galaxy for three different source sizes. To convert the length of the tracks in r_E into physical units, we need the mass of the microlenses. We use $M_{\mu\mathrm{lens}} = 1 M_\odot$ and $M_{rm\mu lens} = 0.1 M_\odot$. The error estimation for l_{upper} is $\pm 0.02\, r_E$.

It is even possible to place slightly stronger limits on v_{bulk}. The reason is that the actual effective lens velocity v_d is a combination of the bulk velocity of the galaxy as a whole (v_{bulk}) and the

source size (r_E)	$l_{\rm upper}$ (r_E)	$M = 1M_\odot$	$M = 0.1M_\odot$
0.003	0.11	1817 km/s	508 km/s
0.010	0.12	1985 km/s	568 km/s
0.050	0.12	1985 km/s	568 km/s

Table 6.3: Same as Tab. 6.2 but using Eq. 6.6 to infer slightly stronger limits on the effective transverse velocity $v_{\rm bulk}$ of the lens galaxy. The error estimation for $l_{\rm upper}$ is $\pm 0.02\ r_E$.

velocity dispersion of the microlenses ($v_{\mu\rm lens}$). This latter effect was studied by Schramm et al. (1992), Wambsganss & Kundic (1993) and Kundić & Wambsganss (1995), and it was found that the two velocity contributions combined are producing the effective velocity in the following way:

$$v_d = \sqrt{{v_{bulk}}^2 + (a\ v_{\mu lens})^2} \tag{6.6}$$

where a represents the *effectiveness* of microlensing produced by the velocity dispersion of the stars versus the one caused by the galaxy bulk motion. The value of this '*effectiveness parameter*' is $a \approx 1.3$ (see Wambsganss & Kundic 1993, Kundić & Wambsganss 1995 for details). Since the velocity dispersion of the lensing galaxy in Q2237+0305 has been measured to be $v_{\mu\rm lens} \simeq 215$ km/s (Foltz et al. 1992), we can use that and infer an even lower value for the limit on the effective velocity of the bulk motion (using the largest source size):

$$v_{\rm bulk} \simeq 568\,{\rm km/s}\ \text{ for }\ M_{\mu\rm lens} = 0.1M_\odot,\ \text{ and}$$

$$v_{\rm bulk} \simeq 1985\,{\rm km/s}\ \text{ for }\ M_{\mu\rm lens} = 1.0M_\odot.$$

In Tab. 6.3 the resulting values from applying Eq. 6.6 for all the source sizes are shown.

6.5 Discussion

Wyithe et al. (1999) presented the first contribution for determining the effective transverse velocity of the lens galaxy in Q2237+0305 via microlensing. Here we compare this approach to ours. First, as the Wyithe et al. method requires a number of microlensing events happening, they need a base monitoring line of the order of 10 years or so. Our method – based on the absence of microlensing fluctuations – can be applied to shorter monitoring base lines (typically one order of magnitude lower). Second, our statistics is simple and straighforward: fluctuations higher than the observations are ruled out in the simulations, no other assumptions are necessary. Wyithe et al. use the Kolmogorov-Smirnov statistic (and a modification of it), where the method has to accept or reject a previously adopted hypothesis. Third, the results in Wyithe et al. are slightly quasar size dependent, contrary to ours: this can be understood thinking that the source size plays a more important role when microlensing fluctuations are present (their method) but not during quite episodes (our method). Fourth, although the results obtained by Wyithe et al. are model dependent, their best case is a few per cent lower than our result and it is in very good agreement within our error estimations. Finally, it is important to notice that if outliers are present in the photometry, the result will be overestimated (the real limit for the transverse velocity will lower than the obtained result) and thus a precise data reduction procedure is needed. This seems to be true in both methods.

6.6 Conclusions

Estimating peculiar motions of galaxies is in general a difficult task. Here we have derived upper limits to the transverse velocity of the lensing galaxy in the quadruple quasar system Q2237+0305. Using four months of monitoring data from the GLITP collaboration (Alcalde et al. 2002), we took the limits from the lightcurves of components B and D, where no strong microlensing signals are present. The idea of the method is simple and straightforward: if the galaxy is moving through the network of microcaustics but no microlensing is present in the observations, this defines a typical length of the low magnification regions in the magnification patterns, which in turn can be easily converted into a physical velocity. This typical length is derived in a statistical sense from intensive numerical simulations using two different macro models for the lens (which both produce the same results). The resulting value obtained for this upper limit on the transverse velocity of the lensing galaxy is $v_{\rm bulk} < 570$ km/s for lens masses of $M = 0.1 M_{\odot}$ and $v_{\rm bulk} < 2000$ km/s for lens masses of $M = 1.0 M_{\odot}$. Within the error estimation for this limit, the result is independent of the quasar sizes considered. Future monitoring campaigns of this and other multiply imaged quasars can be used to provide more and stronger limits on the transverse velocities of lensing galaxies.

Part III

Galaxy Cluster Lensing and X-rays

Chapter 7

Weak lensing: the galaxy cluster Cl 0024+1654 from VLT-BVRIJK multiband photometry⋆

Link. *The study of clusters of galaxies is a powerful way to get information on the cosmological parameters. Mass and luminosity estimates of clusters help us to understand how dark matter is distributed in the Universe. Nevertheless, there are several ways of analysing galaxy clusters and not all the methods give the same results. In order to find an explanation to these discrepancies, a detailed description of the systems and their physical states are needed. Gravitational lensing allows us to obtain the total mass of a cluster independently of its dinamical state. In the last years the improvements in the lensing techniques and in the observational instruments make possible to get accurate mass distributions.*

Abstract. We present a mass reconstruction using weak lensing analysis of the cluster of galaxies CL0024+1654. We make use of a multiband BVRIJK photometry to get the photometric redshift of the background galaxies in the field. This breaks the degeneracy in the mass estimate. We compare the mass profile to the luminosity one and find that mass is well traced by light in a region of radius $\theta < 3$ arcminutes from the centre of the cluster. We obtain a mass of $M(\theta < 230 h_{65}^{-1}$ kpc$) = (0.98 \pm 0.11)\ 10^{14} h_{50}^{-1}\ M_{\odot}$ and a luminosity of $L = (0.48 \pm 0.04)\ 10^{12} h_{65}^{-2}\ L_{\odot}$. The mass-to-light ratio is $M/L_R = (200 \pm 2)\ M_{\odot}/L_{\odot}$ assuming a constant behaviour in the analysed region. Fitting a universal mass density profile to the data, we find a concentration parameter $c = 9.88^{+4.18}_{-2.22}$.

⋆A paper based on the results of this Chapter is in preparation

7.1 Introduction

Clusters of galaxies are the largest structures gravitationally bound we know of in the Universe. The analysis of such systems provides deep insides in understanding the nature and content of dark matter in the Universe, one of the key issues in cosmology. Thus, mass estimates of galaxy clusters deserve special attention.

Three independent methods are used to estimate the mass of clusters of galaxies: 1) the application of the virial theorem, which relates the galaxy velocity dispersion with the total mass of the cluster (Zwicky 1993, Smith 1936). Its limitations are the difficulty in measuring radial velocities for large samples of cluster members and the assumption of dinamical equilibrium, which can be broken by substructure or/and infalls (Merrit & Tremblay 1994). 2) From the X-ray emission of the intra-cluster hot gas, assuming spherical symmetry and hydrostatic equilibrium in the cluster, one can relate the density and temperature obtained from the intracluster gas spectrum with the cluster mass as a function of radius (Bahcall & Sarazin 1977). 3) By using the gravitational lensing theory. The gravitational lensing by cluster of galaxies can be divided in two regimes: strong and weak lensing. Giant lensed arcs and multiple images fall in the former regime, while little distorsions of background galaxies are the signature of the latter. The mass estimate through strong lensing features is associated with lens modeling and gives tight constrains on the mass (Soucail et al. 1987), although the method is only valid in the inner parts of the cluster defined by the multiple images. The complementary approach is the weak lensing mass estimates from the observed distortions of background galaxies (Kaiser & Squires 1993, Squires & Kaiser 1996). This method, with some recent improvements on the original (see also Section 3.2, is the one we use in this work and it is described in some detail in Sec. 7.4. Also in the context of gravitational lensing, the measured source depletion due to lens magnification can be used to estimate the mass of a galaxy cluster, as predicted by Broadhurst et al. (1995).

The galaxy cluster Cl 0024+1654 was discovered by Humason & Sandage (1957). It is one of the most interesting distant clusters of galaxies, with $z = 0.395$ (Gunn & Oke 1975), due to the gravitationally lensed features that it produces. Gravitational arcs in this system were firstly detected by Koo (1988) and then spectroscopically observed by Mellier et al. (1991). It is also a very rich cluster, with a high central concentration of bright galaxies and not dominated by a single cD galaxy. Dressler et al. (1985) obtained a velocity dispersion of (1300 ± 100) km s^{-1}, suggesting a very massive cluster of galaxies (Schneider et al. 1986). Böhringer et al. (2000) and Soucail et al. (2000) analised X-ray ROSAT observations of Cl 0024+1654, finding a mass discrepancy of a factor 1.5 to 3 lower with respect to the dinamical approach. Mass estimates from gravitational lensing by Kassiola et al. (1992), Smail et al. (1997), Tyson et al. (1998) and Broadhurst et al. (2000) using strong lensing models and by Smail et al. (1996) using weak shear estimates are in general a factor of 2-3 higher than the X-ray results. Recently, Ota et al. (2003) found a discrepancy between lensing mass estimate and X-rays of a factor of 3, using observations from the CHANDRA satellite. Czoske et al. (2002) proposed a collision scenario where a high speed encounter between two similar mass clusters would explain all these discrepances. Being this approach valid would imply that X-ray mass estimates are no longer possible without detailed hydrodynamic simulations. Furthermore, Kneib et al. (2003) in a wide-fiedl HST analysis, found significantly massive substructure at a distance of 1 Mpc, suggesting that the system might be not relaxed.

Filter	Exp. time [s]	Seeing [″]	Pixel Size [″]	F.O.V [″]
B	4800	0.54	0.2	6'.8×6'.8
V	4800	0.57	0.2	6'.8×6'.8
R	4800	0.48	0.2	6'.8×6'.8
I	4200	0.52	0.2	6'.8×6'.8
J	–	–	0.2	2'.5×2'.5
K	–	–	0.2	2'.5×2'.5

Table 7.1: VLT data of the galaxy cluster Cl 0024+1654. BVRI bands were obtained with the FORS camera and JK bands with the ISAAC camera. The field of view (FOV) of the two cameras is different, so the photometric redshifts can only be calculated for the galaxies in the common field of both cameras.

In this work we analyse multiband BVRIJK photometry of the galaxy cluster Cl 0024+1654. In Sec. 7.2 we present the observations and data set. In Sec. 7.3 we describe the cluster members distribution. Sec. 7.4 describes the mass estimates derived from the weak lensing signal whereas in Sec. 7.5 we fit this results to an universal density profile. In Sec. 7.6 we analyse the light distribution and compare to the distribution of the projected mass. Finally, in Sec. 7.7 we compare our results to previous ones and conclude.

Throughout this Chapter we use $H_0 = 65$ km s^{-1} Mpc^{-1}, $\Omega_M = 0.3$ and $\Omega_\Lambda = 0.7$. Using this cosmology, at the redshift of Cl 0024+1654, $1'$ corresponds to 230 kpc.

7.2 Data acquisition

The galaxy cluster Cl 0024+1654 was observed with the VLT at ESO. FORS2 camera was used to obtain the B, V, R and I bands with a field of view of 6'.8×6'.8. The J and K bands were obtained with the ISAAC camera and field of view of 2'.5×2'.5. The photometric calibrations and image stacking were done at the TERAPIX[1] data center. These data are presented in Tab. 7.1.

This multi-band photometry makes possible to obtain the photometric redshifts z_{phot} of the background galaxies in the common field of the different bands. The z_{phot} were computed using the fitting software *hiperz* (Bolzonella et al. 2000) by means of a comparison between the spectral energy distribution of galaxies inferred from our data set (BVRIJK bands) and spectral templates of galaxies with time-evolution correction models (a detailed explanation of this procedure can be found in Athreya et al. 2002). In general, z_{phot} errors obtained from the *hiperz* software were found to be $\Delta z_{phot} \sim 0.05$ at $z_{phot} \leq 1$ and $\Delta z_{phot} \sim [0.1\ (1 + z_{phot})]$ for larger redshifts. It is important to notice here the fact pointed out by Athreya et al. (2002) that using only BVRI photometry would introduce a much larger error in these estimates, due to the lack of strong spectral features in the wavelenghts covered by these filters. The distribution of galaxies versus photometric redshift is shown in Fig. 7.2.

[1] http://terapix.iap.fr

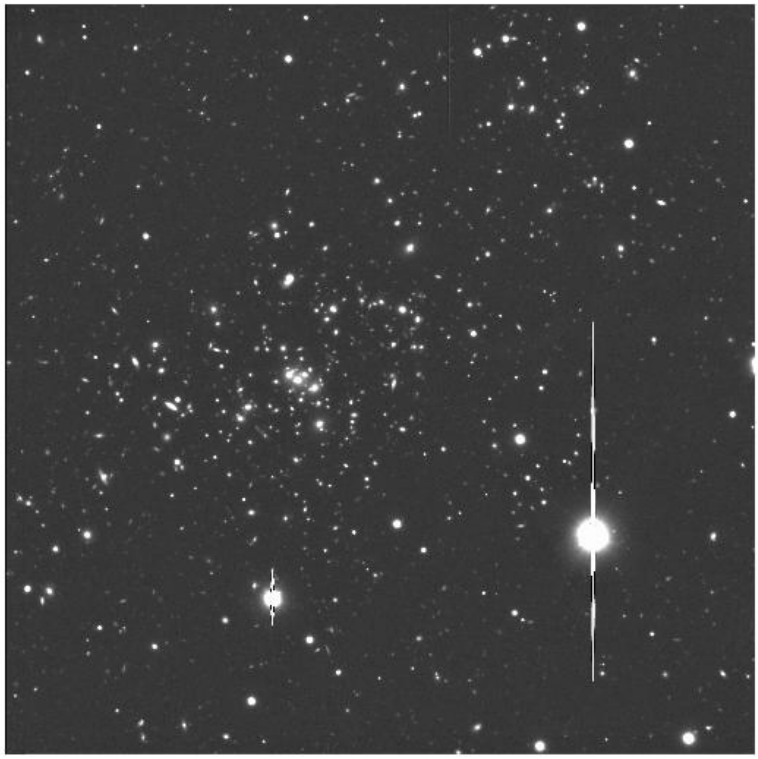

FIGURE 7.1: The galaxy cluster Cl 0024+1654 in the R band obtained with the FORS camera. The field of view is $6'.8 \times 6'.8$. North is up and East is left.

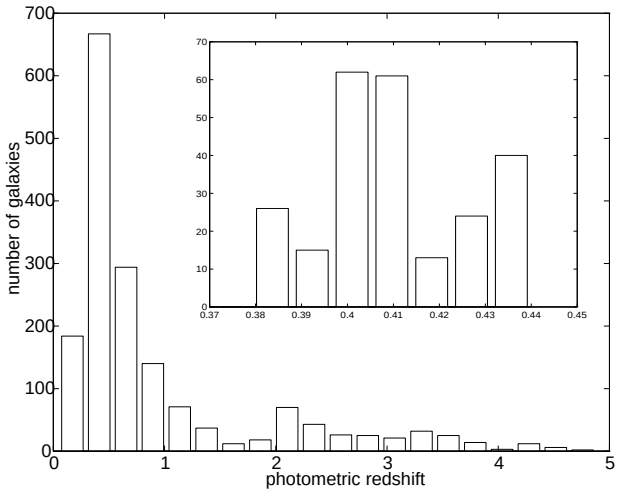

FIGURE 7.2: Distribution of galaxies with photometric redshift in Cl 0024+1654 field. The photometric redshifts were computed using *hiperz* software (see text for details) applied to the BVRIJK set of filters. The *inner pannel* is the same distribution only in the redshift interval [0.37 0.45]. We cannot confirm/reject a bimodal distribution of galaxies – as suggested by Czoske et al. (2002) – due to the error estimates in the photometric redshifts, too high for this comparison.

7.3 Distribution of cluster members

Czoske et al. (2002) proposed a collision scenario based on the bimodal distribution of the redshift histogram of the cluster members . They found a large peak centered at $z = 0.395$ ($0.387 < z < 0.402$), i.e., at the known cluster redshift, containing 237 galaxies and a secondary background peak centered at $z = 0.381$ ($0.374 < z < 0.387$) containing 46 cluster members. They interpreted this as two clusters of galaxies in a merging process.

We looked into our data in order to check this hipothesis. Due to the error estimates in the photometric redshifts, large for this purpose although precise enough for the weak lensing analysis, we cannot confirm/reject this issue. In Fig. 7.2 *inner pannel* we plot the distribution of galaxies in the redshift range [0.37 0.45]. No bimodal distribution is found.

The distribution of galaxies with respect to their R magnitude is shown in the *left pannel* of Fig. 7.3 and in the *right pannel* the same distribution only for cluster members. This illustrates the completeness of our sample. The sample is complete until R=25.5 magnitudes.

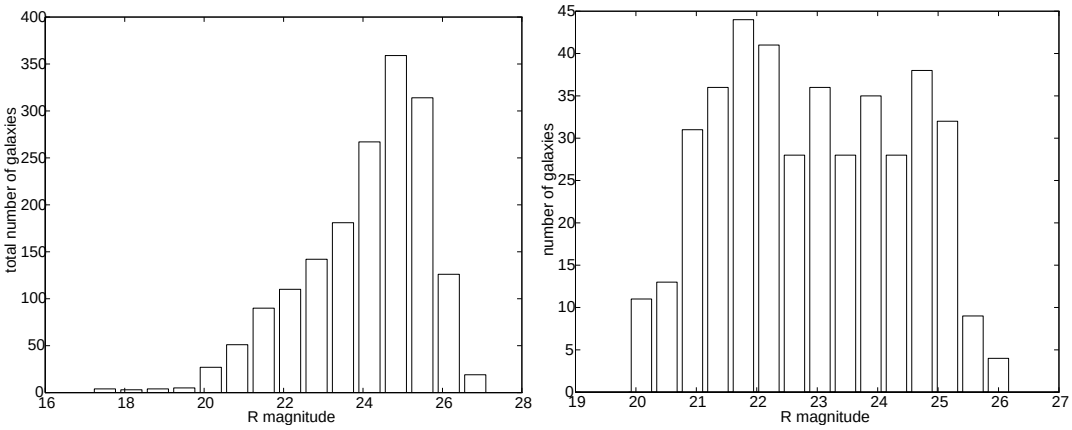

FIGURE 7.3: To illustrate the completeness of our sample: the *left pannel* is the distribution of the total number of galaxies in the field in the R band; the *right pannel* shows the histogram of cluster members against R magnitude. Our sample is complete until R=25.5 magnitudes.

7.4 Mass reconstruction from weak shear

The mass reconstruction method used here is the Aperture Mass Densitometry or ζ-statistics described by Kaiser & Squires (1993), Fahlman et al. (1994) and Squires & Kaiser (1996), with some modifications introduced by Hoekstra et al. (1998). We briefly describe the method here and refer the reader to those authors and references therein for further details.

The general idea of the method resides in two basic statements:

(a) that the surface mass density can be calculated inverting the integral expression for the shear (see e.g. Bartelmann & Schneider 2001)

$$\gamma(\theta) = \frac{1}{\pi} \int_{\Re^2} \mathcal{D}(\theta - \theta')\, \kappa(\theta')\, d^2\theta' \tag{7.1}$$

where the complex function $\mathcal{D}(\theta) = \frac{-1}{(\theta_1 - i\theta_2)^2}$ and θ_1 and θ_2 are the two components of the vector θ;

(b) that the shear can be approximated by the weak distortion in the background galaxies induced by the gravitational lensing potential of the cluster. Although this distortion is an observable, not all the distortion observed in the background galaxies is due to gravitational lensing: undesirable effects induced by the PSF ('smearing') and/or camara distorsions must be properly corrected.

Following Hoekstra et al. (1998), we first quantify the shapes of the selected background galaxies calculating the second moments I_{ij} of their fluxes and forming their 2-component polarization (Blandford et al. 1991)

$$e_1 = \frac{I_{11} - I_{22}}{I_{11} + I_{22}} \qquad \text{and} \qquad e_2 = \frac{2I_{12}}{I_{11} + I_{22}}. \tag{7.2}$$

The PSF smearing or smear polarizability P^{sm} will change the shape of the objects and must be corrected. It has two opposite effects. One comes from the anisotropy of the PSF, which introduces a systematic polarization of the galaxies. The other one is the convolution of the PSF with the seeing that tends to circularize the objects. The PSF can be estimated from the field stars in the images, fitting a second order polynomial over the field and interpolating at the position of the galaxies. After these corrections, the new galaxy polarization will be

$$e_\alpha \;\rightarrow\; e_\alpha - \sum_\beta \frac{P^{sm}_{\alpha\beta}}{P^{sm*}_{\alpha\beta}} e^*_\beta \tag{7.3}$$

where asteriks denote measurements from the stars.

Since the seeing circularizes the shape of the objects, it is important to take this effect into account as well. In this way we will be able to have a 'preseeing' shear polarizability P^γ, i.e. the shear polarizability before 'suffering' the seeing effect (Luppino & Kaiser 1997)

$$P^\gamma = P^{sh} - \frac{P^{sh}_*}{P^{sm}_*} P^{sm} \tag{7.4}$$

where P^{sh} denotes 'postseeing' shear polarizability which can be directly calculated from the observations and asteriks denote again measurements from the stars.

Finally, the distortion at a certain position in the image due to gravitational lensing is

$$g_\alpha = \frac{\langle\, e_\alpha \rangle}{\langle P^\gamma_{\alpha\alpha} \rangle}. \tag{7.5}$$

Working in the weak lensing regime (when $\kappa \ll 1$) we can write $\langle\gamma\rangle \approx \langle g\rangle$ (see e.g. Kaiser & Squires 1993, Mellier 1999), the surface mass density can be expressed as (the so-called ζ-statistics)

$$\zeta(\theta_1, \theta_2) = \kappa(\leq \theta_1) - \kappa(\theta_1 \leq \theta \leq \theta_2) = \frac{2}{1 - (\theta_1/\theta_2)^2} \int_{\theta_1}^{\theta_2} \langle \gamma_t(\theta) \rangle \, d(ln\theta) \tag{7.6}$$

and the mass within a certain aperture is given by

$$M(\leq \theta_i) = \kappa(\leq \theta_i)\, \Sigma_{crit}\, \pi\, (\theta_i D_{ol})^2 \tag{7.7}$$

where Σ_{crit} is the critical surface mass density and D_{ol} is the angular distance between the observer and the lens. Also the critical surface mass density can be expressed in terms of the angular distances:

$$\Sigma_{crit} = \frac{c^2}{4\,\pi\,G}\frac{D_{os}}{D_{ol}\,D_{ls}}, \tag{7.8}$$

where c is the vacuum speed of light, G is the gravitational constant and D_{os}, D_{ol} and D_{ls} are the angular distances observer-sources, observer-lens and lens-sources, respectively (see also Section 2.2.1) .

With the photometric redshifts of the background sources, D_{os} and D_{ls} can be calculated, giving a value for the critical surface mass density:

$$\Sigma_{crit} = 1.39 \cdot 10^9\; h_{65}\; M_\odot\; kpc^{-2}$$

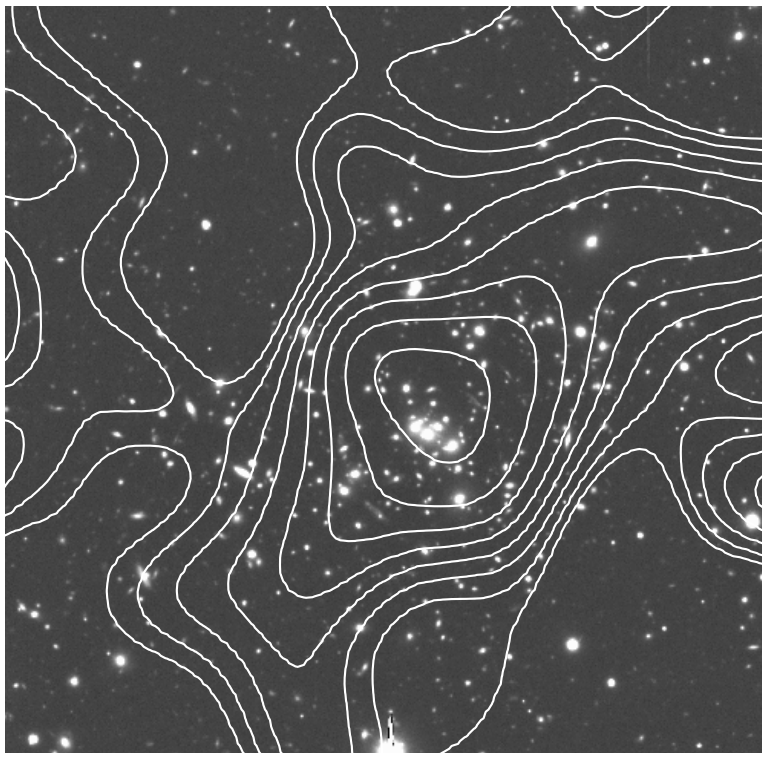

FIGURE 7.4: The κ-isocontours obtained with the mass reconstruction process on the R band image of the galaxy cluster Cl 0024+1654. The field of view is the common area of the FORS1 and ISAAC cameras (2'.5×2'.5), where the photometric redshift of the background galaxies was calculated. North is up and East is left.

The surface mass density profile $\kappa(\theta)$ is plotted in Fig. 7.5. It is calculated by computing annuli centered on the centre of the cluster – we assume the most luminous galaxy is the centre, which allows us to make comparisons with other authors –.

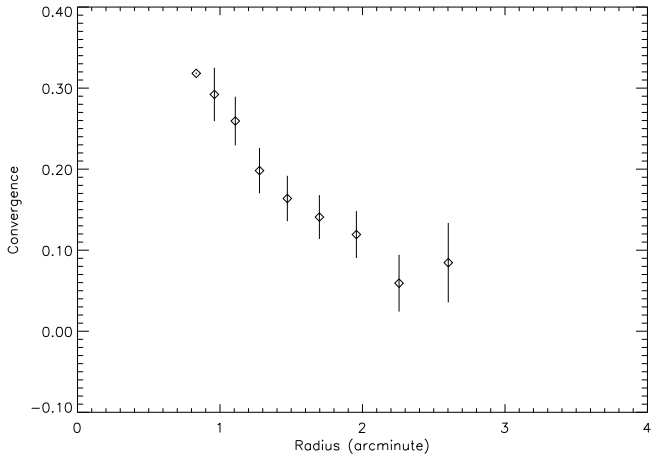

FIGURE 7.5: The surface mass density profile κ (or convergence) from the weak lensing analysis of Cl 0024+1654, using the image in the R band for the reconstruction.

7.5 Universal density profile fitting

Navarro et al. (1997, hereafter NFW) showed, through N-body simulations, that the equilibrium density profiles of CDM halos of all masses follow the simple distribution

$$\rho(\theta) = \rho_{crit}\,\frac{\delta_c}{(\theta/\theta_s)\,(1+\theta/\theta_s)^2} \tag{7.9}$$

where θ_s is a scale radius, δ_c is a characteristic dimensionless density and $\rho_{crit} = 3H^2/8\pi G$ is the critical density for closure (see Section friedmod. In general, low-mass halos are denser, so having higher values of δ_c than high-mass halos. The dimensionless density can be expressed in terms of a concentration parameter c as

$$\delta_c = \frac{200}{3}\frac{c^3}{ln(1+c) - c/(1+c)}. \tag{7.10}$$

That halos follow this NFW mass profiles would favor a universe dominated by collision-less dark matter. Nevertheless is not clear yet whether these NFW profiles rule out alternative density profiles, e.g. isothermal spheres (IS hereafter). This degeneracy can be easily explained since both NFW and IS profiles follow a similar r^{-2} behaviour at short and intermediate radial distances (a recent discussion on the validity and implications of the NFW density profiles can be found in Gavazzi et al. 2003).

The NFW profile results in a surface mass density κ profile given by (Bartelmann 1996)

$$\kappa(x) = \kappa_s \frac{f(x)}{x^2-1} \tag{7.11}$$

where

$$f(x) = \begin{cases} 1 - \frac{2}{\sqrt{x^2-1}}\,\tan^{-1}\sqrt{\frac{x-1}{1+x}} & , \quad (x>1) \\ 1 - \frac{2}{\sqrt{1-x^2}}\,\tanh^{-1}\sqrt{\frac{1-x}{1+x}} & , \quad (x<1) \\ 0 & , \quad (x=1) \end{cases} \tag{7.12}$$

$x = \theta/\theta_s$ and $\kappa_s = \rho_{crit}\ \delta_c\ \theta_s/\Sigma_{crit}$.

Once the surface mass density profile $\kappa(\theta)$ has been calculated after the mass reconstruction process, we fitted this profile to a NFW profile, obtaining the values for θ_s and δ_c. We got $\theta_s = 0.63^{+0.24}_{-0.22}$ and $c = 9.88^{+4.18}_{-2.22}$. The fitted mass profile is plot in Figure 7.6.

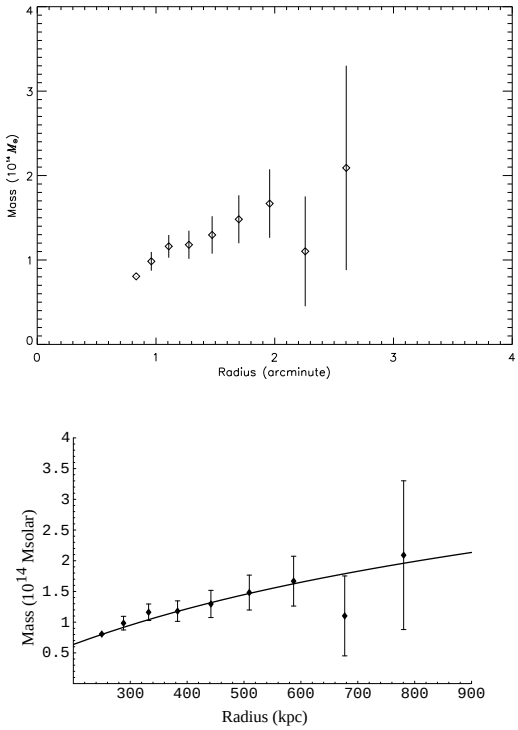

FIGURE 7.6: The mass profile from the weak lensing analysis of Cl 0024+1654. This done by computing consecutive annuli (see Eq. 7.6) on the surface mass density mapp in Fig.7.4 centered on the cluster centre. The *upper pannel* shows the mass profile with the radius expressed in arcminutes. The *lower pannel* is the fitted universal mass density profile NFW; the radius is expressed in kpc for comparison ($1' \approx 230$ kpc).

7.6 Light distribution and mass-to-light ratio

Having the surface mass density distribution computed for our field, it is interesting to compare this to the distribution of light in the same field. To do this, we computed the luminosity for each galaxy in the same R-band we used for the mass reconstruction.

The luminosity was then computed assuming no-evolution models and a K-correction for S0/E galaxies, since it is assumed most of the cluster members belong to this classification (see Sec. 7.3). The z=0.39 K-correction (the correction at the Cl 0024+1654 redshift) was kindly provided by Damian Le Borgne based on models by Bruzual & Charlot (1993). The value for the K-correction in the R-band filter was 0.46.

In Fig. 7.8 we show the luminosity map for the cluster members and the number density map. We can compare these maps to the κ-map in Figure 7.4 to see how well the κ-isocontours follow the light distribution. The mass-to-light M/L_R profile, which quantifies this comparison, is shown in Fig. 7.7. A fitting to a constant gives $M/L_R = (200 \pm 2)\ M_\odot/L_\odot$.

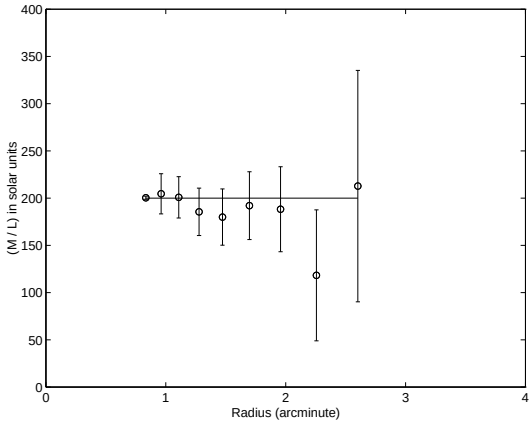

FIGURE 7.7: The mass-to-light ratio (M/L_R) profile of Cl 0024+1654 from the weak lensing analysis. Fitting a constant to the data we obtain $M/L_R = (200 \pm 2) M_\odot/L_\odot$.

7.7 Comparison with previous results and conclusions

Several lensing mass estimates have been reported so far from strong lensing modeling. Kassiola et al. (1992) and Smail et al. (1997) obtained $M(\theta \leq 220 h_{50}^{-1}\ \text{kpc}) = (2 \pm 0.2) \cdot 10^{14} h_{50}^{-1}\ M_\odot$, whereas Tyson et al. (1998) obtained a slightly higher value $M(\theta \leq 220 h_{50}^{-1}\ \text{kpc}) \approx 3.2 \cdot 10^{14} h_{50}^{-1}\ M_\odot$. Broadhurst et al. (2000), including a new arc redshift measurement at $z = 1.675$ in the lens modeling and thus breaking the mass-redshift degeneracy in those previous models, obtained $M(\theta \leq 220 h_{50}^{-1}\ \text{kpc}) = (2.6 \pm 0.06) \cdot 10^{14} h_{50}^{-1}\ M_\odot$, a value very close to that from Kassiola et al. (1992) and Smail et al. (1997). They also claimed that some substructure is required in Cl 0024+1654 – contrary to what Tyson et al. (1998) concluded – due to the high mass-to-light ratio they assigned to the central luminous elliptical galaxies, implying a well local minima of a more general potential.

Using X-ray ROSAT observations, Böhringer et al. (2000) found a cluster mass of $(3\text{-}4) \cdot 10^{14} h_{50}^{-1}\ M_\odot$ within a radius of $3 h_{50}^{-1}$ Mpc. They also reported the core size of the mass halo to be $66^{-25}_{+38} h_{50}^{-1}$ kpc, compatible to those found by Tyson et al. (1998) and Smail et al (1997), $70 h_{50}^{-1}$ kpc and $(40 \pm 10) h_{50}^{-1}$ kpc, respectively. Böhringer et. al (2000) concluded that although the X-ray mass is consistent with the core mass of strong lensing results, there could be much more unrelaxed gas surrounding the cluster. Furthermore, Soucail et al. (2000) from their X-ray ROSAT+ASCA analysis found $M(\theta \leq 220 h_{50}^{-1}\ \text{kpc}) = 0.96^{+0.82}_{-0.35} \cdot 10^{14} h_{50}^{-1}\ M_\odot$ and extrapolating the total mass $M(\theta < 3 h_{50}^{-1}\ \text{Mpc}) = 1.4^{+1.2}_{-0.5} \cdot 10^{15} h_{50}^{-1}\ M_\odot$

On the other side, from weak lensing studies, Bonnet et al. (1994) found a mass of $4 \cdot 10^{15} h_{50}^{-1} M_\odot$ within $3 h_{50}^{-1}$ Mpc, assuming that the mass density profile remains isothermal at this distance. And from the velocity dispersion of 26 cluster members, Schneider et al. (1986) inferred a cluster mass of $M(\theta < 480 h_{50}^{-1}\ \text{kpc}) = 6.6 \cdot 10^{14} h_{50}^{-1}\ M_\odot$.

From our mass profile in Figure 7.6, we can obtain a reference value for the mass at a given radius. Thus, we get a mass of $M(\theta \leq 230 h_{65}^{-1}\ \text{kpc}) = (0.98 \pm 0.11) \cdot 10^{14}\ M_\odot$. This value is in surprising good agreement with that obtained by Soucail et al. (2000) in X-rays and a factor of 2 smaller than other previous estimates using strong lensing. This result is surprising because usually the discrepancy is between X-rays and optical estimates, rather than between strong and

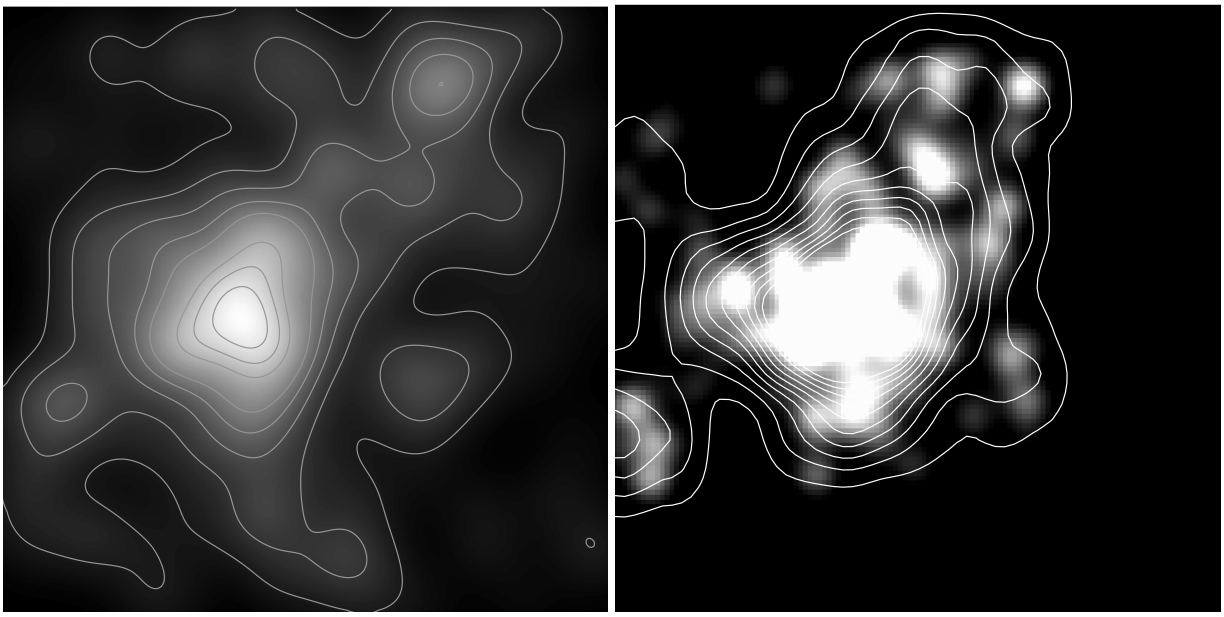

FIGURE 7.8: The *left pannel* shows the number density of galaxies members of Cl 0024+1654. The *right pannel* is the luminosity distribution of the same galaxies. The field is the same as in Fig. 7.1, $6'.8 \times 6'.8$. North is up and East is left.

weak lensing ones, in the case of Cl 0024+1654. Furthermore, our estimates are also in agreement with the results obtained by Ota et al. (2003) using the CHANDRA X-ray satellite.

Kneib et al. (2003) have recently presented a wide-field HST study of Cl 0024+1654, based on a panoramic sparse-sampled imaging. They detected weak lensing signal up to a radius of $\sim 5\ h_6^{-1} 5$ Mpc. Moreover, they found a secondary mass peak located at $\sim$1 Mpc NW of the cluster centre, which corresponds with the substructure already detected by Czoske et al. (2002). This would mean that the galaxy cluster Cl 0024+1654 is not a 'typical relaxed cluster at all. They also found that the mass-to-light ratio (M/L) keeps constant at large radii – which agrees with our M/L profile –.

These results suggest that numerical simulations would be very helpful in order to carefully analyse all these discrepancies and to explain the physical state of Cl 0024+1654

Chapter 8

A search for gravitationally lensed arcs in the z=0.52 galaxy cluster RBS380 using combined CHANDRA and NTT observations⋆

Link. *New clusters of galaxies are mainly discovered during X-ray surveys. Their X-ray luminosity can be used to roughly estimate their masses. After these serendipity discoveries, optical follow-ups are carried out in order to determine the redshifts of such systems. With both the mass and the redshift one can assign certain probability to a cluster as acting as a gravitational lens, suggesting a deeper and more detailed study of a given cluster. But things are not usually as simple as this. If, e.g., point sources are not properly removed when estimating the X-ray luminosity of a galaxy cluster, erroneous conclusions can be achieved.*

Abstract. CHANDRA X-ray and NTT optical observations of the distant $z = 0.52$ galaxy cluster RBS380 – the most distant cluster of the ROSAT Bright Source (RBS) catalogue – are presented. We find diffuse, non-spherically symmetric X-ray emission with a X-ray luminosity of $L_X(0.3 - 10 \text{ keV}) = 1.6\ 10^{44}$ erg/s, which is lower than expected from the RBS. The reason is a bright AGN in the centre of the cluster contributing considerably to the X-ray flux. This AGN could not be resolved with ROSAT. In optical wavelength we identify several galaxies belonging to the cluster. The galaxy density is at least 2 times higher than expected for such a X-ray faint cluster, which is another confirmation of the weak correlation between X-ray luminosity and optical richness. The example of the source confusion in this cluster shows how important high-resolution X-ray imaging is for cosmological research.

⋆Chapter based on the refereed publication Gil-Merino & Schindler, A&A, in press (also as astro-ph/0306499)

8.1 Introduction

The galaxy cluster RBS380 is part of a large optical programme to search for strong gravitationally lensed arcs in X-ray luminous clusters selected from the ROSAT Bright Survey (RBS, Schwope et al. 2000), with a predicted probability for arcs of 45%. In addition to the optical images X-ray observations are taken in order to compare masses determined with different methods and to use the X-ray morphology for lensing models. The main goal of this project is to combine X-ray and optical information, together with possible gravitational lensing information, to constrain cosmological models.

The cluster presented here – RBS380 – is after RBS797 (Schindler et al. 2001) the second cluster for which we have performed a combined optical and X-ray analysis. The X-ray source RBS380 was found in the ROSAT All-Sky Survey (RASS, Voges et al. 1996, 1999) and classified as a massive cluster of galaxies in the RBS. RBS380 is the most distant cluster of this catalogue.

We present here CHANDRA ACIS-I and NTT SUSI2 observations of the X-ray cluster RBS380 at $z = 0.52$ and coordinates $\alpha = 03\ 01\ 07.6$, $\delta = -47\ 06\ 35.0$ (J2000).

We find a lower X-ray luminosity than expected from the RBS. The reason is source confusion in the ROSAT data – the X-ray emission of the central AGN had been mixed up with cluster emission –.

The high galaxy number density in this cluster is in contrast to its low X-ray luminosity. This is another confirmation that optical luminosity is not well correlated with X-ray luminosity, see e.g. Donahue et al. (2001) or the clusters Cl0939+4713 and Cl0050−24 for extreme examples of optical richness and low X-ray luminosity (Schindler & Wambsganss 1996, 1997; Schindler et al. 1998).

Throughout this Chapter we use $\mathrm{H}_0 = 65$ km/s/Mpc, $\Omega_\mathrm{M} = 0.3$ and $\Omega_\Lambda = 0.7$.

8.2 Data acquisition and reduction

8.2.1 X-ray data reduction

The cluster RBS380 was observed on October 17, 2000 by the CHANDRA X-ray Observatory (CXO). A single exposure of 10.3 ksec was obtained with the Advanced CCD Imaging Spectrometer (ACIS). During the observations the 2×2 front-illuminated array ACIS-I was active, together with the S0 chip of the ACIS-S 1×6 array, although this last one was not used for the data reduction, since the expected cluster centre was placed on the ACIS-I array. Each CCD in the ACIS-I is a 1024×1024 pixel array, each pixel subtending $0''.492 \times 0''.492$ on the sky, covering a total area of $16'.9 \times 16'.9$.

The data were ground reprocessed on February 28, 2001 by the CHANDRA X-ray Center (CXC). The analysis of these reprocessed data was performed by the CIAO-2.2 suite toolkit.

As upgraded gainmaps from preprocessing were available, we used the *acis_process_events* tool to improve the quality of the level_2 events file. We also corrected for aspects offsets and removed bad pixels in the field. For that we used the provided bad pixel file acisf02201_000N001_bpix1.fits by the CXC. We built the lightcurve for the observation period and we searched for short high backgrounds intervals. We found none, so no data filtering was needed.

Since we are interested in the diffuse emission of the galaxy cluster, special attention has to be paid to the removal of point sources. This extra care is not needed when the count rate is high enough, since the cluster emission can be seen even without any processing. If the number of counts from diffuse cluster emission is low, any not removed point source can induce wrong estimates. In a broadband ($0.3 - 10$ keV) image, we applied two different procedures for the detection of sources: *celldetect* and *wavdetect*. The latter uses wavelets of differents scales and correlates them with the image; the former uses sliding square cells with the size of the instrument PSF. In general, *celldetect* works well with well-separated point sources, although a low threshold selection will obviously overestimate the number of point sources. On the other hand, *wavdetect* tends to include some diffuse emission regions as point sources. For these reasons, a scientific judgment must be applied in order to decide which regions must be identified as point sources. Using a sigma threshold of 10^{-6} in the *wavdetect* routine, we found 31 point sources, expecting a probability of wrong detections of 0.1 in the image. Using analogous criteria for the *celldetect* routine we found no significant differences.

The correction for telescope vignetting and variations in the spatial efficiency of the CCDs was done by means of an exposure map, using the standard procedure of the CIAO-2.2 package. The exposure map was generated for an integrated energy distribution peak. The value of the peak was slightly different depending on the included region. Selecting the whole effective area of the ACIS-I array, the peak value was 0.7 keV. If the selected area was only the region covering the central part of the cluster (a circle of radio $1'.5$), the value of the peak was then 0.5 keV. We used these two values for the reduction and we could not see any significant change in the final result.

The background correction was done using a blank field background set acisi_C_i0123_bg_evt_-230301.fits provided by the CXC. We used a blank field instead of a region from the science image, since one cannot be sure a priori whether a certain region in the field is free of galaxy cluster emission. The smoothing process for the final image was done with the *csmooth* CIAO tool and compared to the result using the IRAF[1] (Image Reduction and Analysis Facility) task *gauss* (using a $\sigma = 20$ pixels Gaussian) to be sure that no artificial features were created in the convolution process. We found no significant differences.

8.2.2 Optical data reduction

The galaxy cluster RBS380 was observed in optical wavelength with the New Technology Telescope (NTT) in service mode during summer 2001. The Superb Seeing Imager-2 (SUSI2) camera was used in bands V and R. The SUSI2 detector is a 2 CCDs array, 1024×2048 pixels each, subtending a total area on the sky of $5'.5 \times 5'.5$ (the pixel size in the 2×2 binned mode is $0.16''/pixel$). In order to be able to avoid the gap between the two chips during the data reduction process, dithering was applied.

The data reduction was perfomed with the IRAF package. A total number of 6 images in R band and 3 in V band in very good seeing conditions ($\leq 1''$) were used in the analysis. The exposure time was 760 sec for each image. For each band, after bias subtraction, a standard flatfielding was not enough to produce good results, because the twilight flats provided by the NTT team contained some stars and the scientific images showed stronger gradients than the flats. A hyperflat (see

[1]IRAF is distributed by the National Optical Astronomy Observatories, which are operated by the Association of Universities for Research in Astronomy, Inc., under cooperative agreement with the National Science Foundation.

e.g. Hainaut et al. 1998) was built to flat-correct the images. We briefly describe the hyperflat technique here.

To produce a hyperflat we processed separately the provided twilight flats and the scientific images, although the procedure will be analogous in both sets. The technique is to smooth strongly all the bias subtracted and normalized frames (with e.g a Gaussian $\sigma = 100$ pixels). The result is then subtracted from the original frames, so one obtains a very flat background, but still with stars in the images. Smoothing again the result with a smaller Gaussian (e.g. $\sigma = 20$ pixels) will show all the stars. One can then mark all these stars in the original frames, median average them and reject the marked values. Applying this procedure to the twilight flats set and to the scientific images set, one obtains a final twilight flat and a final night-sky flat, respectively. A linear combination of these two yields the final hyperflat.

Once the images are flatfielded, they can be co-added, resulting in a deep image of the field and free of chip gaps. Note that the whole procedure has to be done for each filter.

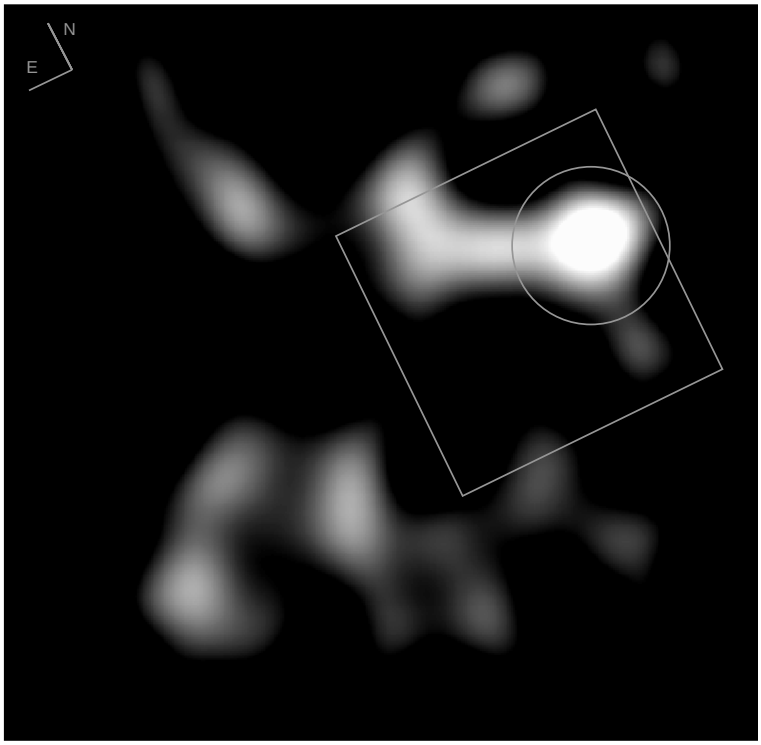

FIGURE 8.1: X-ray image of RBS380 (z=0.52) in the (0.3-10 keV) band, adaptatively smoothed with the *csmooth* CIAO tool and cross-check with the IRAF *gauss* task. The total area is $14' \times 14'$. The rotated square shows the region that was observed in the optical band (V and R). The circle with a radius of $1'.5$ marks the area within which we have computed a count rate of 0.05 counts/s. Point-like X-ray sources have been removed. North and East are marked.

FIGURE 8.2: Optical R band image of RBS380 (z=0.52). The total area is $5' \times 5'$. North is up and East is left.

8.3 Analysis and results

8.3.1 X-ray results

The final X-ray image after data reduction (including point sources removal) is shown in Fig. 8.1. We encircle the main cluster emission within a radius of $1'.5$ centred on the peak of the emission. The count rate obtained in that area is 0.05 counts/s. We compared this count rate to the count rate of the same region in the background fields, finding a value of 0.02 counts/s. We found that this background count rate was in fact not very sensitive to its position in the field, as expected. Using a weighted average column density $nH = 2.23 \cdot 10^{20}$ cm^{-2} (Dickey & Lockman 1990), a Raymond-Smith source model with $T = 5$ keV and the cluster redshift $z = 0.52$, the derived luminosity is $L_X(0.3 - 10keV) = 1.6 \cdot 10^{44}$ erg/s. Using slightly lower numbers for the temperature in the source model (in the range 3-4 keV), reduces the final luminosity result in only by a few per cent. This is a relatively low X-ray luminosity for a massive cluster of galaxies. As the luminosity is so low we were particularly careful with the background subtraction and the removal of point sources.

The X-ray luminosity is lower than expected from the RBS results. The reason is an X-ray point source centred on the coordinates $\alpha = 03\ 01\ 07.8$ and $\delta = -47\ 06\ 24.0$. The point source is probably an AGN which could not be resolved with ROSAT and therefore not distinguished from cluster emission. The AGN is probably the central cluster galaxy. Within a radius of $7''$ we find a count rate of 0.07 counts/s for this point source. Using a power law model with photon index 2, the same column density as for the cluster and an energy range [0.3-10 keV], the obtained flux for this AGN is $f_X = 8.2 \cdot 10^{-13}$ erg cm^2 s^{-1}. This AGN is one of the galaxies for which the RBS

Name	α_{2000}	δ_{2000}	Counts [cts/s]	L_X [erg/s]
AGN	03 01 07.8	-47 06 24.0	0.07	1.8 10^{44}
RBS380	03 01 07.6	-47 06 35.0	0.05	1.6 10^{44}

Table 8.1: Coordinates of the AGN and the cluster. The AGN is almost at the centre of the cluster emission. We also show the count rate for the two objects (normalized for the different apertures, see text for details) and the luminosities, both in the [0.3-10 keV] band (bolometric luminosity for the cluster is given in Tab. 8.2). The contribution of the AGN is larger than the cluster luminosity. Both objects are at the same redshift of 0.52. An optical counterpart of the AGN is marked in Fig. 8.7.

optical follow-up observations (Schwope et al. 2000) yielded a redshift of 0.52 (see Fig. 8.7). In Tab. 8.1 we summarise the coordinates, count rates and luminosities of the AGN and the cluster.

In addition to the main cluster emission within a circle of radius $1'.5$ described above, we found an asymmetric structure extending to both sides of this main region. If this is cluster emission, it could indicate that the cluster is not relaxed, but interacting with surrounding material or/and an infalling galaxy group. In any case we consider the inferred X-ray luminosity L_X as an lower limit for the cluster. Due to the low number of X-ray counts we did not perform any spectral analysis.

8.3.2 Optical results

Both V and R images show a high number density of galaxies. The main goal is to find a way of selecting the cluster members in order to determine their number and their spatial distribution. We select cluster members through a colour-magnitude relation, applying it to all the galaxies detected both in V and R bands.

We use the SExtractor[2] (Source-Extractor) package to build the catalogue for images V and R. First we extract all the objects detected in both images with a detection threshold of 2σ over the local sky. We show in Fig. 8.3 all the detected objects in both bands, representing uncalibrated magnitude vs. FWHM. In the two plots a vertical stellar locus is clearly seen at the position of the expected seeing for each image (FWHM$= 1.1$ for V and FWHM$= 0.75$ for R). We consider all objects to the right of these values as being galaxies. In the V band, many objects lie on the lower left side of the vertical stellar locus. We think the problem is due to the low S/N value in the final V image, built with only 3 original frames.

We select the galaxies present in both images and calibrate the magnitudes. For the calibration we use data from the SuperCOSMOS Sky Survey[3] (SSS). We obtain from the SSS the magnitudes in R and B_J for two galaxies in our field (see both marked in Fig. 8.7). The calibration for our R filter is straightforward. For our V filter we use the B_J contained in the SSS. This means that our V filter is not perfectly calibrated, but the offset does not induce any difference in our results (since we are interested in the shape/slope of the colour-magnitude diagram of our galaxies, the offset induces only a vertical shift of all the objects in the plot).

In Fig. 8.4 we show the selected galaxies in both V and R images. Stars and deficient detections

[2]available at http://terapix.iap.fr/soft/sextractor/index.html

[3]http://www-wfau.roe.ac.uk/sss/

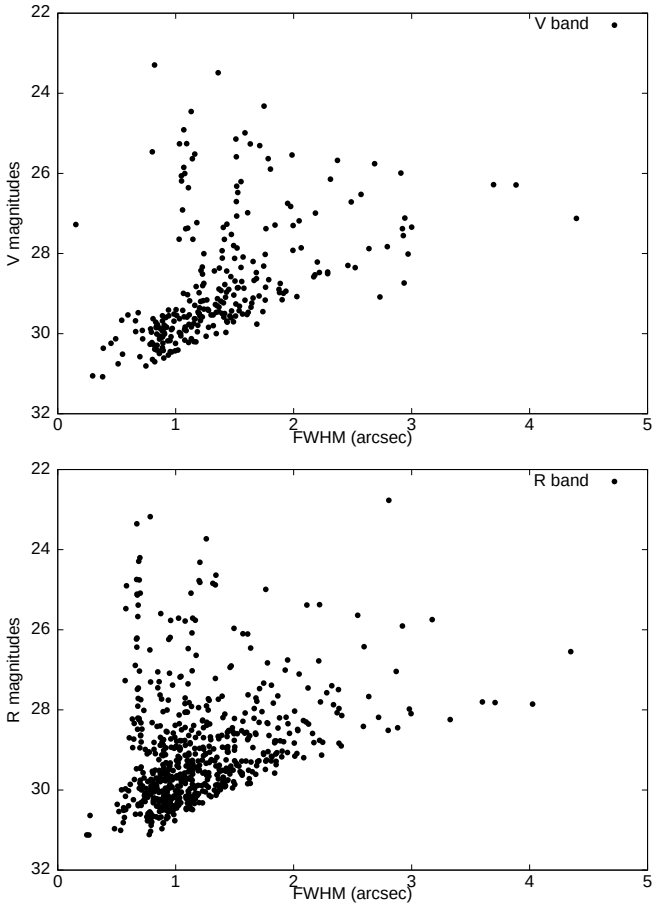

FIGURE 8.3: All the objects detected in V (upper panel) and R (lower panel) bands. A vertical stellar locus is present in both plots at the position of the seeing for each image. The magnitudes are not calibrated.

(SExtractor indicates this with different flags) are rejected. The number of galaxies is 452 in the R filter and only 64 in the V filter. This represents a 70% of the total number of objects detected in R and only a 23% of the objects detected in V.

The next step is to cross-check which galaxies detected in the V image were also detected as galaxies in the R image. We find that all the galaxies in V (64) are also present in the R catalogue.

The existence of a relation between colour and magnitude for early-type galaxies is well known (Baum 1959; Sandage & Visvanathan 1978). In Fig. 8.5 we show the colour-magnitude relation for the selected galaxies. Since the presence of a red sequence of early-type galaxies is an almost universal signature in clusters (Gladders et al. 1998, Gladders & Yee 2000 and references therein) and clusters at $z \approx 0.5$ tend to concentrate elliptical galaxies in their central regions (Dressler et al. 1997), we look for this sequence in our data. We select only the galaxies below 23^{rd} magnitude as this is our completeness limit (see Fig. 8.6 upper panel for completeness), and we fit the remaining galaxies by a straight line. Note that this fit is not sensitive to calibration problems, these induce only a vertical shift in the line. We used a robust statistical method based on minimizing the absolute deviation, which is expected to be less sensitive to outliers compared to standard linear regression (Press et al. 1992).

The result, presented in Fig. 8.6 lower panel, shows a red sequence with slope 0.06. According

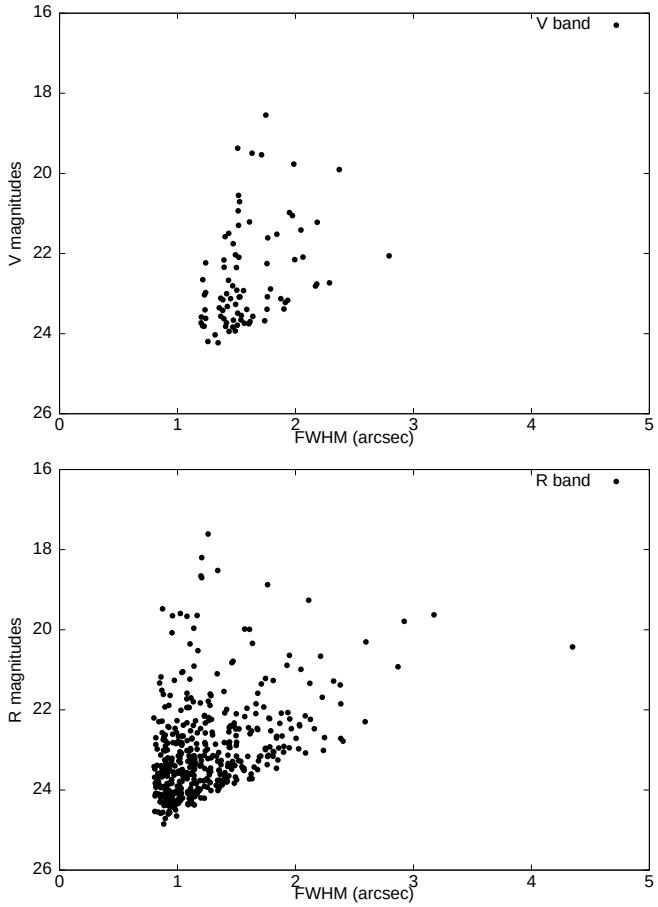

FIGURE 8.4: Galaxies detected in V (upper panel) and R (lower panel) bands. The magnitudes are calibrated using the SSS archive.

to the predicted slopes for formation models of galaxy clusters as a function of redshift in Gladders et al. (1998, see their Fig. 4), this slope is compatible with a galaxy cluster at $z = 0.5$. This value does not strongly depend on the cosmology. This is particulary interesting because we would have derived a most likely redshift of ≈ 0.5 from this prediction, which is in good agreement with the actual redshift of 0.52.

8.4 Comparison: X-ray vs. Optical

In Fig. 8.7 we show the selected galaxies through the colour-magnitude relation, using the R image. We now want to compare the galaxy number density to the distribution of the X-ray emission in the same area. For the number density map, using a blank image of the same size as the optical image, we allocate pixels with value 1 in all the positions where we detected a galaxy, and then we smooth it strongly (i.e. with a 200 pixels Gaussian). We need such a large smoothing Gaussian because of the low number of galaxies finally detected. In this way we obtain the smooth distribution of the galaxies in the field.

From the X-ray image we extracted the contour lines from the squared region shown in Fig. 8.1

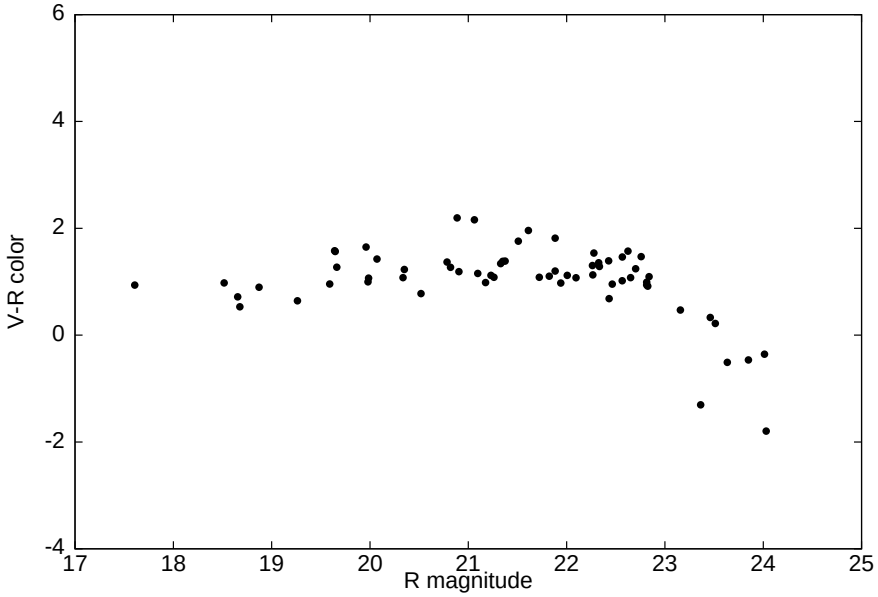

FIGURE 8.5: Colour-magnitude diagram for the detected galaxies both in V and R filters. Although the final number of galaxies is low due to the low number of detection in V band, a close relation can be infered at least up to a limit of 23^{rd} magnitude.

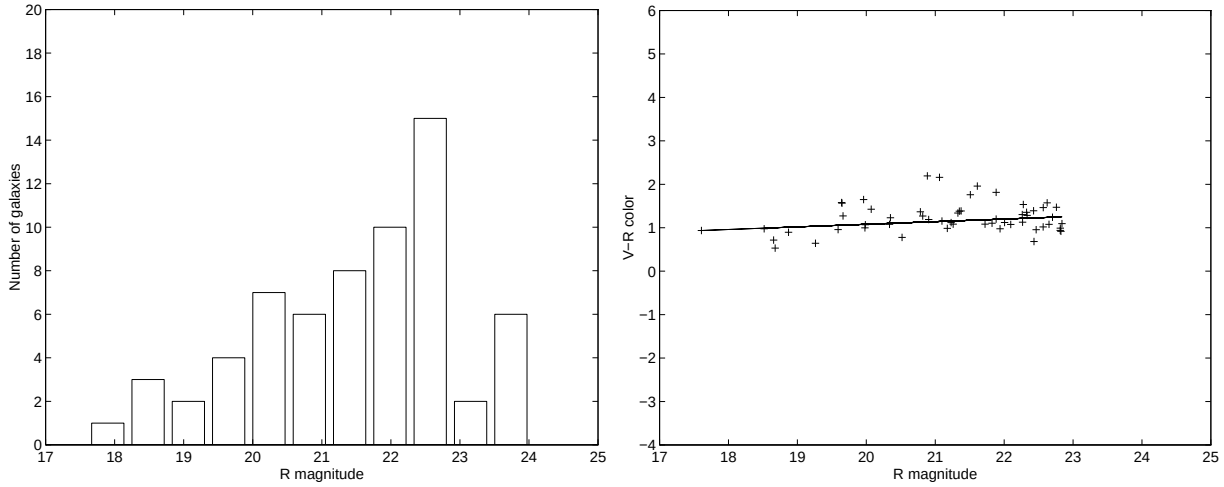

FIGURE 8.6: *Left panel*: In the distribution of galaxies for the R filter we see the completeness until the 23^{rd} magnitude, where there is a drop in the number of galaxies detected. *Right panel*: The fit shows a red sequence of the detected early-type galaxies with a slope of 0.06.

(which corresponds to the observed region in the optical). In Fig. 8.8 we plot the galaxy number density together with the X-ray contour lines. The main maximum peak in the number density map is shifted by 2 arcmin in SE direction with respect to the X-ray maximum. Nevertheless, galaxies are present close to the asymmetric X-ray features on both sides of the main peak (in N and NE direction). These asymmetric features might indicate the existence of surrounding material interacting with the cluster, e.g. infalling galaxy groups.

The number of galaxies to the limiting magnitude is at least 2 times higher than expected for a such faint X-ray cluster (using the number of cluster members detected in an Abell radius of $R \leq 1.5\ h^{-1}$ within the centre of the cluster) but since the detection members efficiency is not complete due to the V band poor quality, this number could even be higher. This is another confirmation that number of galaxies and X-ray luminosity are not well correlated (see Table 1 for a comparison with other X-ray underluminous clusters).

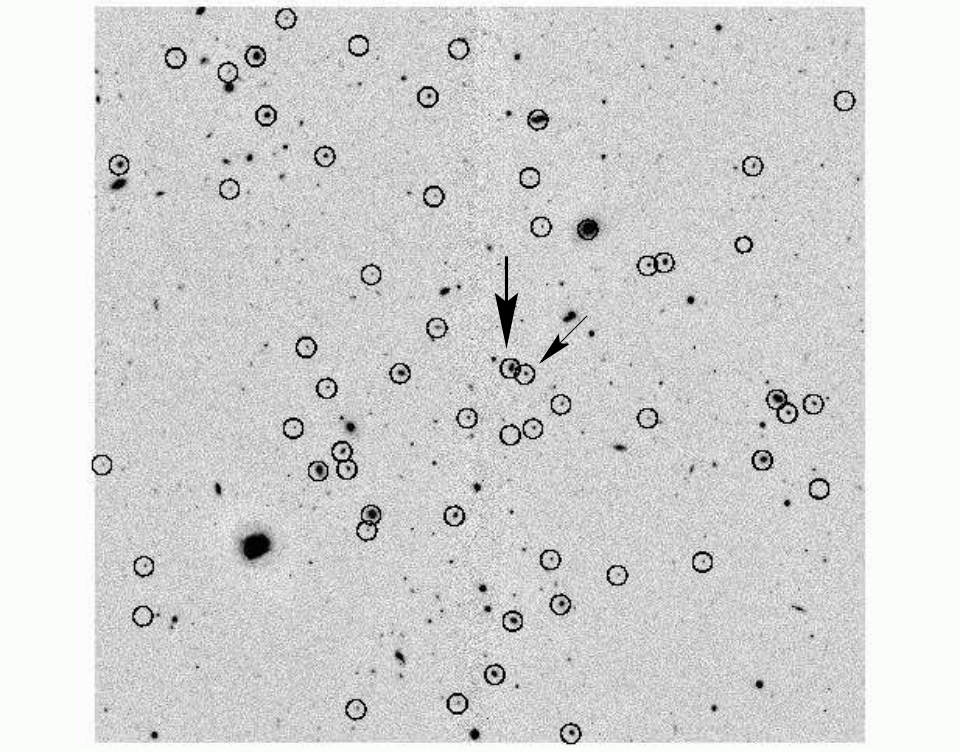

FIGURE 8.7: Optical R band image of RBS380 (z=0.52). The total area is $5' \times 5'$. We have inverted colours and marked the galaxies that were detected as cluster members using both R and V bands with a circle. The arrows indicate the two galaxies used for the calibration from the SSS (see text for details). The thicker arrow shows the AGN described in Sec. 8.3.1 and in Tab. 8.1. North is up and East is left.

8.5 Conclusions

The X-ray source RBS380 was found in the RASS and identified as a cluster of galaxies in the RBS. From the RBS catalogue, the cluster was expected to be very massive due to its inferred

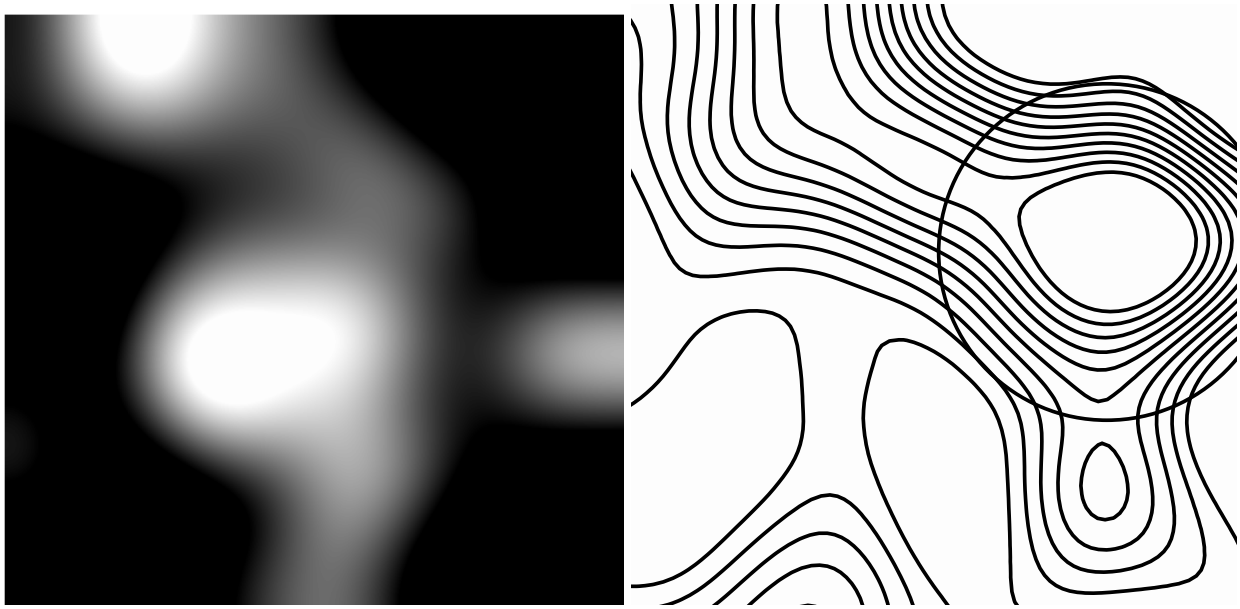

FIGURE 8.8: RBS380 galaxy number density in the R band (left panel) and the X-rays contours for the same region (right panel). The circle with radius $1'.5$ is the same as in Fig. 8.1. The total area in both panels is $5' \times 5'$. North is up and East is left.

Name	Redshift	Luminosity [erg/s]	band
Cl0500−24	0.32	5.6 10^{44}	bolometric
Cl0939+4713	0.41	7.9 10^{44}	bolometric
RBS380	0.52	2 10^{44}	bolometric

Table 8.2: We compare the X-ray luminosity of RBS380 with two more clusters of galaxies which are optically rich, but have relatively low X-ray luminosity. For comparison, we give the bolometric luminosity for RBS380 too.

high X-ray luminosity. Its redshift $z = 0.52$ makes it the most distant galaxy cluster in that catalogue. Our interest in this object was due to its predicted probability (up to 60%) of acting as a gravitational lens. In fact these observations are part of a broader project that searches systematically for gravitational arcs in different galaxy clusters and combines this optical information with X-ray studies of the same clusters in order to constrain cosmological models and find possible correlations between X-ray and optical properties of them.

With the new CHANDRA imaging we detect a strong X-ray point source (an AGN) very close to the cluster centre, which could not be resolved with ROSAT. After subtracting the emission of this AGN, the remaining diffuse emission is almost one order of magnitude less luminous than expected: $L_X = 1.6 \cdot 10^{44}$ erg/s. No previous investigation of the system has been carried out, so our first aim was to make sure that it is really a cluster of galaxies. The X-ray CHANDRA observation shows a non-relaxed cluster of galaxies probably interacting with surrounding material or/and another nearby cluster.

From the NTT optical observations we are able to distinguish some of the cluster members by

means of the colour-magnitude relation for early-type galaxies present in the cluster, which is a well known signature for almost every cluster of galaxies. The obtained slope for this red sequence is 0.06. Using existing predicted slopes for different formation models as a function of redshift, the most likely redshift for this slope is $z \approx 0.5$, in good agreement with the measured redshift of 0.52.

We could not detect any gravitational arc in this cluster. This is not surprising as with the low X-ray luminosity the probability for arcs is strongly reduced.

The example of this cluster shows that high-resolution X-ray imaging is crucial for cosmological research. This type of distant galaxy clusters is often used for various types of cosmological applications. Due to source confusion some clusters can have wrong luminosity measurements and hence influence the results. This effect might e.g. artificially flatten the luminosity function for distant clusters.

Part IV

Final Remarks

Chapter 9

Summary

Ojalá quien visite este folleto
sea lego en Chaquespiare y en sor Juana
no compite mi boina de paleto
con el chambergo de Villamediana.

JOAQUÍN SABINA

9.1 Overall conclusions

A thesis period is thought to be a training time in which the candidate acquires the ability of conducting research by his/her own. There are many different ways of doing so and the candidate is, in many cases, the one with less control on it. Different advisors put emphasis on different aspects – sometimes in opposite directions –, observations break down or the data adquisition is not good enough or someone you need for something is on the other side of the World. On the top of that, research is often a blind random walk, a fuzzy dancing in the middle of nowhere and instead of light at the end of the tunnel, one only sees flashes that cloud even more the direction to follow. At some point the thesis project, like an undesired Frankenstein, wakes up to life and there is not much one can do to keep it under control.

This thesis was planned from the beginning as an investigation on different aspects of lensing. The goal was to learn different techniques establishing a solid background for the future. In the end, it has been that, but I also had to go into other problems far from lensing which I decided not to include in the report (different data reduction problems, mathematical analysis of time delay methods, etc.). And, moreover, learning different techniques is not possible without working closely with different people, so that I was lucky to do science in several institutions. In this way, when the thesis project was alive it had most of the ingredients I wanted it to have.

Obviously, if the reader is not familiar with the techniques or with the state of the art of the topic, it is difficult to place the results in their proper context. The first part of the thesis is devoted to this purpose. We give some historical guidelines and then introduce the background needed throughout the rest of the chapters. And in order to give an actual perspective of the work, we present the most recent aspects of gravitational lensing. In parts II and III we present our research, the former dedicated to quasar lensing and microlensing and the latter to galaxy cluster lensing and X-rays. We highlight here the main conclusions obtained along this work:

- We determine a time delay for the double quasar HE 1104−1805 (Chapter 4), using a poorly sampled dataset. We explore in detail a number of techniques and find differences in their behaviour. In general, well sampled datasets are difficult to obtain and it is interesting to know under which circumstances the available techniques will give useful results. We find that the dispersion spectra method has some difficulties that are not found in the rest of the techniques. The more robust result is found with the δ^2 method, which gets the time delay by minimizing the differences between the autocorrelation and the cross-correlation functions of the two components. We obtain a time delay $\Delta t_{A-B} = (-310 \pm 20)$ days (2σ errors). A quite different time delay has been reported recently. This new value of $\Delta t_{A-B} = (-161 \pm 7)$ days (1σ errors) is obtained using a photometric dataset with much better sampling but with a high microlensing signal. The results probably need further investigation.

- In Chapter 5 we perform an analysis of three monitoring campaigns (1996/98) of the double quasar Q0957+561. We are able to construct two difference light curves of the system (the time delay is 420 days). We analyse the fluctuations we see in the difference light curves with Monte Carlo simulations. We conclude that they are completely consistent with noise and no microlensing is needed to explain them. The sources of noise can be instrumental, observational or the data reduction itself. These conclusions were extended for two more years of observations (1998/2000). Recently, other authors arrived at similar conclusions (Colley et al. 2003a).

- The system Q2237+0305 studied in Chapter 6 was observed during four months. Microlensing is a well known signature in this system and has been detected by several teams. In our observing period, two images showed little or no strong microlensing signal. We use this behaviour to put limits on the effective transverse velocity of the lens galaxy. We conclude that $v_{\rm bulk} \leq 570$ km/s considering microlenses with $M_{\rm lens} = 0.1\ M_\odot$ and $v_{\rm bulk} \leq 1000$ km/s for $M_{\rm lens} = 1\ M_\odot$.

- Chapter 7 is dedicated to the cluster of galaxies Cl 0024+1654. This is one of the most studied cluster in many aspects. Here we concentrate on the weak lensing signal that can be detected in the background galaxies. We use this weak lensing to get a mass profile of the cluster, obtaining a reference values of $M(\theta \leq 230 h_{65}^{-1}\ \text{kpc}) = (0.98 \pm 0.11) \cdot 10^{14}\ M_\odot$. We compare this profile to the light distribution. We get an almost constant mass-to-light ratio $M/L \simeq 200\ M_\odot/L_\odot$ within a radius of 3 arcminutes. We found that the best fit to a universal mass density profile (Navarro et al. 1997) has parameters $\theta_s = 0.63^{+0.24}_{-0.22}$ and $c = 9.88^{+4.18}_{-2.22}$. Our mass estimate is in agreement with previous estimates from X-ray studies, which was unexpected since usually there is a discrepancy of a factor of 2-3 lower in X-rays results.

- The cluster of galaxies RBS380 (Chapter 8) is the most distant cluster in the ROSAT Bright Source catalogue ($z = 0.52$). It was thought to be a very massive galaxy cluster due to its apparent high X-ray luminosity. For this reason it had a predicted probability of $\approx 50\%$ for producing gravitational arcs of background galaxies. Nevertheless, we found that the former X-ray luminosity estimate was erroneous due to the presence of an AGN close to the centre of the galaxy. This AGN contributes about 60% of the total X-ray luminosity. In spite of this low luminosity, we still see an optically rich cluster, which gives another example of an unclear correlation between optical richness and high X-ray luminosity.

9.2 Future work

It is quite hard, probably one of the most difficult things to write, to imagine the problems I would like to solve in the future when my 'only' worry is to finish up this thesis. In any case, there are many open and interesting questions derived from or in parallel to the research presented here.

A very promising tool for the estimate of the Hubble constant is statistics on gravitational lensed systems with known time delays. This means that regular monitoring of multiple quasars is required. But it is also important to understand properly the techniques we use for the determination of the time delays. Currently we have more time delay methods than measured lags. This means that each author has encountered different problems and tried to solve them with a new method. In my view, a deep analysis of the techniques is needed, a classification that allows to know which is the best technique for a given system – or a given dataset –, and what the pros/cons of each technique are. This will be the only way to properly evaluate the result and to compare the different results.

The double quasar HE 1104−1805 is a fascinating system. The amount of microlensing that it shows is a problem for time delay estimates, but opens many other interesting points. In fact, several scenarios have been proposed to interpret its high microlensing signal. One of the possible, and probably one of the best, ways to try to clarify this situation is a multiband analysis of the system. If the microlensing signal is, e.g., seen in optical but not in infrared, we can put limits to the size of the regions in which the cause of microlensing might be.

Although the double quasar Q0957+561 was the first discovered lensed quasar and has been studied for long, the system is not fully understood. Several authors claimed that the little discrepancy of the published time delays can only be explained with the existence of multiple time delays. The short-time scale fluctuations reported by several authors are very likely due to different types of noise, so a careful data reduction process is always needed. Furthermore, the long-term variability has been clearly detected, but interpreted differently by different authors. A long term campaign would be the best way to clarify these issues.

Numerical simulations are very powerful tools in lensing studies. The analysis we performed with the quadruple quasar Q2237+0305 was done with limited computer resources. Large simulations with magnification patterns $\geq 10^4 \times 10^4$ pixels will help to put stronger limits on physical properties of the system – source size, effective transverse velocity, etc. –.

The cluster of galaxies RBS380 has revealed itself as one of the cases in which high resolution X-ray imaging is crucial. In order to improve the understanding of the system, new observations would increase the signal-to-noise statistics. Furthermore, the mix up of point sources and intracluster gas emissions could occur in more cases, with a significant impact on the luminosity function for distant clusters. And, as it was concluded from the analysis of RBS380, the correlation between optical richness and high X-ray luminosity is far from being clear. This issue deserves more attention.

Acknowledgments

[...] señas esclarecidas
que, con llama parlera y elocuente,
por el mudo silencio repartidas,
a la sombra servís de voz ardiente;
pompa que da la noche a sus vestidos,
letras de luz, misterios encendidos; [...]

FRANCISCO DE QUEVEDO

Starting this work with a historical introduction seems to be a natural beginning. Ending it in the same way, sounds like too much. Nevertheless, this is the way I have to explain how things started three years – an a half – ago and to thank the people who, in many senses, were there.

Obviously, this thesis could not ever have been done without the position provided by Joachim Wambsganss at the Universität Potsdam – under the Deutsche Forschungsgemeinschaft grant WA 1047/6 –. I want to specially thank him for his trust on me and the freedom I had to conduct my research, even when I was wrong.

When I decided to come to Potsdam, I needed some help. Luis J. Goicoechea provided me with some funds for the first scientific contacts (from a Universidad de Cantabria project). Since then, I have been a Research Associate at his university, being funded for a three month visit there (and several shorter ones) and an observing period in Calar Alto. His additional advise during all this time was always a help.

The lensing group at the Instituto Astrofísico de Canarias (IAC) is also thanked for making their data available to me, in particular the observations at the IAC-80 telescope by Alex Oscoz, David Alcalde and Miquel Serra, among others. The head of the group, Evencio Mediavilla, invited me to a one month visit at the IAC and provided me with funds for a observation period at the Roque de los Muchachos Observatory in La Palma (under the IAC project P6/88). Moreover, he introduced me to Luis Goicoechea so, saying thanks to him is probably not enough.

Parts of the thesis have been done in other institutions. It is a pleasure to thank Sabine Schindler for selecting me to a three months Marie Curie Predoctoral Fellowship at the Liverpool John Moores Astrophysics Institute (contract number EU HPMT-CT-2000-00136). Working with Sabine and learning from her is always a very smooth process. She also invited me to a one week visit to

the Institut für Astrophysik in Innsbruck. In both institutes I met very nice people: Elisabetta de Filippis and Africa Castillo-Morales in Liverpool and Eelco van Kampen in Innsbruck help me a lot in my research.

I thank Yannick Mellier for a four months visit to the Institute d'Astrophysique de Paris (AIP) under an EARA Predoctoral Fellowship (contract HPMT-CT-2000-00132). Working in Paris was a very enrichment experience. Raphaël Gavazzi is also thanked for all the time he spent solving my scientific and technical problems.

In Potsdam, I have received inputs from many people. I shared office with Lutz Wisotzki for a long time. It is impossible to say how many things I learned from him and I was lucky that he was always ready for discussions. I thank Andreas Helms, Janine Heinmüller, Daniel Kubas, Robert Schmidt and Olaf Wucknitz for reading and commenting a first version of this thesis. And it is also something to thank how well they received the idea of moving group meetings to wine group meetings, which are a little longer. I specially thank Daniel for joining the spanish after-lunch 'tertulias', which are the soul of the spanish character. These 'tertulias' were visited by Giovanna, Isabel, Antonio, Ernest and Andreas in a more or less regular basis. With some of them, what it was supposed to be done after-lunch was converted into after-hours. Soon after arriving at Potsdam, I met Mamen and Marco. Since then, they have been always worry about me.

A thesis period, as almost any activity, is not free of bureaucracy. And if all those papers come from a german office, the problem gets harder for me. Andrea Brockhaus, the secretary in our Department, made completely transparent to me all those potential problems. Her help was something invaluable. In this sense, I also thank Rita Schulze-Gahlbeck, from the Internationale Begegnungszentren der Wissenschaften (IBZ). They made my life much easier.

Spanish Epilogue

La investigación es, desde mi punto de vista, una labor un tanto solitaria y dura, siempre absorbente y con tendencia a convertir el tiempo libre en una utopía. Todo ello se multiplica si a uno le prohíben la siesta, le obligan a comer en la hora del desayuno y le someten a torturas lingüísticas. Bajo estas circunstancias, la personalidad se trastoca, se invierte el norte y el espíritu se agría. Se pierden las buenas constumbres, como diría Ignatius J. Reilly. Sin embargo, es también la investigación una especie de droga de difícil abandono y, en los momentos en los que se obtienen resultados, llega la euforia introspectiva, una especie de éxtasis personal e intrasferible que casi nunca se deja ver. Esta breve y efímera embriaguez tiene también su fase de exaltacion de la amistad.

Con lo mal que he tratado a mis amigos, creo que no puedo terminar sin tan siquiera nombrar a muchos de los que he conseguido no perder y con los que he compartido buenos y malos momentos. Los de siempre son Jesús, Esteban, Adolfo, Raquel, Alfredo; aunque no necesito añadir nada más, les agradezco que siempre estén ahí, de una u otra forma. A ellos le dedico la introducción histórica de este trabajo. Creo que sabrán la razón.

De obligada mención son Araceli, Cristina y Sonia, no me perdonarían un olvido, como creo

estoy olvidando a muchos otros.

Durante tantos años de estudio he tenido la suerte de hacer buenos amigos en Valladolid, Salamanca y La Laguna: Pencho, Itziar, Marta, Sofía, Cristina, Marga, Iñigo A., Iñigo R., Sergio, Rafa y Victor. Muchos de ellos tienen la culpa de esta tesis, aunque no lo sepan. La cita en el sumario está especialmente pensada para el grupo de La Laguna.

He comenzado esta sección con un soneto de Quevedo. Creo que hay muchas personas a las que no he mencionado en estos agradecimientos y a las que seguro debo mucho. A todas ellas va dedicada esa cita.

References

Abajas C., Mediavilla E., Muñoz J.A., Popovic L.C., Oscoz A., 2002, ApJ, 576, 640

Abetti G., 1949, “Storia dell’Astronomia”, Vallecchi Editore (spanish edition: “Historia de la Astronomía”, 1956, Fondo de Cultura Económica)

Albrow M., Beaulieu J.-P., Birch P. et al., 1998, ApJ, 509, 687

Alcalde D., 2002, PhD. Thesis, Univerdad de la Laguna-IAC, Spain (in spanish)

Alcalde D., Mediavilla E., Moreau O. et al., 2002, ApJ, 572, 729

Alcock C., Akerloff C.W., Allsman R.A. et al., 1993, Nature, 365, 621

Alcock C., Allsman R.A., Alves D. et al., 1997, ApJ, 486, 697

Alcock C., Allsman R.A., Alves D. et al. (The MACHO Collaboration), 1997, ApJ, 491, L11

Alcock C., Allsman R.A., Alves D. et al., 1998, ApJ, 499, L9

Alcock C., Allsman R.A., Alves D. et al., 2000, ApJ, 542, 281

Allen S.W., 1998, MNRAS, 296, 392

Athreya R.M., Mellier Y., van Waerbeke L., Pelló R., Fort B., Dantel-Fort M., 2002, A&A, 384, 743-762

Aubourg E., Bareyre P., Brehin S. et al, 1993, Nature, 365, 623

Bahcall J.N., Sarazin C.L., 1977, AJ, 213, L99

Barkana R., 1997, ApJ, 489, 21

Bartelmann M., Huss A., Colberg J.M., Jenkins A., Pearce F.R., 1998, A&A, 330, 1

Bartelmann M., Narayan R., 1995, ApJ, 451, 60

Bartelmann M., Narayan R., Seitz S., Schneider P., 1996, ApJ, 464, L115

Bartelmann M., Schneider P., 2001, Physics Reports 340, 291 (also as astro-ph/9912508)

Bartelmann M., Weiss A., 1994, A&A, 287, 1

Baum W.A., 1959, PASP, 71, 106

Bernardeau F., Uzan J.-P., 2001, Physical Review D, 63(2)

Biggs A.D., Browne I.W.A., Helbig P. et al., 1999, MNRAS, 304, 349

Blandford R.D., Saust A.B., Brainerd T.G., Villumsen J.V., 1991, MNRAS, 251, 600

Boden A.F., Shao M., Van Buren D., 1998, ApJ, 502, 538

Böhringer H., Tanaka Y., Mushotzky R.F., Ikebe Y., Hattori M., 1998, A&A, 334, 789
Böhringer H., Soucail G., Mellier Y., Ikebe Y., Schuecker P., 2000, A&A, 353, 124
Bolzonella M., Miralles J.-M., Pelló R., 2000, A&A, 363, 476
Bond I., Abe F., Dodd R.J., et al. (MOA collab.), 2002, MNRAS, 331, L19
Bonnet H., Mellier Y., Fort B., 1994, ApJ, 427, L83
Brainerd T.G., Blandford R.D., Smail I., 1996, ApJ, 466, 623
Bridle S.L., Hobson M.P., Lasenby A.N., Saunders R., 1998, MNRAS, 299, 895
Broadhurst T.J., Huang X., Frye B., Ellis R.S., 2000, ApJ, 534, L15
Broadhurst T.J., Taylor A.N., Peacock J.A., 1995, ApJ, 438, 49
Bruzual G., Charlot S., 1993, ApJ, 405, 538
Burud I., Courbin F., Magain P. et al., 2002a, A&A, 383, 71
Burud I., Hjorth J., Coubin F. et al., 2002b, A&A, 391, 481
Burud I., Hjorth J., Jaunsen A.O., 2000, ApJ, 544, 117
Burud I., Magain P., Sohy S., Hjorth J., 2001, A&A, 380, 805
Chae K-H., Turnshek D.A., Khersonsky V.K., 1998, ApJ, 495, 609
Chang K., Refsdal S., 1984, A&A, 132, 168
Chwolson O., 1924, Astr. Nachrichten, 221, 329
Czoske O., Moore B., Kneib J.-P., Soucail G., A&A, 386, 31
Colley W.N., Shapiro I.I., Pegg J. et al., 2003a, ApJ, 588, 711
Colley W.N., Schild R.E., 2000, ApJ, 540, 104
Colley W.N., Schild R.E., Abajas C. et al., 2003b, ApJ, 587, 71
Colley W.N., Tyson J.A., Turner E.L., 1996, ApJ, 461, L83
Corrigan R.T., Irwin M.J., Arnaud J. et al., 1991, AJ, 102, 34
Courbin F., Lidman C.,Magain P., 1998, A&A, 330,57
Courbin F., Lidman C., Meylan G., Kneib J.-P., Magain P., 2000, A&A, 360, 853
Dekel A., Bertschinger E., Faber S.M., 1990, ApJ, 364, 349
Dickey J.M., Lockman F.J., 1990, ARA&A, 28, 215
Donahue M., Mack J., Scharf C., Lee P., Postman M., Rosati P. et al., 2001, ApJ, 552, L93
Dressler A., Gunn J.E., Schneider D.P., 1985, ApJ, 294, 70
Dressler A., Oemler A., Couch W.J. et al., 1997, ApJ, 490, 577
Edelson R.A., Krolik J.H., 1988, ApJ, 333, 646
Eddington A.S., 1920, “Space, time and gravitation”, Cambrige University Press
Einstein A., 1936, Science, 84, 506

Evans N.W., 2003, “Gravitational lensing: a unique tool for cosmology”, ASP Conference Series, eds., Valls-Gabaud D., Kneib J.-P. (also astro-ph/0304252)

Fahlman G., Kaiser N., Squires G., Woods D., 1994, ApJ, 431, L71

Fahlman G., Kaiser N., Squires G., Woods D., 1994, ApJ, 437, 56

Falco E.E, Wambsganss J., Schneider P., 1991, MNRAS, 251, 698

Fassnacht C.D., Womble D.S., Neugebauer G., et al., 1996, ApJ, 460, L103

Fassnacht C.D., Xanthopoulos E., Koopmans L.V.E., Rusin D., 2002, ApJ, 581, 823

Foltz C.B., Hewett P.C., Webster R.L., Lewis G.F., 1992, ApJ, 386, L43

Fort B., Mellier Y., 1994, A&ARv, 5, 239

Freedman W.L., Madore B.F., Gibson B.K. et al., 2001, ApJ, 553, 47

Freese K., Fields B., Graff D., 2000, ApJ, 534, 265

Friedman M., 1983, “Foundations of Space-Time Theories”, Princeton University Press (spanish edition: “Fundamentos de las teorías del espacio-tiempo”, 1991, Alianza Editorial)

Gavazzi R., Fort B., Mellier Y., Pelló R., Dantel-Fort M., 2003, A&A, 403, 11-27

Gladders M.D., López-Cruz O., Yee H.K.C, Kodama T., 1998, ApJ, 501, 571

Gladders M.D., Yee H.K.C., 2000, ApJ, 120, 2148

Gil-Merino R., Goicoechea L.J., Serra-Ricart M. et al., 1998, A&SS, 263, 47

Gil-Merino R., Goicoechea L.J., Serra-Ricart M. et al., 2001, MNRAS, 322, 428

Gil-Merino R., Schindler S., 2003, A&A, in press

Gil-Merino R., Wambsganss J., Goicoechea L.J., Lewis G., 2002a, A&A, submitted

Gil-Merino R., Wisotzki L., Wambsganss J., 2002b, A&A, 381, 428

Gioia I.M., Shaya E.J., Le Fèvre O., Falco E.E., Luppino G., Hammer F., 1998, ApJ, 497, 573

Goicoechea L.J., 2002, MNRAS, 334, 905

Goicoechea L.J., Alcalde D., Mediavilla E., Muñoz J.A., 2002, A&A, 397, 517

Goicoechea L., Mediavilla E., Oscoz A., Serra-Ricart M., Buitrago J., 1998b, A&SS, 261, 341

Goicoechea L., Oscoz A., Mediavilla E., Buitrago J., Serra-Ricart M., 1998a, ApJ, 492, 74 (G98)

Gorenstein M.V., Falco E.E., Shapiro I.I., 1988, ApJ, 327, 693

Gould A., 1995, ApJ, 444, 556

Gould A., 1997, “Astronomical Time Series”, Kluwer, p. 37

Gould A., Miralda-Escudé J., 1997, ApJ, 483, L13

Grogin N.A., Narayan R., 1996, ApJ, 464, 92; erratum, 1996, ApJ, 473, 570

Grossman S.A, Narayan R., 1988, ApJ, 324, L37

Gunn J.E., Oke J.B., 1975, ApJ, 195, 255

Haarsma D.B., Hewitt J.N., Lehár J., Burke B.F., 1997, ApJ, 479, 102

Haarsma D.B., Hewitt J.N., Lehár J., Burke B.F., 1999, ApJ, 510, 64

Hainaut O.R., Meech K.J., Boehnhardt H., West R.M., 1998, A&A, 333, 746

Hammer F., Rigaut F., 1989, A&A, 226, 45

Hawkins M.R.S., 1993, Nature, 366, 242

Hawkins M.R.S., Taylor A.N., 1997, ApJ, 482, L5

Hjorth J., Burud I., Jaunsen A.O. et al., 2002, ApJ, 572, L11

Hoekstra H., Franx M., Kuijken K., 1998, ApJ, 504, 636-660

Hoekstra H., Franx M., Kuijken K., 2003, MNRAS, 340, 609

Hoskin M., ed., 1999, "The Cambridge Concise History of Astronomy", Cambridge University Press

Humason M.L., Sandage A., 1957, Carnegie Institution of Washington Yearbook 1956, 61

Ibata R., Harvey B., Gilliland R.L., Scott D. et al., 1999, ApJ, 524, L95

Impey C.D., Falco E.E., Kochanek C.S., Lehár J., McLeod B.A., Rix H.-W., Peng C.Y., Keeton C.R., 1998, ApJ, 509, 551

Irwin M. J., Webster R. L., Hewitt P. C., Corrigan R. T., Jedrzejewski R. I., 1989, AJ, 98, 1989

Kaiser N., 1992, ApJ, 388, 272

Kaiser N., Squires G., 1993, ApJ, 404, 441

Kaiser N., Squires G., Broadhurst T., 1995, ApJ, 449, 460

Kassiola A., Kovner I., Fort B., 1992, ApJ, 400, 41

Kayser R., Refsdal S., Stabell R., 1986, A&A, 166, 36

Keeton C.R., Falco E.E., Impey C.D., Kochanek C.S., Lehár J., McLeod B.A., Rix H.-W., Muñoz J.A, Peng C.Y., 2000, ApJ, 542, 74

Kent S.M., Falco E.E., 1988, AJ, 96, 1570

King L.J., Browne I.W.A., Muxlow T.W.B. et al., 1997, MNRAS, 289, 250

Klimov Y.G., 1963, Sov. Phys. Doklady, 8, 119

Kneib J.-P., Hudelot P., Ellis R.S., Treu T., Smith G.P., Marshall P., Czoske O., Smail I., Natarajan P., 2003, ApJ, submitted, astro-ph0307299

Kneib J.-P., Mellier Y., Fort B., Mathez G., 1993, A&A, 237, 367

Kneib J.-P., Mellier Y., Pelló R, Miralda-Escudé J., Le Borgne J.-F., Böhringer H., Picat J.P., 1995, A&A, 303, 27

Kochanek C.S., 1995, ApJ, 445, 559

Kochanek C.S., 1996, ApJ, 466, 638

Kochanek C.S., 2002, ApJ, 578, 25

Kochanek C.S., Keeton C.R., McLeod B.A., 2001, ApJ, 547, 50

Kochanek C.S., Falco E.E., Impey C., Léhar J., McLeod B.A., Rix H.-W., 1998, CASTLE Survey, http://cfa-www.harvard.edu/castles/

Kochanek C.S., Schechter P.L, 2003, to appear in "Measuring and Modeling the Universe", Carnegie Observatories Astrophysics Series, Vol. 2. Ed. W.L. Freedman, Cambrige University Press (also as astro-ph/0306040)

Koo D.C., 1988, "Large-Scale Motions in the Universe", Rubin V.G, Cayne G.V. (eds.), Princeton Univ. Press, 513

Koopmans L.V.E., de Bruyn A.G., 2001, in Brainerd T.G., Kochanek C. S., eds., "Gravitational Lensing: Recent Progress and Future Goals", ASP Conference Proceedings, Vol. 237. San Francisco: Astronomical Society of the Pacific, ISBN: 1-58381-074-9

Koopmans L.V.E., de Bruyn A.G., Xanthopoulos E., Fassnacht C.D., 2000, A&A, 356, 391

Kundić T., Colley W.N., Gott III J.R. et al., 1995, ApJ, 455, L5

Kundić T., Turner E.L., Colley W.N. et al., 1997, ApJ482, 75

Kundić T., Wambsganss J., 1993, ApJ, 404, 455

Laplace P.S., 1795, "Exposition du système du monde"

Lasserre, T., et al., 2000, A&A355, L39

Lehár J., Hewitt J.N., Roberts D.H., Burke B.F, 1992, ApJ, 384, 453

Lehár J., Falco E.E., Kochanek C.S., McLeod B.A., Muñoz J.A., Impey C.D., Rix H.-W., Keeton C.R., Peng C.Y., 2000, ApJ, 536, 584

Lewis G.F., Ibata R.A., 1998, ApJ, 501, 478

Lewis G.F., Irwin M.J., 1995, MNRAS, 276, 103

Lewis G.F., Irwin M.J., Hewett P.C., 1996, IAU Symposium, 173, 241

Lewis G.F., Miralda-Escudé J., Richardson D.C., Wambsganss J., 1993, MNRAS, 261, 647

Lidman C., Courbin F., Kneib J., Golse G., Castander F., Soucail G., 2000, A&A, 364, L6

Liebes S., 1964, Phys. Rev. B, 133, 835

Lineweaver C.H., Tenorio L., Smoot G.F. et al., 1996, ApJ, 470, 38

Lodge O.J., 1919, Nature, 104, 354

López S., Reimers D., Rauch M., Sargent W.L.W., Smette A., 1999, ApJ, 513, 598

Lovell J.E.J., Jauncey D.L., Reynolds J.E. et al., 1998, ApJ, 508, 51

Luppino G.A., Kaiser N., 1997, ApJ, 475, 20

Lynds R., Petrosian V., 1987, Bull. AAS, 18, 1014

Lynds R., Petrosian V., 1989, ApJ, 336, 1

Mao S., 2001, in Brainerd T.G., Kochanek C.S., eds., "Gravitational Lensing: Recent Progress and Future Goals", ASP Conference Proceedings, Vol. 237. San Francisco: Astronomical Society of the Pacific, ISBN: 1-58381-074-9

Maoli R., Van Waerbeke L., Mellier Y. et al., 2001, A&A, 368, 766

Maoz D., Rix H.-W., 1993, ApJ, 416, 425

Mediavilla E., Arribas S., del Burgo C. et al., 1998, ApJ, 503, 27

Mellier Y., 1999, Ann. Rev. Astron. Astrophys., 37, 127-189

Mellier Y., Fort B., Soucail G. et al., 1991, ApJ, 380, 334

Mellier Y., Fort B., Kneib J.-P., 1993, ApJ, 407, 33

Meneghetti M., Bartelmann M., Moscardini L., 2003, MNRAS, 340, 105

Merrit D., Tremblay B., 1994, AJ, 108, 514

Michell J., 1982, "Black Holes: Selected reprints", Stony Brook. Originally appeared in 1784, Trans. R. Soc. London, 74, 35.

Miralda-Escudé J., 1991, ApJ, 380, 1

Miralda-Escudé J., Babul A., 1995, ApJ, 449, 18

Misner C.W., Thorne K.S., Wheeler J.A., 1973, "Gravitation", W.H. Freeman and Company

Navarro J.F., Frenk C.S., White S.D.M., 1997, ApJ, 490, 493-508

North J., 1994, "The Fontana history of astronomy and cosmology", Fontana Press (spanish edition: "Historia Fontana de la astronomía y la cosmología", 2001, Fondo de Cultura Económica)

Ofek E.O., Maoz D., 2003, ApJ, in press (astro-ph/0305200)

Oscoz A., Mediavilla E., Goicoechea L.J., Serra-Ricart M., Buitrago J., 1997, ApJ, 479, L89

Oscoz A., Serra-Ricart M., Goicoechea L.J., Buitrago J., Mediavilla E., 1996, ApJ, 470, L19

Østensen R., Refsdal S., Stabell R. et al., 1996, A&A, 309, 59

Ota N., Mitsuda K., Fukazawa Y., 1998, ApJ, 495, 170

Ota N., Pointecouteau E., Hattori M., Mitsuda K., 2003, astro-ph/0306580

Ovaldsen J.E., Teuber J., Schild R.E., Stabell R., 2003, A&A, 402, 891

Paczyński B., 1986a, ApJ, 301, 503

Paczyński B., 1986b, ApJ, 304, 1

Paczyński B., 1987, Nature, 325, 572

Patnaik A.R., Narasimha D., 2001, MNRAS, 326, 1403

Peacock J.A., 1999, "Cosmological Physics", Cambridge University Press

Peebles P.J.E., 1993, "Principles of Physical Cosmology", Princeton University Press.

Peebles P.J.E., Phelps S.D., Shaya E.J., Tully R.B., 2001, ApJ, 554, 104

Pelt J., Holf W., Kayser R., Refsdal S., Schramm T., 1994, A&A, 286, 775 (P94)

Pelt J., Kayser R., Refsdal S., Schramm T., 1996, A&A, 305, 97 (P96)

Pelt J., Refsdal S., Stabell R., 2002, A&A, 389, L57

Pelt J., Schild R., Refsdal S., Stabell R., 1998, A&A, 336, 829

Petters A.O., Levine H., Wambsganss J., 2001, "Singularity Theory and Gravitational Lensing", Birkhäuser

Pijpers F.P., 1997, MNRAS, 289, 933

Popović L.C., Mediavilla E., Jovanović P., Muñoz J.A., 2003, A&A, 399, 795

Press W.H., Rybicki G.B., 1998, ApJ, 507, 108

Press W.H., Rybicki G.B., Hewitt J.N., 1992a, ApJ, 385, 404 (PRH92)

Press W.H., Rybicki G.B., Hewitt J.N., 1992b, ApJ, 385, 416 (PRH92)

Press W.H., Teukolsky S.A., Vetterling W.T., Flannery B.P., 1992, "Numerical Recipes: The Art of Scientific Computing", Cambridge University Press

Refsdal S., 1964a, MNRAS, 128, 295

Refsdal S., 1964b, MNRAS, 128, 307

Remy M., Claeskens J.-F., Surdej J., Hjorth J., Refsdal S., Wucknitz O., Sørensen A., Gruhdahl F., 1998, NewA, 3, 379

Rix H.W., Franx M., Fischer D., Illingworth G., 1992, AJ, 104, 959

Roukema B.F., Bajtlik S., 1999, MNRAS, 308, 309

Saha P., Williams L.L.R, 2003, AJ, 125, 2769

Sandage A., Visvanathan N., 1978, ApJ, 225, 742

Sarazin C.L., 1988, "X-ray emissions from clusters of galaxies", Cambridge University Press

Schechter P.L., 2000, in IAU Symp. 201, New Cosmology and the Values of the Fundamental Parameters, ed. A.N. Lasenby and A. Wilkinson (also as astro-ph/0009048)

Schechter P.L., Udalski A., Szymanski M. et al., 2003, ApJ, 584, 657

Schild R.E., 1996, ApJ, 464, 125 (S96)

Schild R.E., 1999, ApJ, 514, 598

Schild R.E., Thomson D.J., 1995, in Holt S.S., Bennett C.L. eds., "Dark Matter", AIP Conference Proceedings, 336, 95

Schild R.E., Thomson D.J., 1997, AJ, 113, 130

Schindler S., Belloni P., Ikebe Y., Hattori M., Wambsganss J., Tanaka Y., 1998, A&A, 338, 843

Schindler S., Castillo-Morales A., De Filippis E., Schwope A., Wambsganss J., 2001, A&A376, L27

Schindler S., Hattori M., Neumann D.M., Böhringer H., 1997, A&A, 317, 646

Schindler S., Wambsganss J., 1996, A&A, 313, 113

Schindler S., Wambsganss J., 1997, A&A, 322, 66

Schmidt R.W., Kundić T., Pen U.-L. et al., 2002, A&A, 392, 773

Schmidt R.W., Wambsganss J., 1998, A&A, 335, 379 (SW98)

Schmidt R.W., Webster R.L., Lewis G.F., 1998, MNRAS, 295, 488

Schneider P., 1985, A&A, 143, 413

Schneider D.P., Dressler A., Gunn J.E., 1986, AJ, 92, 523

Schneider P., Ehlers J., Falco E.E., 1992, "Gravitational Lenses", Springer Verlag

Schneider D.P., Turner E.L., Gunn J.E. et al., 1988, AJ, 95, 1619

Schneider P., Wambsganss J., 1990, A&A, 237, 42

Schneider P., Weiss A., 1987, A&A, 171, 49

Schramm T., Kayser R., Chang K., et al., 1992, A&A, 268, 350

Schrödinger E., 1950, "Space-Time Structure", Cambridge University Press (spanish edition: "La estructura del espacio-tiempo", 1992, Alianza Editorial)

Schutz, B.F., 1985, "A first course in general relativity", Cambrige University Press

Schwope A., Hasinger G., Lehmann I. et al., 2000, AN, 321, 1

Serra-Ricart M., Oscoz A., Sanchis T., Mediavilla E., Goicoechea L.J., Licandro J., Alcalde D., Gil-Merino R., 1999, ApJ, 526, 40 (SR99)

Seitz C., Schneider P., 1995, A&A, 297, 287

Seitz S., Schneider P., Bartelmann M., 1998, A&A, 337, 325

Shalyapin V.N., Goicoechea L.J., Alcalde D., Mediavilla E., Muñoz J.A., Gil-Merino R. et al., 2002, ApJ, 579, 127

Simonetti, J. H., Cordes, J. M., Heeschen, D. S., 1985, ApJ, 296, 46

Sklar L., 1992, "Philosophy of Physics", Westview Press (spanish edition: "Filosofía de la física", 1994, Alianza Editorial)

Sluse D., Surdej J., Claeskens J.-F. et al., 2003, A&A, 406, 43

Smail I., Dressler A., Kneib J.-P., Ellis R.S., Couch W.J., Sharples R.M., Oemler A., 1996, ApJ, 469, 508

Smail I., Ellis R.S., Dressler A., Couch W.J., Oemler A., Sharples R.M., Butcher H., 1997, ApJ, 479, 70

Smail I., Ellis R.S., Fitchett M.J., 1994, MNRAS, 270, 245

Smail I., Ellis R.S., Fitchett M.J., Edge A.C., 1995, MNRAS, 273, 277

Smette A., Robertson J.G., Shaver P.A., Reimers D., Wisotzki L., Köhler T., 1995, A&A, 113, 199

Smith S., 1936, AJ, 83, 23

Smith D.R., Bernstein G.M., Fischer P., Jarvis M., 2001, ApJ, 551, 643

Stetson P.B., 1987, PASP, 99, 191

Soldner J., 1804, Berliner Astronomisches Jahrbuch, 161

Soucail G., Fort B., Mellier Y., Picat J.P., 1987, A&A, 172, L14

Soucail G., Mellier Y., Fort B., Mathez G., Cailloux M., 1988, A&A, 191, L19

Soucail G., Ota N., Böhringer H., Czoske O., Hattori M., Mellier Y., 2000, A&A, 355, 433

Squires G., Kaiser N., 1996, ApJ, 473, 65

Stockton A., 1980, ApJ, 242, L141

Sutherland W., 1999, Rev. Mod. Phys. 71, 421

Torretti R., 1999, "The Philosophy of Physics", Cambridge University Press

Treu T., Koopmans L.V.E., 2003, MNRAS, 343, L29

Trimble V., 2001, in Brainerd T.G., Kochanek C.S., eds., "Gravitational Lensing: Recent Progress and Future Goals", ASP Conference Proceedings, Vol. 237. San Francisco: Astronomical Society of the Pacific, ISBN: 1-58381-074-9

Tyson J.A., Fischer P., 1995, ApJ, 446, L55

Tyson J.A., Kochanski G.P., Dell'Antonio I.P., 1998, ApJ, 498, L107

Tyson J.A., Valdes F., Wenk R.A., 1990, ApJ, 349, L1

Udalski A., Szymanski M., Kaluzny J. et al., 1993, AcA, 43, 289

Uzan J.-P., Bernardeau F., 2001, Physical Review D, 63(2)

Van Waerbeke L., Mellier Y., Radovich M. et al., 2001, A&A, 374, 757

Vilenkin A., Shellard E.P.S., 1994, "Cosmic Strings and Other Topological Defects", Cambridge University Press

Voges W., Aschenbach B., Boller T. et al., 1996, IAU Circ. 6420

Voges W., Aschenbach B., Boller T. et al., 1999, A&A, 349, 389

Walsh D., Carswell R.F., Weymann R.J., 1979, Nature, 279, 381

Wambsganss J., 1990, PhD thesis, Munich University, report MPA 550

Wambsganss J., 1999, Journ. Comp. Appl. Math., 109, 353

Wambsganss J., 2001, in "Cosmological Physics with Gravitational Lensing", Proceedings of the XXXVth Rencontres de Moriond, 2000, eds. Tran J.T.V., Mellier Y., Moniez M., EDP Sciences

Wambsganss J., Bode P., Ostriker J.P., 2003, ApJ, submitted (astro-ph/0306088)

Wambsganss J., Kundić T., 1995, ApJ, 450, 19

Wambsganss J., Paczyński B., 1994, AJ, 108, 1156

Wambsganss J., Schneider P., Paczyński B., 1990, ApJ, 358, 33

Webster R.L., Ferguson A.M.N., Corrigan R.T., Irwin M.J., 1991, AJ, 102, 1939

Weinberg S., 1972, "Gravitation and Cosmology", J. Wiley & Sons

Will C.M., 1988, Astr. Ap., 236, 311

Williams L.L.R., Navarro J.F, Bartelmann M., 1999, ApJ, 527, 535

Witt H.J., 1993, ApJ, 403, 530

Witt H.J., Mao S., 1994, ApJ, 429, 66

Witt H.J., Mao S., Keeton C.R., 2000, ApJ, 544, 98

Wisotzki L., Becker T., Christensen L. et al., 2003, A&A, accepted, (astro-ph/0307147)

Wisotzki L., Köhler T., Ikonomou M., Reimers D., 1995, A&A, 297, L59

Wisotzki L., Köhler T., Kayser R., Reimers D., 1993, A&A, 278, L15

Wisotzki L., Wucknitz O., López S., Sørensen A., 1998, A&A, 339, L73 (W98)

Woźniak P.R., Alard C., Udalski A., Szmanski M., Kubiak M., Pietrzynski G., Zebrun K., 2000, ApJ, 529, 88

Woźniak P. R., Udalski A., Szymański et al., 2000b, ApJ, 540, L65

Wu X.-P., Fang L.-Z., 1997, ApJ, 483, 62

Wucknitz O., Wisotzki L., López S., Gregg M.D., 2003, A&A, 405, 445

Wyithe J.S.B., Loeb A., 2002, ApJ, 577, 615

Wyithe J.S.B., Webster R.L., Turner E.L., 1999, MNRAS, 309, 261

Wyithe J.S.B., Webster R.L., Turner E.L., 2000a, MNRAS, 315, 51

Wyithe J.S.B., Webster R.L., Turner E.L, Mortlock D.J., 2000b, MNRAS, 315, 62

Yee H.K.C., 1988, AJ, 95, 1331

Yonehara A., 1999, ApJ, 519, L31

Yonehara A., 2001, ApJ, 548, L127

Zhao H., Pronk D., 2001, MNRAS, 320, 401

Zwicky F., 1933, Helv. Phys. Acta 6, 110

Zwicky F., 1937a, Phys. Rev. Lett. 51, 290

Zwicky F., 1937b, Phys. Rev. Lett. 51, 679

List of Publications

Refereed papers

1. **Gil-Merino R.**, Schindler S., ”Galaxy and hot gas distributions in the z=0.52 galaxy cluster RBS380 from CHANDRA and NTT observations”, **2003, A&A, in press (also astro-ph/0306499)**

2. **Gil-Merino R.**, Wambsganss J., Goicoechea L.J., Lewis G., ”The transverse velocity of the lensing Galaxy in Q2237+0305 from the lack of microlensing variability”, **2003, A&A, submitted**

3. Shalyapin V.N., Goicoechea L.J., Alcalde D., Mediavilla E., Muñoz J.A., **Gil-Merino R.**, ”The Nature and Size of the Optical Continuum Source in QSO 2237+0305”, **2002, ApJ, 579, 127**

4. Alcalde D., Mediavilla E., Moreau O., Muñoz J.A., Libbrecht C., Goicoechea L.J., Surdej J., Puga E., De Rop Y., Barrena R., **Gil-Merino R.**, McLeod B.A., Motta V., Oscoz, A., Serra-Ricart M., ”QSO 2237+0305 VR Light Curves from Gravitational LensES International Time Project Optical Monitoring”, **2002, ApJ, 572, 729**

5. **Gil-Merino R.**, Wisotzki L., Wambsganss J., ”The Double Quasar HE 1104−1805: A case study for time delay determination with poorly sampled lightcurves”, **2002, A&A, 381, 428**

6. **Gil-Merino R.**, Goicoechea L.J., Serra-Ricart M., Oscoz A., Alcalde D., Mediavilla E., ”Short time-scale fluctuations in the difference light curves of QSO 0957+561A,B: microlensing or noise?”, **2001, MNRAS, 322, 428**

7. Serra-Ricart M., Oscoz A., Sanchs T., Mediavilla E., Goicoechea L.J., Licandro J.,Alcalde D., **Gil-Merino R.**, ”BVRI Photometry of QSO 0957+561A, B: Observations, New Reduction Method, and Time Delay”, **1999, ApJ, 526, 40**

8. **Gil-Merino R.**, Goicoechea L.J., Serra-Ricart M., Oscoz A., Mediavilla E., Buitrago J., ”Analysis of the Difference Light Curve of the Gravitational Mirage QSO 0957+561”, **1998, A&SS, 263, 47**

Proceedings

9. Goicoechea L.J., **Gil-Merino R.**, Serra-Ricart M., Mediavilla E., Oscoz A., Alcalde D., "The Nature of Dark Matter in Elliptical (cD) Galaxies: Main Lens Galaxy of Q0957+561", **Gravitational Lensing: Recent Progress and Future Goals**, ASP Conference Proceedings, Vol. 237. Edited by Tereasa G. Brainerd and Christopher S. Kochanek. San Francisco: Astronomical Society of the Pacific, ISBN: 1-58381-074-9, 2001, p.87

10. Puga E., Alcalde D., Barrena R., Mediavilla E., Motta V., Muñoz J.A., Oscoz A., Serra-Ricart M., **Gil-Merino R.** and 6 coauthors, "Daily monitoring of the gravitational lens QSO 2237+0305 at the Nordic Optical Telescope", **Highlights of Spanish astrophysics II**, Proceedings of the IV Scientific Meeting of the Spanish Astronomical Society (SEA), held in Santiago de Compostela, Spain, September 11-14, 2000, Dordrecht: Kluwer Academic Publishers, 2001 xxii, 409 p. Edited by Jaime Zamorano, Javier Gorgas, and Jesus Gallego. ISBN 0792369742, p.53

11. Goicoechea L.J., **Gil-Merino R.**, Serra-Ricart M., Oscoz A., Alcalde D., Mediavilla E., "IAC gravitational lenses monitoring program: difference signals from 2.5 years of QSO 0957+561 observations", **Highlights of Spanish astrophysics II**, Proceedings of the IV Scientific Meeting of the Spanish Astronomical Society (SEA), held in Santiago de Compostela, Spain, September 11-14, 2000, Dordrecht: Kluwer Academic Publishers, 2001 xxii, 409 p. Edited by Jaime Zamorano, Javier Gorgas, and Jesus Gallego. ISBN 0792369742, p.376

12. **Gil-Merino R.**, Schindler S., "The Galaxy Cluster RBS380: X-ray and Optical Analysis", to appear in **Highlights of Spanish Astrophysics III**, Proceedings of the V Meeting of the Spanish Society of Astronomy (SEA), held in Toledo, Spain, September 9-13, 2002. Eds. J. Gallego, J. Zamorano and N. Cardiel, ASSL, Kluwer Academic Publishers